AN ABSTRACT OF THE THESIS OF

James W. MacLean for the degree of Master of Science in Geology presented on February 17, 1994.

Title: Geology and Geochemistry of Juniper Ridge, Horsehead Mountain and Burns Butte: Implications for the Petrogenesis of Silicic Magma on the High Lava Plains, Southeastern Oregon.

Abstract approved: Signature redacted for privacy.
Anita L. Grunder

The Juniper Ridge volcanic complex is located in the High Lava Plains Province of southeastern Oregon, a wide zone of bimodal volcanism and faulting that marks the northern limit of widespread Basin and Range-style faulting in the northern Great Basin Province. Rhyolite dome complexes are progressively younger to the northwest along the High Lava Plains, providing a mirror-image to age-progressive silicic volcanism on the Snake River Plain in southern Idaho. ^{40}Ar-^{39}Ar dating of rocks from western and eastern Juniper Ridge (5.70 ± 0.02 Ma and 6.87 ± 0.02 Ma, respectively) and Burns Butte (7.75 ± 0.06 Ma) confirms the overall age progression, and shows that age relations within the Juniper Ridge complex are consistent with the trend. Horsehead Mountain (15.54 ± 0.03 Ma) predates the age progression altogether.

Rocks at both eastern Juniper Ridge and western Juniper Ridge are overlain by diktytaxitic olivine basalt flows similar to regional high-alumina olivine tholeiites (HAOTs). At western Juniper Ridge, high-silica rhyolite flows overlie lower-silica rhyolite and hybrid andesite flows. At eastern Juniper Ridge, a suite of intermediate rocks ranging from basaltic andesite to dacite overlies a series of rhyolite flows. Rocks at Burns Butte consist of high-silica rhyolite, porphyritic dacite and rhyodacite, and andesite.

Field and petrographic observations, including mixing textures, inclusions, and xenocrysts, along with straight-line relationships on chemical diagrams, show that the

intermediate rocks at western Juniper Ridge formed by mixing between high-silica rhyolite magma and slightly evolved HAOT, probably at the base of a large silicic magma chamber. In contrast, curvilinear geochemical trends and an internally consistent four-stage major and trace element model suggest that intermediate rocks at eastern Juniper Ridge evolved in small, unconnected magma chambers by removal of olivine, plagioclase, clinopyroxene, and magnetite from a primitive HAOT parent, accompanied by contamination by up to 22 percent rhyolite. Unusually elevated concentrations of incompatible trace elements in the Squaw Butte basaltic andesite were produced by either zone refining or combined fractionation and recharge.

The least-evolved rhyolites at eastern and western Juniper Ridge have lower rare-earth element concentrations than the intermediate fractionates at eastern Juniper Ridge, thus precluding an origin by crystal fractionation from the observed intermediate rocks, but have major element compositions close to those of experimental dehydration melts of amphibolite. The rhyolites probably originated as dehydration melts of an amphibolite lower crust, which were subsequently modified by removal of quartz, sanidine, plagioclase, clinopyroxene and zircon. At western Juniper Ridge, the fractionating assemblage probably included trace allanite.

Rhyolites from dome complexes and ash-flow tuffs of the 5- to 10-Ma portion of the age-progressive trend show systematic trace element variations with position along the trend. Dome complexes include Burns Butte, Palomino Butte, eastern and western Juniper Ridge and Glass Buttes; ash-flow tuffs include the Devine Canyon Tuff, the Prater Creek Tuff, the Rattlesnake Tuff and the tuff of Buckaroo Lake. From east to west, Y/Nb and Yb/Ta increase, and Ce/Yb decreases in the least-evolved rhyolite in each suite. These variations can be accounted for by a systematic increase in degree of garnet-residual partial melting of amphibolite crust from east to west, correlating either with degree of extension with time along the Brothers fault zone, or with distance from the main axis of faulting.

Porphyritic, calc-alkaline andesites and dacites erupted from at least six vents at Horsehead Mountain. Field relationships indicate a general decrease in age from southwest to northeast within the complex. At 15 Ma, calc-alkaline volcanism at Horsehead Mountain

predates the age-progressive rhyolites, and is instead part of an earlier phase of volcanism that produced the Steens and Columbia River flood basalts, along with several other calc-alkaline intermediate centers that are unrelated to subduction. Overlapping rare-earth element patterns of Horsehead Mountain intermediate rocks with those of Steens basalts precludes their derivation by fractionation from the broadly contemporaneous flood basalts.

Geology and Geochemistry of Juniper Ridge, Horsehead Mountain and Burns Butte: Implications for the Petrogenesis of Silicic Magma on the High Lava Plains, Southeastern Oregon.

by

James W. MacLean

A THESIS

submitted to

Oregon State University

in partial fulfillment of
the requirements for the
degree of

Master of Science

Completed February 17, 1994

Commencement June 1994

ACKNOWLEDGEMENTS

Sincere thanks go to Anita Grunder for her patience, inspiration and support during the course of my graduate work. Thanks also to various collaborators, including Martin Streck and Al Dieno. This thesis is brought to you in part by funding and assistance from the National Science Foundation, the Geological Society of America and the OSU Radiation Center.

My ideas about the volcano-tectonic evolution of the northern Great Basin, as well as the petrogenesis of silicic volcanic rocks, was shaped in part by discussions with Martin Streck, Eric Seedorff, Anita Grunder, Jenda Johnson, Jeff Templeton, and Allyson Mathis. Their ideas and interest in this project are greatly appreciated, however, the interpretations and possible flaws herein are entirely my own.

TABLE OF CONTENTS

LIST OF FIGURES

LIST OF TABLES

LIST OF PLATES

Plates are in rear pocket

GEOLOGY AND GEOCHEMISTRY OF JUNIPER RIDGE, HORSEHEAD MOUNTAIN AND BURNS BUTTE: IMPLICATIONS FOR THE PETROGENESIS OF SILICIC MAGMA ON THE HIGH LAVA PLAINS, SOUTHEASTERN OREGON.

CHAPTER ONE: INTRODUCTION

Rhyolitic volcanism along the High Lava Plains is systematically younger to the northwest, from about 15 Ma in the Owyhee Plateau region of westernmost Idaho to Holocene age at Newberry Volcano in Oregon (MacLeod et al., 1975). The High Lava Plains trend is mirrored to the east by age-progressive rhyolitic volcanism along the Snake River Plain in Idaho, which, together with the High Lava Plains, constitutes the northern limit of major Basin and Range extension. Competing models for the migration of silicic vents (e.g. crustal rifting, Christiansen and McKee (1978); hotspot track, Duncan (1982); and back-arc spreading, Hart and Carlson (1987) are hampered by lack of precise age and geochemical data that are necessary to provide constraints on the magmatic and tectonic evolution of the northern Basin and Range Province.

1.1 Rationale and Methods

Limited chemical and age data are available for individual silicic dome complexes along the High Lava Plains trend. Previous work on regional stratigraphy and chemistry focuses on the ash-flow tuff sheets and associated domes of Harney Basin (e.g. Davenport, 1971; Greene, 1973, Parker, 1974, Walker, 1979). Most data on silicic rocks from the High Lava Plains were collected in the reconnaissance studies of Walker and coworkers (Walker, 1974; MacLeod et al., 1975; Walker, 1981). Cummings and students identified compositional variation and age-progression in their studies of the volcanic stratigraphy and geochemistry of the Glass Buttes complex (Berri et al., 1983; Cummings, 1984; Cummings, 1985; Roche,1988; Cummings and

Roche, 1989). Chemical data are also available from Newberry Volcano (MacLeod and Sherrod, 1988; Linneman and Myers, 1990).

This thesis focuses on age relations and petrogenesis of volcanic rocks at Juniper Ridge, and is part of a larger project to gather age, geological and analytical data for silicic dome complexes in the 5 to 10 Ma portion of the High Lava Plains trend. The main goals of the project are (1) to determine the longevity of individual vent complexes and to test for within-complex age-progression; (2) to establish a matrix of age and geochemical data in order to constrain magmatic processes and to identify compositional variations along the age-progressive trend; and (3) to examine the relationship between magmatism and tectonism in order to better understand how the trend developed.

Geologic mapping at a scale of 1:24,000 (Plate I) was supplemented by ^{40}Ar-^{39}Ar dating to establish a temporal framework for the volcanic rocks at Juniper Ridge. Stratigraphic relations and petrographic characteristics of each map unit are summarized in Chapter 2. Age and geochemical data for Juniper Ridge and Burns Butte, an approximately 8-Ma bimodal vent complex that was mapped by Brown (1982), are presented in Chapter 3, along with mineral chemical data from representative Juniper Ridge samples obtained by electron microprobe analysis. Geochemical constraints on the petrogenesis of Juniper Ridge rocks are examined in Chapter 4 and regional variations in rhyolite chemistry along the 5 to 10 Ma portion of the High Lava Plain with implications for the evolution of the northern Basin and Range are discussed in Chapter 5.

Another dome complex, Horsehead Mountain (15.54 ± 0.03 Ma; ^{40}Ar-^{39}Ar; Table 6.1), was mapped and sampled before age data revealed it to be too old for the main goals of the study. The basic geologic and geochemical relationships at Horsehead Mountain (Chapter 6), a geologic map at the scale of 1:12,000 (Plate 2), and a summary of petrographic descriptions (Appendix 1) are presented for completeness.

1.2 Tectonic setting

Juniper Ridge is located in the High Lava Plains province of southeastern Oregon (Fig. 1.1), and is dissected by the Brothers fault zone, a northwest-trending series of subparallel faults that mark the northern boundary of Basin and Range extension (Lawrence, 1976). Basin and Range block faulting, defined topographically by regularly spaced, normal fault-bounded horsts and intervening sediment-filled grabens, is prevalent to the south of the 20- to 50-kilometer-wide zone, but is nearly absent to the north of it. The Brothers fault zone is one of several en echelon features that separate extended terrain in southern and eastern Oregon from relatively unextended areas to the north; others include, from southwest to northeast, the McLoughlin zone, the Eugene-Denio zone, the Vale zone, and the Olympic-Wallowa lineament. Despite the appearance of right-lateral offset of large-scale geomorphic features (Lawrence, 1976), and the inference that Oregon is the limit of province-wide dextral shear related to the San Andreas transform system (Atwater, 1970; Livaccari, 1979), strike-slip movement has yet to be documented on any individual fault within the Brothers fault zone.

1.3 Volcanism on the High Lava Plains

In addition to serving as a structural boundary between the Basin and Range province to the south and the Blue Mountains province to the north, the High Lava Plains host voluminous bimodal volcanism. High-alumina olivine tholeiite (HAOT) lavas, with geochemical affinities to oceanic basalts, make up the dominant volume of volcanic rock in the province (at least 650 km^3, according to Hart et al., 1984), and are intercalated with several large ash-flow tuff sheets and volumetrically minor silicic dome complexes and sedimentary rocks (Walker, 1979). Because HAOT lavas in eastern Oregon have characteristics similar to back-arc basin basalts, including primitive major element compositions, depleted incompatible trace element

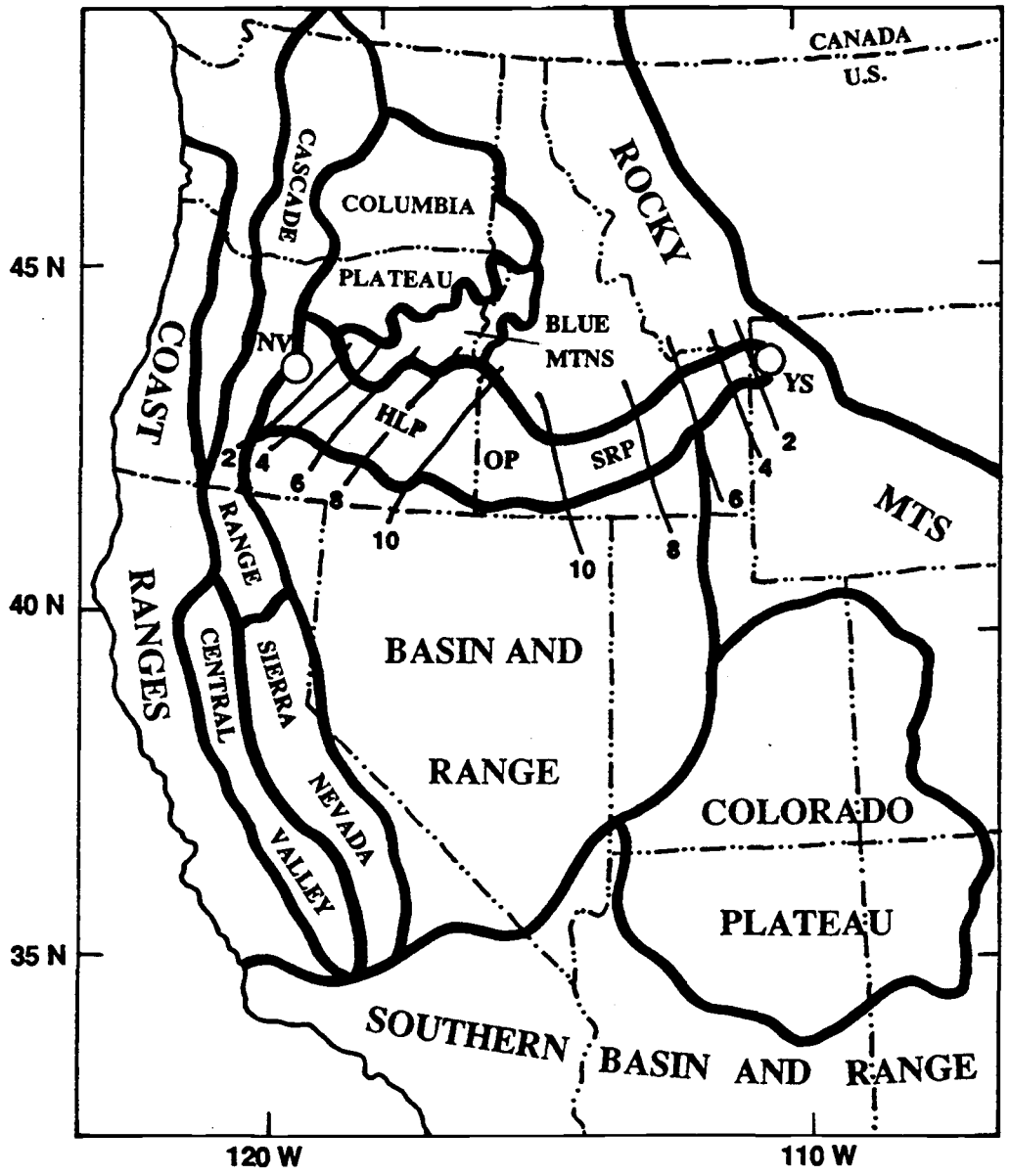

Figure 1.1: Map showing some of the main geologic provinces of the western United States and location of isochrons (in Ma) representing migration of silicic vents along the High Lava Plains (HLP) in southeastern Oregon and along the Snake River Plain (SRP) in southern Idaho. HLP isochrons are simplified from MacLeod et al. (1975), and SRP isochrons are derived from Armstrong et al. (1975). Other locations mentioned in text: NV, Newberry Volcano; OP, Owyhee Plateau; YS, Yellowstone.

abundances, flat to light rare-earth element-enriched rare-earth element patterns, and slightly elevated $^{87}Sr/^{86}Sr$ with respect to mid-ocean ridge basalt, several studies have suggested that they erupted due to lithospheric thinning and melting of the upper mantle in response to extension behind the Cascades volcanic arc (McKee et al., 1983; Carlson, 1984; Hart et al., 1984; Carlson and Hart, 1987).

Miocene to recent volcanism on the High Lava Plains is perhaps best known for its age progressive nature (MacLeod et al., 1975). Silicic rocks along the High Lava Plains in Oregon are progressively younger to the northwest (Fig. 1.2), from about 15 Ma in the Owyhee Plateau region near the intersection of Nevada, Oregon and Idaho (Malde and Powers, 1962; Armstrong et al., 1975), culminating in Holocene activity at the Newberry volcanic system (MacLeod and Sherrod, 1988). MacLeod et al. (1975) calculated rates of progression of 3.2 cm/yr from 10 to 5 Ma, and about 1 cm/yr from 5 Ma to the present. If the trend is considered to extend westward past Newberry, as proposed by Hill (1992), and extended eastward toward the Owyhee region, the rate of progression is 3 cm/yr from 15 Ma to the present. The age-progressive relationship of silicic volcanism is mirrored to the east, on the Snake River Plain, which terminates in the Yellowstone area. Age relations are considerably more complex on the Snake River Plain (Armstrong et al., 1975), but the timing and rates of migration of silicic centers appear to be similar, each showing a slight decrease in migration rate between 4 and 6 Ma (assuming that the Oregon trend ends at Newberry, as shown in Fig. 1.2). Miocene to Quaternary basaltic lavas along both trends are persistent, but not age-progressive. Primitive high-alumina basalts occur regularly throughout the stratigraphy of the High Lava and Snake River Plains provinces from 15 Ma to the present and are not age-progressive (Armstrong et al., 1975; Hart and Mertzman, 1982; Guffanti and Weaver, 1988).

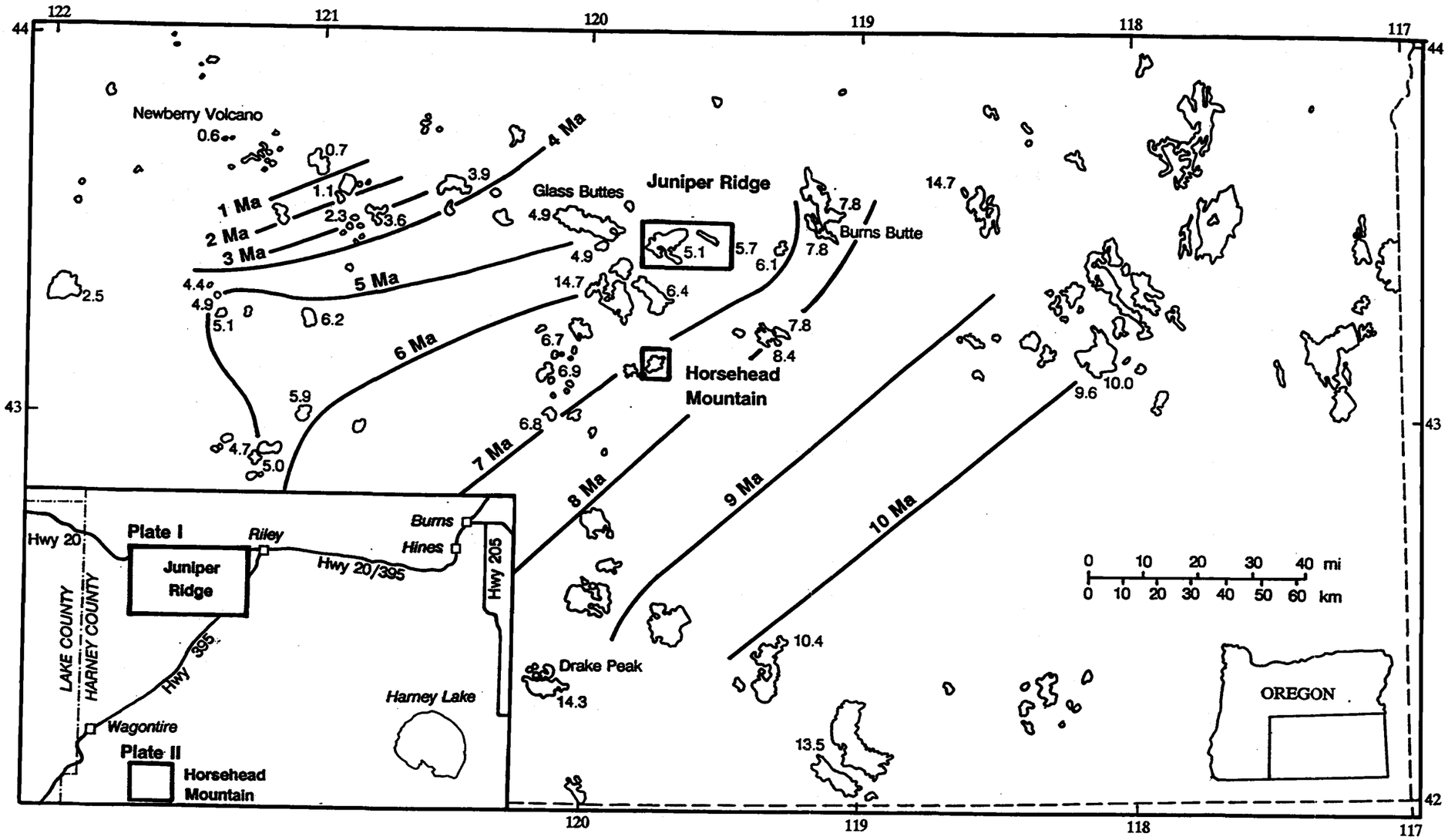

Figure 1.2: Map of southeastern Oregon, showing locations and ages of silicic volcanic complexes and isochrons for silicic volcanism in Ma (modified from Luedke and Smith, 1982). Inset shows locations of Juniper Ridge and Horsehead Mountain with respect to cultural and geographic features. Heavy boxes outline locations of Plates I and II (Juniper Ridge and Horsehead Mountain, respectively).

1.4 Hypotheses for age-progressive volcanism on the High Lava Plains: Hotspot versus continental rifting

Age progression of silicic centers on the northern margin of the Basin and Range province has been ascribed to various plate tectonic interpretations. Several studies, starting with Armstrong et al. (1969), have attributed time-transgressive volcanism and its concentration toward province margins to heating and ductile behavior of the lithosphere during extensional mantle upwelling (see also Christiansen and McKee, 1978). In this model, hot, plastic crust in the interior of the province prevented the eruption of mantle-derived mafic magmas and associated crustal melts in a progressively wider zone of continental rifting. Wernicke et al. (1987) suggested that initiation of extension in the northern Basin and Range correlates to the degree and timing of late Cretaceous Cordilleran orogenic events. Thermal and gravitational instability generated by overthickened crust and late Cretaceous plutonism were relieved by subsequent crustal "relaxation," resulting in extension and magmatism. Although overthickening may have initiated crustal extension and calc-alkaline magmatism throughout the Great Basin in the early Cenozoic Era, most workers acknowledge that subsequent tectonic and magmatic events (i.e. broadening of the area of extension, accompanied by a change to bimodal magmatism starting in the mid-Miocene epoch) may have been influenced by plate tectonic interactions (Zoback and Thompson, 1978; Wernicke et al., 1987).

Based on the geochemical similarity of HAOT basalts to back arc basin basalts, and the position of southeastern Oregon behind the Cascades volcanic arc, Carlson and Hart (1987) concluded that age progression of rhyolites might be related to the development of a "keel" of progressively shallowing mantle in response to convection in the mantle wedge above the subducting Juan de Fuca plate. This theory is weakened by inordinate distance of High Lava Plains (and Snake River Plains) volcanism from the Cascades arc, the fact that the timing of the

age progressive trend shows no relation to the timing of subduction-related processes off the Oregon coast, and that orientation of the basalt plain is nearly perpendicular to the arc.

Another school of thought favors a hotspot origin for age-progressive volcanism along the Snake River Plain in Idaho, with the hotspot now located under the Yellowstone area. Geist and Richards (1993) outline a model first proposed by Duncan (1982) in which the hotspot, located in the forearc of the Cascades in the Eocene epoch (Duncan et al. 1992), was subducted under the Oregon coast at about 48 Ma and re-emerged in southeastern Oregon at about 17 to 15 Ma. In this scenario, a portion of the plume was deflected northward by oblique subduction to form the Columbia River flood basalts, and the effects of the remainder of the plume were shut off for 30 Ma while it was trapped beneath the subducting slab. In addition to timing problems, a major drawback to the hotspot theory is that it fails to account for the lack of age progression among basalts or the mirror image of the Snake River trend in southeastern Oregon. Recently Draper (1991) theorized that the Oregon trend represents the expansion of the trailing edge of the Yellowstone hotspot as it intercepted the base of the crust at about 18 Ma.

In considering these conflicting hypotheses, volcanism in southeastern Oregon and southwestern Idaho needs to be examined in the context of the volcano-tectonic development of the entire Basin and Range province. Time-space patterns of volcanism compiled by Stewart and Carlson (1976) and again summarized by Seedorff (1991) reveal several province-wide volcanic episodes (Fig. 1.3), including (1) an early episode of diffuse volcanism centered on east-central Nevada from 43 to 34 Ma, (2) a southward sweeping belt of of intermediate to silicic, calc-alkaline volcanism from 34 to 17 Ma, and (3) progressive migration of volcanism to the margins of the province starting at about 15 to 17 Ma, coinciding with a transition in chemical character of the eruptive rocks from calc-alkaline to bimodal (basalt and rhyolite) or "fundamentally basaltic" (Christiansen and McKee, 1978). Until recently, the calc-alkaline phase had been considered to be related to subduction of the Farallon Plate, and the transition to bimodal

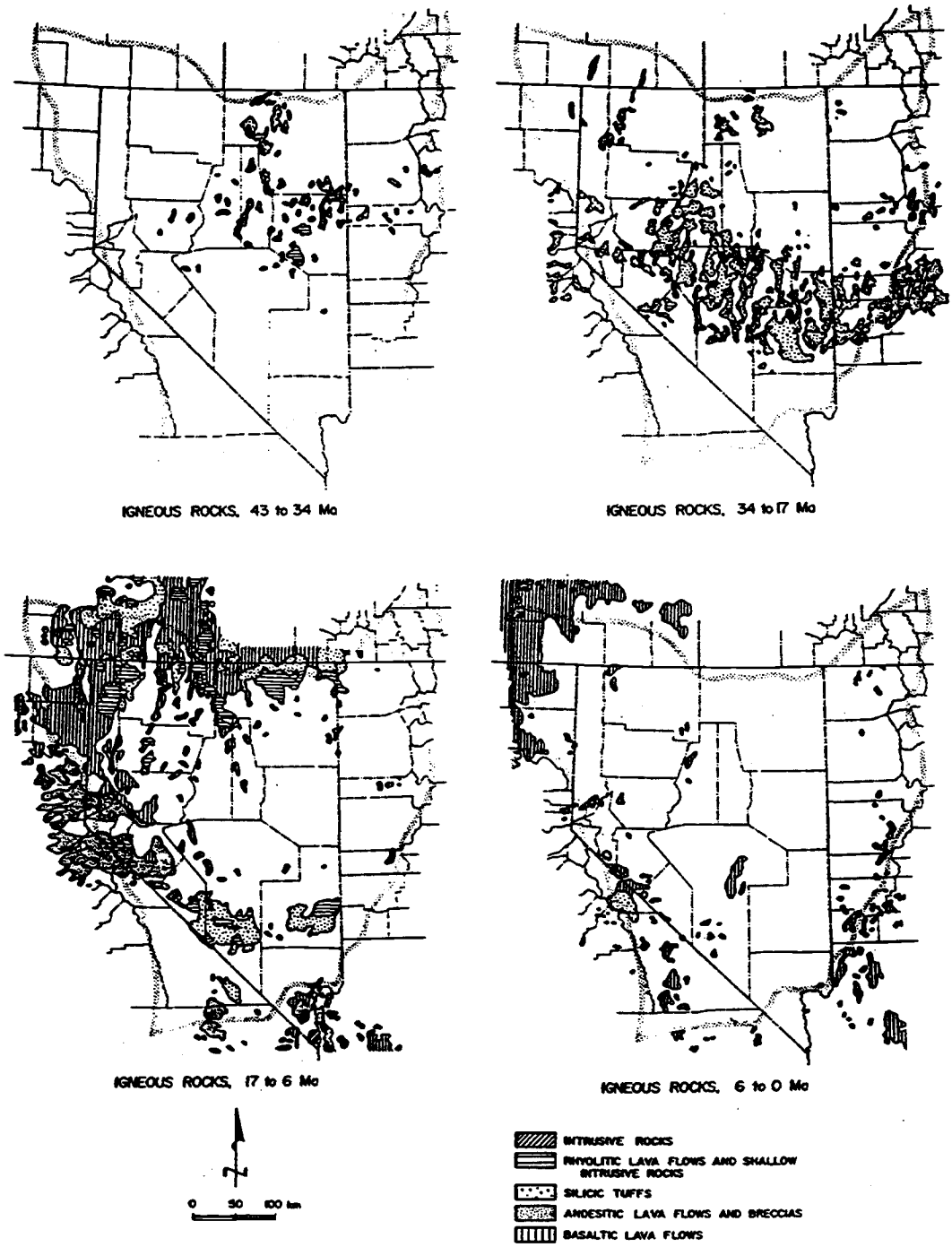

Figure 1.3: Four stages of mid- to late Tertiary volcanism in the Basin and Range province, after Seedorff (1991). Volcanism prior to about 17 Ma is largely intermediate to silicic and is calcalkaline in chemistry; after 17 Ma it is bimodal, consisting mainly of basalt and rhyolite (Christiansen and McKee, 1978; Hart and Carlson, 1988). Additional data on volcanic rocks in southeastern Oregon Idaho was compiled from Luedke and Smith (1982), Langer (1992), and Mathis (1993). Shaded line represents approximate boundary of the Great Basin portion of the Basin and Range province.

volcanism was attributed to the development of a transform system along the western margin of North America, resulting in extension in the continental interior (Atwater, 1970; Christiansen and Lipman, 1972; Snyder et al., 1976). However, as Gans et al. (1989) and Seedorff (1991) point out, mid-Tertiary magmatism in the northern Basin and Range is much farther inland than that of any modern arc, and the direction of migration of volcanism during the inception of the San Andreas transform is opposite the direction of migration of the Mendocino triple junction. Therefore, magmatism in the northern Basin and Range, and consequently on the High Lava Plains, is not necessarily directly dependent on the plate tectonic history of the western margin of the continent.

In view of the discussion above, the rifting model (e.g. Christiansen and McKee, 1978) is probably the most reasonable in explaining the time-space variations in volcanism and faulting in the Basin and Range province in that migration of silicic magmatism on both the High Lava Plains and the Snake River Plain can be explained as a part of province-wide migration of volcanism to the margins of the Basin and Range. For the purposes of this study, therefore, volcanism on the High Lava Plains will be considered in terms of a crustal rifting model, in which magmatic processes such as basaltic underplating and crustal melting are the primary controls on production and evolution of silicic magma.

One of the goals of this thesis is to address the connection between extensional tectonics and the generation of silicic melts. If the timing and style of rhyolite petrogenesis can be related to the timing and degree of extension in the northern Great Basin, the hypotheses that southeastern Oregon volcanism is merely a backarc to the High Cascades and that Snake River Plain volcanism is merely a hotspot track are called into question.

CHAPTER TWO: STRATIGRAPHY AND STRUCTURE AT JUNIPER RIDGE

Two distinct suites of volcanic rocks are exposed at Juniper Ridge. To the west of the Tin Mine fault (Fig. 2.1; Plate I), voluminous high-silica rhyolite and minor hybrid andesite and dacite flows form low hills and buttes that are dissected by northwest-trending faults of the Brothers fault zone; to the east of the Tin Mine fault lies a diverse suite of basalt through low-silica rhyolite exposed along the steep, east-west trending normal fault that bounds the north margin of Juniper Ridge. Although relative ages of the two suites cannot be established by field relations, both underlie the regionally extensive plateau-forming basalts.

About 25 to 30 km^2 of rhyolite lava are exposed at Juniper Ridge, corresponding to a volume of approximately 2.5 to 3 km^3, assuming an average total thickness of 100 meters (exposures generally range from a few tens to a few hundreds of meters). This estimate is conservative, because much more rhyolite is undoubtedly buried beneath alluvium and colluvium. Based on field exposure, the volume of rhyolite erupted at western Juniper Ridge may be as much as ten times that erupted at eastern Juniper Ridge.

Field relationships at eastern and western Juniper Ridge are described in this chapter, along with short summaries of the field appearance and petrographic characteristics of each map unit. Detailed petrographic descriptions are in Appendix 1.

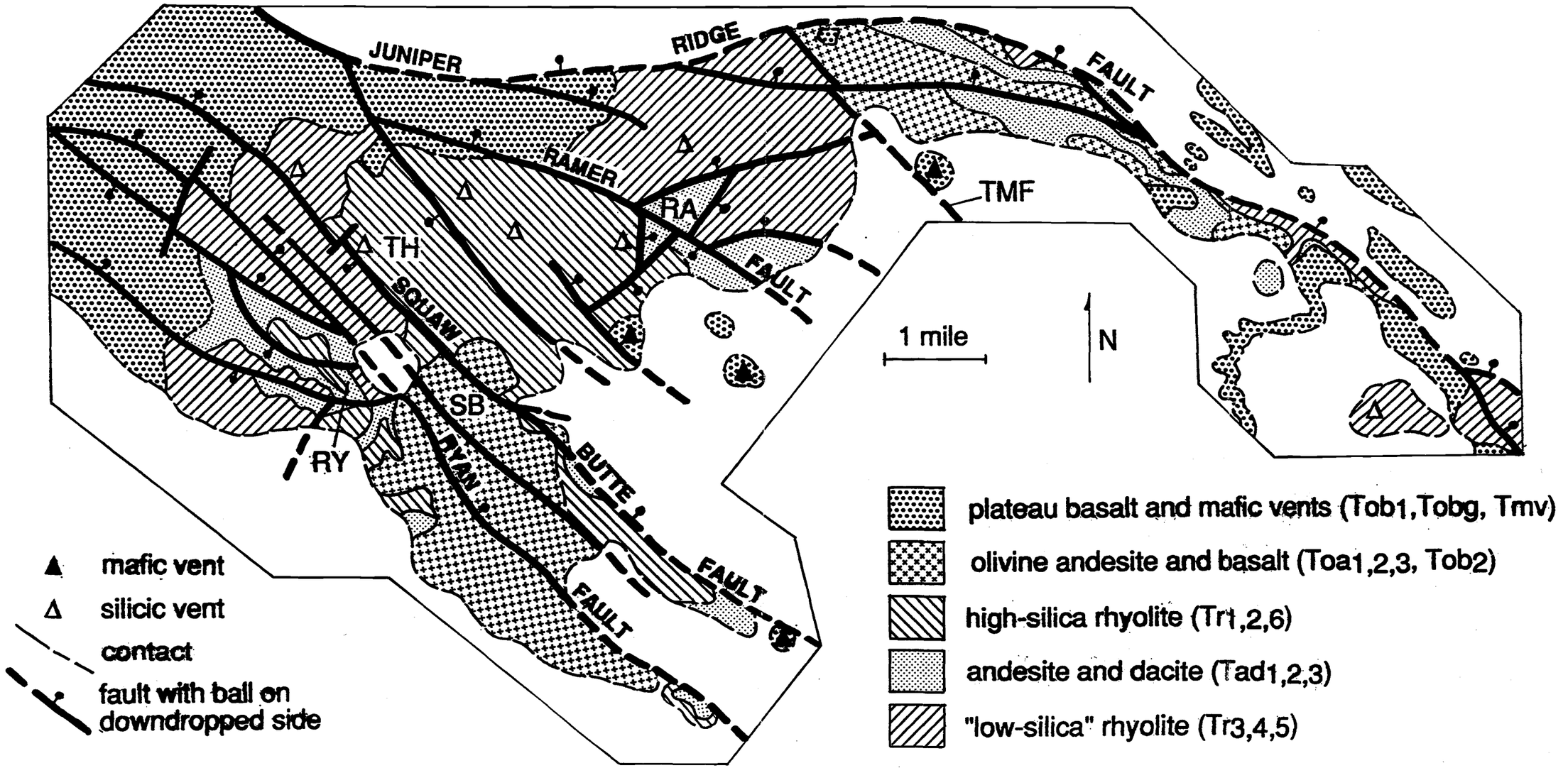

Figure 2.1: Simplified geology and structure map of the Juniper Ridge area, showing rock types, location and offset of faults, and suspected vent locations. RY = Ryan Peak; TH = Thomas Peak; SB = Squaw Butte; RA = Ramer Peak; TMF = Tin Mine fault.

2.1 Younger Units and Quaternary Units

2.1.1 Alluvium and colluvium (Qac, Ql): Quaternary cover at Juniper Ridge consists of thin veneering colluvium that blankets moderate to steep slopes, small landslide deposits along steep fault scarps, and minor alluvium in dry gullies and canyon openings. No attempt was made to break out these units in the field. Playa lake deposits in flat-lying areas were mapped by air photo as Ql.

2.1.2 High-alumina olivine tholeiite (Tob_1, Tobg, Tob_h): Plateau-forming diktytaxitic olivine tholeiite flows (Tobg; olivine basalt of Gum Boot Canyon, Greene et al., 1972) border Juniper Ridge to the north, west, and east, and are the youngest crystalline rocks exposed in the Juniper Ridge area. These basalts are part of a suite that Hart et al. (1984), refer to as high-alumina olivine tholeiites (HAOTs). HAOT flows overlie both eastern and western Juniper Ridge volcanic suites but are cut by faults of the Brothers fault zone. They are massive to blocky in outcrop, exhibiting well-developed columnar jointing and rare platy jointing. Individual flow units range in thickness from about 3 to 10 meters; some are as thick as 30 meters where exposed in paleocanyons. Multiple flows in some exposures can be distinguished by one- to two-meter-thick vesicular and/or clinkery zones at flow tops, which also locally display fluidal pahoehoe textures. Basal vesicular zones contain smaller vesicles and are only 10 to 20 centimeters thick.

Olivine is the primary phenocryst phase in the plateau basalts; plagioclase and clinopyroxene crystals rarely exceed groundmass size. Plagioclase, clinopyroxene and opaque oxides occur along with olivine in the groundmass. Euhedral plagioclase laths in the groundmass form an interlocking matrix, with olivine and oxide minerals in the spaces between feldspar laths. Clinopyroxene may be either intergranular or ophitic. Tob_1 is a porphyritic HAOT lava flow that overlies Tobg north of Porcupine Lake (Plate I). It contains large (up to one cm) feldspar laths enclosed in a groundmass identical to the underlying HAOT. At the eastern end of Juniper Ridge, Tobg and Tob_1 overlie a basaltic hyaloclastite (Tob_h), which ranges from a few

meters to about 30 meters thick. In proximal deposits (directly underlying basalt flows), Tob_h consists mainly of brown basaltic glass shards, with a few percent of euhedral olivine and plagioclase crystals and trace silicic glass shards. Farther from basalt outcrops, the amount of silicic material increases to over 50 percent, and includes clear glass shards, pumice, and minerals from unit Tr_4 in addition to brown basaltic glass. Thus, map unit Tob_h includes reworked tuffaceous sedimentary deposits, or perhaps small silicic pyroclastic deposits in addition to basaltic hyaloclastite.

2.1.3 Mafic vents (Tmv): Small cinder cones with minor lava flows are located mainly in the southeastern portion of the map area. No direct stratigraphic or age control is available, but most are probably about the same age as the plateau-forming flows, because topography suggests that they overlap older silicic flows but are truncated by northwest-trending faults. Basalts from the mafic vents are mostly scoriaceous, but also include small flows of dense olivine basalt or andesite that resemble plateau-forming basalts but are finer grained and not diktytaxitic.

2.2 Western Juniper Ridge (west of the Tin Mine fault)

2.2.1 Squaw Butte basaltic andesite (Toa_1): Squaw Butte is a small, partially eroded cone composed of thin basalt flows alternating with layers of scoria lapilli and bombs. Two 5- to 10-meter-thick basaltic dikes intersect at the summit (Plate I) and a small, blocky lava flow emanates from the west flank. Abundant scoria lapilli mantle the flanks of the peak. Lava flows that are petrographically and chemically identical to the Squaw Butte basaltic andesite surround Squaw Butte and are exposed in the scarp of the northwest-trending Ryan Peak fault (Fig. 2.1; Plate I). These flows are typically 10 to 15 meters thick and have coarsely vesicular, agglutinated and/or autobrecciated bases, finely vesicular to massive, coarsely jointed interiors, and coarsely vesicular tops. Flow textures in basaltic andesite flows are transitional between

plateau basalts and silicic andesite/dacite flows: the groundmass of the basaltic andesite is massive and aphanitic, but not as glassy as in dacite flows; jointing (both columnar and platy) is better developed, though not as well as in diktytaxitic basalt flows.

Basaltic andesite flows and dikes of Squaw Butte contain less than 10 percent phenocrysts of plagioclase and euhedral olivine in a fine-grained, pilotaxitic groundmass of plagioclase, glass, clinopyroxene, olivine and opaque oxides. Trace amounts of euhedral, prismatic apatite phenocrysts are also present.

Contact relations with surrounding silicic rocks are unclear, but at some locations Squaw Butte basaltic andesite flows appear to overlap or bank up against rhyolite outcrops.

2.2.2 High-silica rhyolite (Tr_1, Tr_2): Aphyric and crystal-poor high-silica rhyolite are the two dominant rock types at western Juniper Ridge: aphyric high-silica rhyolite (Tr_1) is restricted to Thomas Peak and a small outcrop just southeast of Squaw Butte (Fig. 2.1; Plate I); crystal-poor high-silica rhyolite (Tr_2) is more widespread but occurs mainly to the southwest of the Ramer Peak fault, and in the fault scarp to the southeast of Squaw Butte. Tr_1 overlies Tr_2 at Thomas Peak; elsewhere contact relations are not evident (stratigraphic diagram; Plate I).

High-silica rhyolite flows at western Juniper Ridge form relatively planar, thin lava flows with no evidence of explosive eruption (pyroclastic deposits are conspicuously absent). Contacts between flows in the high-silica rhyolite suite are usually obscured by colluvium, but exposed thicknesses of individual flows range from 5 to 30 meters. Total thickness of the rhyolite flows is unknown, but a water well drilled at Squaw Butte Ranch penetrated at least three flows of Tr_2 to a depth of about 200 meters. Outcrops are generally restricted to vertical cliffs at flow margins and fault scarps, therefore much of the rhyolite was mapped on the basis of black glass or pumiceous grey perlitic glass in the float.

Above a sharp contact with a coarsely vesicular, devitrified basal zone which is rarely exposed, stratigraphy within each flow unit consists of: (1) a lower spherulitic, lithophysal zone (1 to 10 meters), grading up into (2) a massive, devitrified, flow-banded zone (1 to 10 meters),

which is capped by (3) a carapace of gray pumiceous or perlitic glass (1 to 5 meters; Fig. 2.2). Lithophysae and spherulites in the lower zone truncate flow-banding, and therefore postdate emplacement of the flows. Small beads of black glass ranging from less than 1 mm to several centimeters in diameter occur between spherulites in the lower zones of some aphyric flows, and in float surrounding most aphyric flow units, but vitrophyre in crystal-poor flows is rare. The contact with the middle, flow-banded zone is gradational, with spherulites persisting to slightly higher levels in the middle zone than lithophysae. In the middle flow-banded zone, banding is subparallel on a scale of 2 to 4 meters; on a scale of 1 to 10 mm it is gently to isoclinally folded, contorted, and only locally planar. Layering is defined by finely spherulitic or vapor-phase altered vesicular zones separated by purplish-grey cryptocrystalline rhyolite. Where exposed, the upper 1 to 2 meters of the flow-banded zone is planar, often truncating folds in the the lower portion of the flow unit, but in general folding and contortion of laminations increase gradually downward.

Phyric high-silica rhyolite (Tr_2) contains 3 to 5 percent phenocrysts of sanidine, quartz, clinopyroxene, orthopyroxene, fayalite and oxide minerals, in descending order of abundance. Plagioclase occurs mostly as resorbed cores mantled by alkali-feldspar (anti-rapakivi texture). Trace zircon is also present. Olivine xenocrysts, along with rare inclusions of andesite and dacite, usually cored with large (up to 1 cm) feldspar crystals, occur in high-silica rhyolite flows, especially near the sharp basal contact with Tad_1, and attest to the involvement of both basaltic and rhyolitic magmas in the petrogenesis of Juniper Ridge (see Chapter 4).

2.2.3 Andesite and dacite (Tad_1): Black, flow-jointed andesite and dacite flows occur in several portions of western Juniper Ridge. All rocks mapped as Tad_1 contain abundant silicic inclusions and several percent large, glassy, Carlsbad-twinned feldspar phenocrysts, which are as long as 2 cm, but are more commonly 0.5 to 1 cm long. Although they are mapped as a single unit, based on similar stratigraphic position and field appearance, chemical and

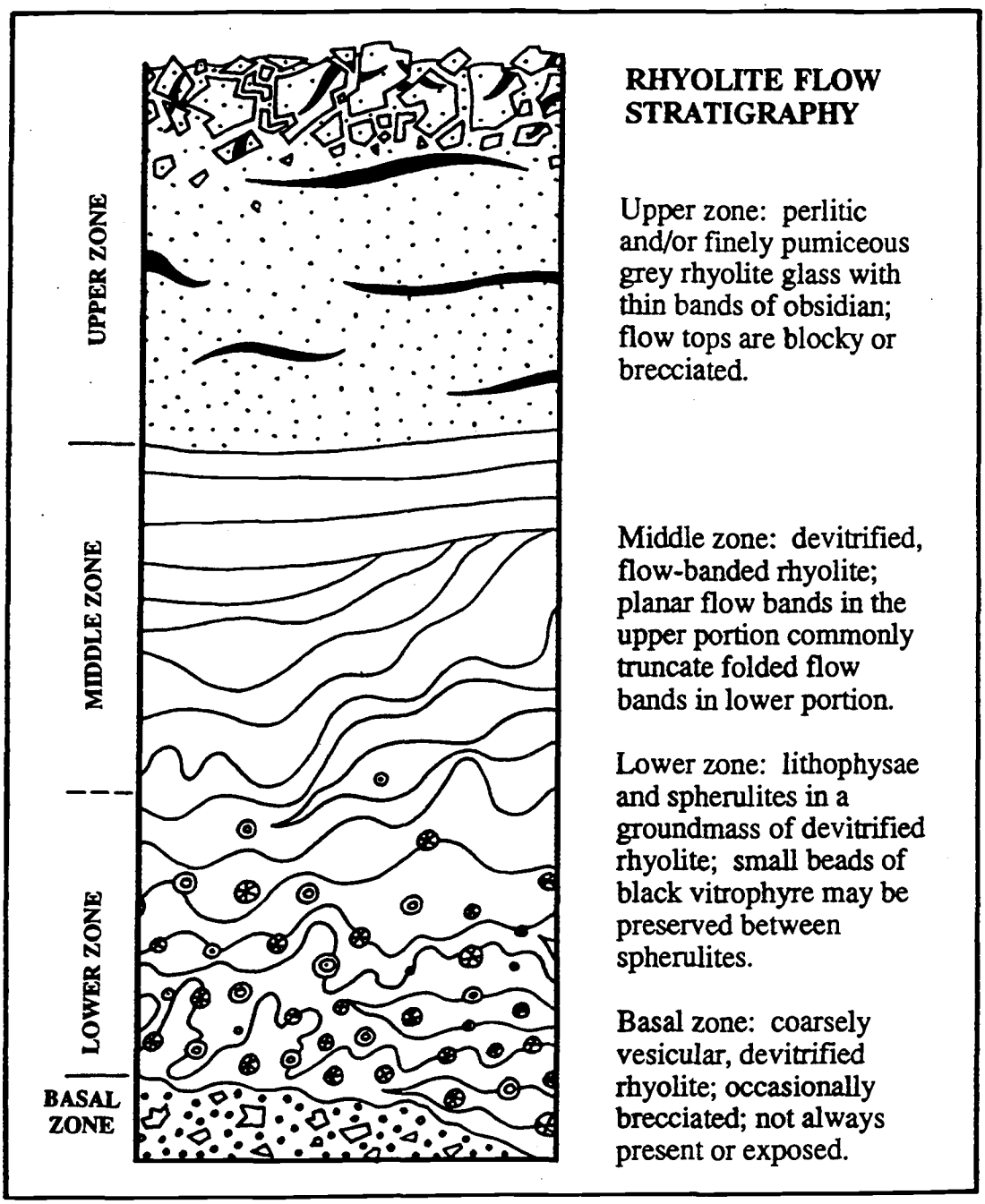

Figure 2.2: Composite sketch of internal stratigraphy of rhyolite flows at Juniper Ridge (includes map units Tr_1, Tr_2, Tr_3, Tr_4, and Tr_5. Not to scale: vertical dimension varies from a few tens of meters in high-silica rhyolite flows to a few hundreds of meters in lower-silica rhyolite flows. Further explanation in text.

petrographic analysis reveal at least two distinct types: (1) hybrid andesite in southwestern Juniper Ridge, and (2) glomerophyric andesite near Ramer Peak.

In the southwest part of the map area, an andesite flow with 3 to 4 percent large feldspar phenocrysts is closely associated in the field with high-silica rhyolite. The andesite is always found underlying rhyolite, and where exposed, the contact between the two seems mingled: irregular centimeter-scale fingers of andesite extend into the overlying rhyolite flow; flow banding in the overlying rhyolite mimics that in the andesite; and thin (less than 1 meter), irregular lenses of rhyolite with sharp to gradational contacts occur within the top 5 meters of andesite. The rhyolite lenses have major- and trace-element chemistry identical to high-silica rhyolite flows that overlie the andesite. The field relationships described above suggest that the andesite and rhyolite were erupted almost simultaneously, or possibly as a single zoned flow, implying that they were erupted from a zoned chamber or that the different magma types interacted shortly before or during eruption. Quartz xenocrysts in andesite and andesite inclusions in the overlying rhyolite are additional evidence for magma mixing, which is corroborated by chemical evidence presented in Chapters 3 and 4.

In the vicinity of Ramer Peak, andesite flows contain several percent glomerocrysts of plagioclase, olivine and clinopyroxene in a pilotaxitic groundmass. Andesite flows capping Ramer Peak lack large platy plagioclase crystals and quartz xenocrysts, but occur in the same stratigraphic position as Tad_1 flows to the southwest.

2.2.4 Lower-silica (microlitic and crystal-poor) rhyolite (Tr_3): Dense, aphyric black glass exposed at the western margin of Juniper Ridge (Tr_3) contains less than 0.5 percent small white specks that are either microcrystals or incipient spherulites, and is referred to here as microlitic rhyolite. To the east of the Ramer Peak fault, a series of crystal-bearing rhyolite flows with almost identical major and trace-element chemistry are also mapped as Tr_3. Crystal-bearing rhyolites at western Juniper Ridge (Tr_2 and Tr_3) are indistinguishable in the field, and were mapped on the basis of stratigraphic position and chemical composition.

Internal lithologic zonation within lower-silica rhyolite flows is identical to that in the high-silica rhyolites (Fig. 2.2), however, lower-silica rhyolite flows are on the average much thicker, ranging up to several hundred meters in the canyons near the Tin Mine area. On the western margin of Juniper Ridge, where the microlitic variety of Tr_3 predominates, rounded fragments of vitrophyre in float range up to 30 cm, increasing in size and abundance downward from the inferred upper contacts of some flow units. Microlitic glass is not found in outcrop, but by analogy to better exposed flows in the eastern part of Juniper Ridge, the glass probably weathered out of an upper flow zone of interlayered obsidian and pumice (see description of Tr_5 below and Fig. 2.2).

In comparison to crystal-bearing high-silica rhyolite (Tr_2), lower-silica rhyolite (Tr_3) contains more plagioclase and orthopyroxene, little or no quartz, fayalite or alkali feldspar, and contains pleochroic, biaxial (-) clinopyroxene (augite) rather than the non-pleochroic biaxial (+) variety (ferrohedenbergite) found in Tr_2.

Tr_3 underlies Tad_1 in the vicinity of Ryan Peak; at Ramer Peak, Tr_3 underlies a different andesitic flow, but is assumed to be coeval on the basis of identical chemistry to Tr_3 sampled from the western margin of Juniper Ridge.

2.3 Eastern Juniper Ridge (east of the Tin Mine fault)

Unlike western Juniper Ridge, where contact relations are typically unclear and relative stratigraphic positions are not well established, most rocks at eastern Juniper Ridge occur in a single, elongate fault scarp in which stratigraphic relations are clearly exposed (Fig. 2.1; Plate I). Unfortunately, none of the volcanic units from western Juniper Ridge, with the exception of the young, plateau-forming Tobg, occur to the east of the Tin Mine fault, so that age relations between western and eastern Juniper Ridge are impossible to determine in the field.

2.3.1 Glomerophyric olivine andesite (Toa_2): The uppermost unit in the volcanic stratigraphy of eastern Juniper Ridge, directly underlying and in conformable contact with Tobg, is a series of several flows of glomerophyric olivine andesite, characterized by radiate clusters of olivine and plagioclase up to one cm in diameter in a microcrystalline, subophitic groundmass. These flows are especially well-exposed in the eastern half of section 36 (T. 23 N, R. 25 E), where the unit has been quarried for road aggregate. Flows of glomerophyric olivine andesite are thin (3 to 5 meters), and often exhibit very thin (0.5 to 1 cm) platy jointing that becomes increasingly convoluted toward the base and margins of each flow.

2.3.2 Aphanitic olivine andesite (Toa_3): Underlying unit Toa_2 in the Juniper Ridge frontal scarp are several flows of dark gray, massive to platy-jointed andesite with less than one percent phenocrysts of olivine and plagioclase. Toa_3 is similar in field appearance to Tob_2, and is distinguished from the latter by stratigraphic position, differences in groundmass texture and whole-rock chemistry. Both are relatively thin (3 to 5 meters).

2.3.3 Andesite and dacite (Tad_2): To the east of the Tin Mine fault, andesite and dacite (Tad_2) are chemically and mineralogically different than andesite and dacite at western Juniper Ridge (Tad_1). Dacite, in particular, is glassier and contains equant, euhedral plagioclase phenocrysts instead of the large, tabular plagioclase that occurs in andesites and dacites to the west. Flow textures in eastern Juniper Ridge dacites more closely approximate those found in rhyolites: platy to poorly flow-banded, devitrified dacite underlies coarsely vesicular to pumiceous grey glass. Occasional fragments of waxy, black, partially spherulitic vitrophyre are found in the float. Dacite flows are exposed in the Juniper Ridge frontal scarp as well as in low, eroded domes to the south (Plate I).

Alkali feldspar, often exhibiting cross-hatched twinning, is the dominant phenocryst phase in dacites of unit Tad_2, accompanied by small amounts of plagioclase, pyroxene and oxide minerals. Olivine ranges up to one percent in the andesite flows of Tad_2, along with plagioclase, clinopyroxene and oxides.

2.3.4 Aphanitic olivine basalt (Tob_2): Underlying Tad_2 in the eastern Juniper Ridge fault scarp are several 3 to 5 meter thick, dark grey, massive lava flows with platy bases and slightly vesicular tops. These flows are almost aphyric, containing less than 1 percent crystals of plagioclase and olivine in an intergranular, intersertal, ophitic groundmass.

2.3.5 Phyric rhyolite (Tr_4): The lowermost unit exposed at eastern Juniper Ridge is a series of crystal-bearing, glassy, spherulitic or completely devitrified rhyolite flows that underlie Tob_2 in the Juniper Ridge fault scarp as well as a low dome-shaped hill to the east of Porcupine Lake (Plate I). The flows contain about 5 to 15 percent crystals of sanidine, plagioclase, pyroxenes and oxide minerals. Flow stratigraphy resembles that of high-silica rhyolite flows in western Juniper Ridge, except in the dome, where the unit is completely devitrified, and displays thin platy jointing that dips generally inward, concentric to the dome itself. Concentric jointing and dome-shaped morphology suggest a local rhyolite vent.

Beside being more crystal-rich than rhyolite flows in western Juniper Ridge, eastern Juniper Ridge rhyolites contain two populations of orthopyroxene (Chapter 3) and trace zircon, in addition to alkali feldspar, plagioclase and oxide minerals.

2.3.6 Aphyric rhyolite (Tr_5): Flows of aphyric black glass crop out at the extreme eastern end of Juniper Ridge where the scarp crosses Highway 395. The flows underlie Tobg, but are not in direct contact with other volcanic units in eastern Juniper Ridge. A roadcut along Highway 395 exposes the top 10 meters of one of the aphyric lava flows, which includes, from lower to higher in the flow: (a) banded devitrified aphyric rhyolite with occasional thin bands of waxy black glass; (b) perlitic grey glass interlayered with 2 to 10 cm thick bands of black obsidian, and (c) pumiceous, blocky perlitic glass, grading upward into unbedded vitric tuff and tuffaceous sediments, which probably represent collapsing of the unstable margins of the advancing flow, or perhaps near-vent explosion deposits.

2.4 Southern Juniper Ridge

Several samples were taken from the southeastern end of the ridge that is bounded on its northwest margin by the Ryan Peak fault. They are chemically dissimilar to rocks at Juniper Ridge (Chapter 3), and may be related instead to the rhyolites at Egli Ridge, which is only a few kilometers to the south.

2.4.1 Andesite and dacite (Tad_3): The southeastern end of the ridge is capped by a black, plagioclase-phyric dacite flow that includes a lower agglutinate zone overlain by a platy zone, a zone of black, waxy vitrophyre, and a scoriaceous top. Alkali feldspar, light green, non-pleochroic clinopyroxene and opaque oxides are present in addition to plagioclase.

2.4.2 Aphyric rhyolite (Tr_6): Voluminous small beads of aphyric black glass, most 1 to 2 cm in diameter but ranging up to 20 cm long, occur in the float directly under Tad_3. Although no outcrops are present, it is inferred that a rhyolite flow underlies the southeastern end of the ridge.

2.5 Structure

Although the Brothers fault zone (BFZ) is an important structural boundary, little work has been done to characterize the nature of individual BFZ faults. Mapping by Donath (1962) near Summer Lake and by Clayton (1989) at Horse Ridge, in the western part of the High Lava Plains, suggest that the sense of displacement of BFZ faults is primarily, if not exclusively, normal, but because of lack of stratigraphic markers and degree of erosion at Juniper Ridge, faulting relations at Juniper Ridge are only locally clear. Continuity of faults through the silicic volcanic pile and into the younger plateau basalts indicates that most, and probably all, faulting post-dates volcanism.

Topographic expression and outcrop patterns at Juniper Ridge are controlled mainly by subparallel northwest-trending faults that are parallel to the general trend the Brothers fault zone. A second group of faults stikes approximately northeast, and the main frontal fault that defines Juniper Ridge runs east-west before turning southeast toward Highway 395 (Fig. 2.1). Linear truncation of hillslopes, linear topographic features such as scarps and cliffs, and silicification were used to locate faults in the field. Only rarely could offset lava flows be used to recognize stratigraphic separation by faulting, except in the case of the Juniper Ridge fault, which has at least 60 meters of normal displacement, based on the offset of the plateau-forming lava (Tobg) at the eastern end of Juniper Ridge.

Some northwest-trending, through-going faults have apparently opposite offset on opposite ends of the same fault, i.e. the Squaw Butte fault, which has apparent down-to-the-northeast offset on its northwest end, and apparent down-to the-southwest offset near the vicinity of Thomas Peak (Plate I). A switch in the direction of apparent offset can be produced by either "scissors"-type (hinge) faulting, or by strike-slip faulting that juxtaposes lithologies with different resistance to erosion or topographic elevation. Alternatively, the nature of faulting at Juniper Ridge may be explained by a third faulting mechanism, described by Donath (1962) for faults in the nearby Summer Lake area, where redistribution of principal stress axes produced vertical dip-slip offset on previously existing conjugate strike-slip shears. In Donath's model, a horizontal principal stress field produced a series of independent polygonal fault blocks that were subsequently uplifted or downdropped to different degrees relative to neighboring blocks when the stress was relieved, resulting in complex and apparently contradictory fault displacements. At Juniper Ridge, the presence of two main fault directions at approximately 30 and 60 degree angles to each other and reversal of offset on different parts of the same fault support a similar mechanism. Northwest-trending faults at Juniper Ridge are longer and more continous, suggesting that strike slip faulting may have occurred after formation of the conjugate sets.

CHAPTER THREE: GEOCHRONOLOGY AND GEOCHEMISTRY

Rock samples from eastern and western Juniper Ridge were collected for purposes of stratigraphic correlation, petrographic analysis, geochemistry and age determinations (geochemical samples are located on Plate I; complete sample list and locations are in Appendix 2). To determine the age span of silicic volcanism at Juniper Ridge, dating was performed on three samples, including the oldest, easternmost rhyolite at eastern Juniper Ridge, and the youngest rhyolite at western Juniper Ridge. For use in geochemical modelling (Chapter 4) and regional chemical comparisons (Chapter 5), whole-rock chemical analyses were obtained from representative samples of each volcanic unit, and mineral compositions were determined from major phases within each rock type.

3.1 Geochronology

Age determinations for Juniper Ridge and Horsehead Mountain were done by Alan Deino at the Geochronology Center of the Institute for Human Origins using the single-crystal, laser-fusion $^{40}Ar/^{39}Ar$ method (Table 3.1, Table 6.1). Results for Horsehead Mountain are described in Chapter 6; results for three Juniper Ridge samples show that eastern Juniper Ridge rhyolites are about 1 Ma older than western Juniper Ridge rhyolites, in keeping with the age-progressive trend. Fifteen sanidine analyses from sample HP-91-13, a sparsely phyric, high-silica rhyolite from map unit Tr_2, yielded a weighted mean age of 5.70 ± 0.02 Ma (Table 3.1). The unit is geochemically similar to the aphyric rhyolite (Tr_1) which caps the sequence at western Juniper Ridge (Plate I), and which yielded a weighted mean average age of 5.72 ± 0.02 Ma (sample JR-92-25). A sample of aphyric rhyolite (JR-92-56) from the easternmost, stratigraphically lowest rhyolite (unit Tr_5) at eastern Juniper Ridge gave a weighted mean average age of 6.87 ± 0.02 Ma.

The new $^{40}Ar/^{39}Ar$ data, including other dates collected by Grunder and Deino (Chapter 5) confirm the younger-to-the-northwest age trend of MacLeod et al. (1975), but yield ages that are 0.5 to 1 Ma older than previous K-Ar ages. For example, McKee and Walker (1976) published K-Ar ages of 5.12 ± 0.08 Ma for an aphyric, vitric rhyolite at western Juniper Ridge (map unit Tr_3?), and 5.70 ± 0.7 Ma for an aphyric rhyolite glass at the extreme eastern end of Juniper Ridge (map unit Tr_5). The anomalously young whole-rock K-Ar ages may have resulted from argon loss during hydration.

TABLE 3.1: ^{40}Ar-^{39}Ar Analytical Data for Juniper Ridge Samples

Lab ID#	Ca/K	$^{36}Ar/^{39}Ar$	$^{40}Ar^*/^{39}Ar$	$\%^{40}Ar^*$	Age (Ma) ±1σ
Sample HP-91-13					
5364-07	0.092	0.00052	0.626	78.4	5.63 ± 0.03
5362-02	0.070	0.00024	0.627	87.3	5.63 ± 0.02
5364-05	0.108	0.00031	0.629	85.3	5.65 ± 0.04
5362-04	0.056	0.00033	0.631	84.5	5.66 ± 0.03
5364-08	0.047	0.00027	0.631	86.5	5.67 ± 0.03
5364-03	0.079	0.00046	0.632	80.4	5.68 ± 0.05
5364-04	0.049	0.00019	0.634	89.2	5.69 ± 0.03
5364-02	0.066	0.00015	0.634	91.0	5.70 ± 0.02
5364-01	0.054	0.00018	0.635	89.9	5.71 ± 0.02
5362-03	0.045	0.00014	0.635	91.1	5.71 ± 0.02
5364-06	0.191	0.00032	0.638	85.4	5.73 ± 0.05
5362-07	0.056	0.00014	0.638	91.2	5.73 ± 0.02
5362-06	0.054	0.00025	0.640	87.1	5.75 ± 0.04
5362-01	0.060	0.00018	0.640	89.6	5.75 ± 0.02
5362-05	0.057	0.00019	0.641	89.5	5.76 ± 0.02
			Weighted average=		5.70 ± 0.02

Notes: Errors in age quoted for individual runs are 1σ analytical uncertainty. Weighted averages are calculated using the inverse variance as the weighting factor (Taylor, 1982), while errors in the weighted averages are 1σ standard error of the mean and incorporate error in *J* (see below) (Samson and Alexander, 1987). Ca/K is calculated from $^{37}Ar/^{39}Ar$ using a multiplier of 1.96. $^{40}Ar^*$ refers to radiogenic argon. $\lambda = 5.543 \times 10^{-10}\ y^{-1}$. Isotopic interference corrections: $(^{36}Ar/^{37}Ar)_{Ca} = (2.58 \pm 0.06) \times 10^{-4}$, $(^{39}Ar/^{37}Ar)_{Ca} = (6.7 \pm 0.3) \times 10^{-4}$, $(^{40}Ar/^{39}Ar)_K = (2.19 \pm 0.02) \times 10^{-2}$. $J = (4.986 \pm 0.010) \times 10^{-3}$.

TABLE 3.1 (continued)

Lab ID#	Ca/K	$^{36}Ar/^{39}Ar$	$^{40}Ar^*/^{39}Ar$	$\%^{40}Ar^*$	Age (Ma) ±1σ
Sample JR-91-25					
7488-01	0.0437	0.00033	0.940	90.6	5.66 ± 0.03
7488-09	0.0478	0.00040	0.941	88.9	5.67 ± 0.03
7488-06	0.0477	0.00064	0.947	83.5	5.70 ± 0.03
7488-10	0.0436	0.00042	0.947	88.5	5.70 ± 0.03
7488-08	0.0450	0.00052	0.948	86.1	5.71 ± 0.03
7488-04	0.0478	0.00064	0.948	83.5	5.71 ± 0.03
7488-05	0.0462	0.00068	0.954	82.7	5.74 ± 0.03
7488-03	0.0428	0.00033	0.955	91.0	5.75 ± 0.03
7488-07	0.0436	0.00049	0.959	86.9	5.77 ± 0.03
7488-02	0.0446	0.00055	0.963	85.6	5.79 ± 0.03
	Weighted average, 1σ error without error in J=				5.72 ± 0.01
	1σ error with error in J=				± 0.02
Sample JR-92-56					
7492-01	0.0942	0.00006	1.138	98.7	6.82 ± 0.03
7492-06	0.0927	0.00010	1.140	97.9	6.83 ± 0.04
7492-03	0.0940	0.00028	1.141	93.4	6.84 ± 0.03
7492-09	0.0939	0.00009	1.142	98.1	6.84 ± 0.03
7492-05	0.0936	0.00007	1.144	98.4	6.85 ± 0.03
7492-07	0.0937	0.00007	1.144	98.6	6.86 ± 0.03
7492-10	0.0938	0.00005	1.144	98.9	6.86 ± 0.03
7492-08	0.0939	0.00006	1.149	98.8	6.88 ± 0.03
7492-04	0.0915	0.00004	1.157	99.3	6.94 ± 0.04
7492-02	0.0942	0.00004	1.159	99.3	6.95 ± 0.03
	Weighted average, 1σ error without error in J=				6.87 ± 0.01
	1σ error with error in J=				± 0.02

Notes: Errors in age quoted for individual runs are 1σ analytical uncertainty. Weighted averages are calculated using the inverse variance as the weighting factor (Taylor, 1982), while errors in the weighted averages are 1σ standard error of the mean (Samson and Alexander, 1987). Ca/K is calculated from $^{37}Ar/^{39}Ar$ using a multiplier of 1.96. $^{40}Ar^*$ refers to radiogenic argon. $\lambda = 5.543 \times 10^{-10}\ y^{-1}$. Isotopic interference corrections: $(^{36}Ar/^{37}Ar)_{Ca} = (2.64 \pm 0.02) \times 10^{-4}$, $(^{39}Ar/^{37}Ar)_{Ca} = (6.7 \pm 0.3) \times 10^{-4}$, $(^{40}Ar/^{39}Ar)_K = (7 \pm 3) \times 10^{-4}$. $J = (3.342 \pm 0.010) \times 10^{-3}$ for JR-91-25, and $(3.328 \pm 0.010) \times 10^{-3}$ for JR-92-56.

3.2 Mineral Chemistry and Geothermometry

3.2.1 Methods: Mineral compositions for the volcanic suite at Juniper Ridge were obtained by electron microprobe analysis at Oregon State University, using a fully automated Cameca SX-50 microprobe with wave-length-dispersive spectrometers. Precision estimates were determined from repeat analyses of standards run as unknowns from all analytical sessions; analytical drift during each session was smaller than precision error. For western Juniper Ridge rhyolites, all of which are crystal-poor, probe analyses were performed on polished grain mounts of mineral separates obtained by heavy liquid (sodium polytungstate) density separation. All other analyses were done on polished thin sections.

In order to document compositional variation within the suite and for use in models of geochemical processes (Chapter 4), the following samples were chosen to represent each of the major petrologic groups at Juniper Ridge:

Plateau basalt	
porphyritic (Tob_1)	JR-92-59
nonporphyritic (Tobg)	JR-92-53
Squaw Butte basaltic andesite (Toa_1)	JR-91-21
Western Juniper Ridge	
high-silica rhyolite (Tr_2)	JR-91-13,18
lower-silica rhyolite (Tr_3)	JR-91-34
andesite (Tad_1)	JR-91-11
Eastern Juniper Ridge	
rhyolite (Tr_4)	JR-92-48
andesite (Toa_3)	JR-91-42

Feldspar, pyroxene, olivine and oxide minerals make up the bulk of the mineral assemblage in the Juniper Ridge suite. Representative or average analytical results for each of these mineral groups along with analytical conditions and precision estimates are in Tables 3.2 to 3.6. Complete microprobe data are available in Appendix 3.

3.2.2 Feldspar: Most feldspars lack pronounced or systematic zonation. In most cases, zonation is restricted to the outer 0 to 10 microns of the crystal, so that rim analyses were difficult to obtain. Compositions in Table 3.2 are all core analyses, and compositions in Figure 3.1 are a mix of core and rim analyses.

Plagioclase compositions range from oligoclase in lower-silica rhyolite at western Juniper Ridge to bytownite in the regional plateau basalts (Table 3.2 and Fig. 3.1). In plagioclase BaO increases with whole rock SiO_2 (see discussion in Section 3.2.6); SrO content was below detection limits for all samples.

Regional plateau basalts contain fairly uniform feldspar compositons ranging from bytownite (An_{74}) to labradorite (An_{65}), with a few anomalous andesine compositions (An_{48} and An_{52}; Fig. 3.1). Large plagioclase megacrysts in the porphyritic basalt (JR-92-59) and in the hybrid western Juniper Ridge andesite are compositionally identical to groundmass plagioclase in the non-porphyritic basalt. The olivine andesite from eastern Juniper Ridge contains a wide range of feldspar compositions, from An_{45} (small euhedral crystals) to An_{77} (larger, subhedral crystals), in contrast to the Squaw Butte basaltic andesite, which contains relatively homogeneous andesine (An_{44} to An_{52}), despite similar variations in grain size and morphology (Chapter 2).

Oligoclase compositions from lower-silica rhyolite at western Juniper Ridge cluster tightly around An_{30}, while the eastern Juniper Ridge sample (JR-92-48) displays a range of compositions from An_{28} to An_{65} (Fig. 3.1). Larger, blockier, concentrically zoned, subhedral feldspars in JR-92-48 tend to be sodium-rich; smaller, unzoned, euhedral feldspars are more calcic.

Sodic sanidine (Or_{31} to Or_{48}) was found only in high-silica rhyolite from western Juniper Ridge. Sanidine extracted from sample JR-91-13 (Or_{31} to Or_{44}), the most evolved of the phyric high-silica rhyolites, is on average slightly more sodium-rich than that from JR-91-18 (Or_{37} to Or_{48}), the least evolved composition of the same unit. BaO content in sanidine correlates

TABLE 3.2: Representative microprobe analyses of feldspar

sample #	JR-91-13	JR-91-18	JR-91-34	JR-91-21	JR-91-21	JR-91-11
map unit	Tr_2	Tr_2	Tr_3	Toa_1 (+)	Toa_1 (-)	Tad_1 (+)
SiO_2	66.60	64.95	61.88	57.38	56.20	50.29
Al_2O_3	19.48	19.95	24.04	26.40	27.68	31.10
FeO_{TOT}	0.16	0.17	0.16	0.34	0.41	0.45
MgO	n.d.	0.01	n.d.	0.03	0.05	0.13
CaO	0.19	0.39	5.51	8.56	9.96	14.12
Na_2O	5.94	6.22	7.56	5.97	5.37	3.24
K_2O	7.41	6.15	0.71	0.46	0.38	0.05
BaO	0.21	1.54	0.09	0.07	0.05	0.01
Total	99.99	99.38	99.95	99.21	100.10	99.39
Ab	54	59	68	54	48	30
Or	45	39	5	3	2	0
An	1	2	27	43	50	70

sample #	JR-92-48	JR-92-48	JR-91-42	JR-91-42	JR-92-59	JR-92-53
map unit	Tr_4 (+)	Tr_4 (-)	Toa_3 (+)	Toa_3 (-)	Tob_1 (+)	Tobg (-)
SiO_2	59.14	52.32	49.89	56.57	49.96	51.51
Al_2O_3	25.56	30.08	31.49	26.81	31.28	30.55
FeO_{TOT}	0.20	0.49	0.28	0.47	0.51	0.51
MgO	n.d.	0.06	0.08	0.07	0.21	0.12
CaO	7.41	12.73	14.52	9.21	14.44	13.45
Na_2O	6.70	3.95	3.22	5.87	3.15	3.59
K_2O	0.66	0.23	0.11	0.37	0.07	0.12
BaO	0.12	0.06	0.03	0.07	n.d.	0.03
Total	99.79	99.92	99.62	99.44	99.62	99.88
Ab	60	35	28	52	28	32
Or	4	1	1	2	0	1
An	36	64	71	46	72	67

n.d. = not detected. FeO_{TOT} = total iron as FeO. (+) and (-) refer to large and small phenocrysts in samples with distinct size variations. Beam conditions: beam current, 30 na; accelerating voltage, 15 kv; beam diameter, 5 microns; counting time, 10 sec. for all elements except for Ba (20 sec.). Analytical precision based on repeat analyses of standards (KANO, n=29; LABR, n=26; SANI, n=10) is better than 1% (1 sigma s.d.) for SiO_2, Al_2O_3, K_2O (sanidine) and CaO (labradorite), better than 5% for Na_2O, K_2O (oligoclase), CaO (oligoclase) and BaO (sanidine), and better than 10% for FeO (labradorite). Other values are at or below detection limit. Ternary feldspar compositions: Ab = albite ($NaAlSi_3O_8$); Or = orthoclase ($KAlSi_3O_8$); An = anorthite ($CaAl_2Si_2O_8$).

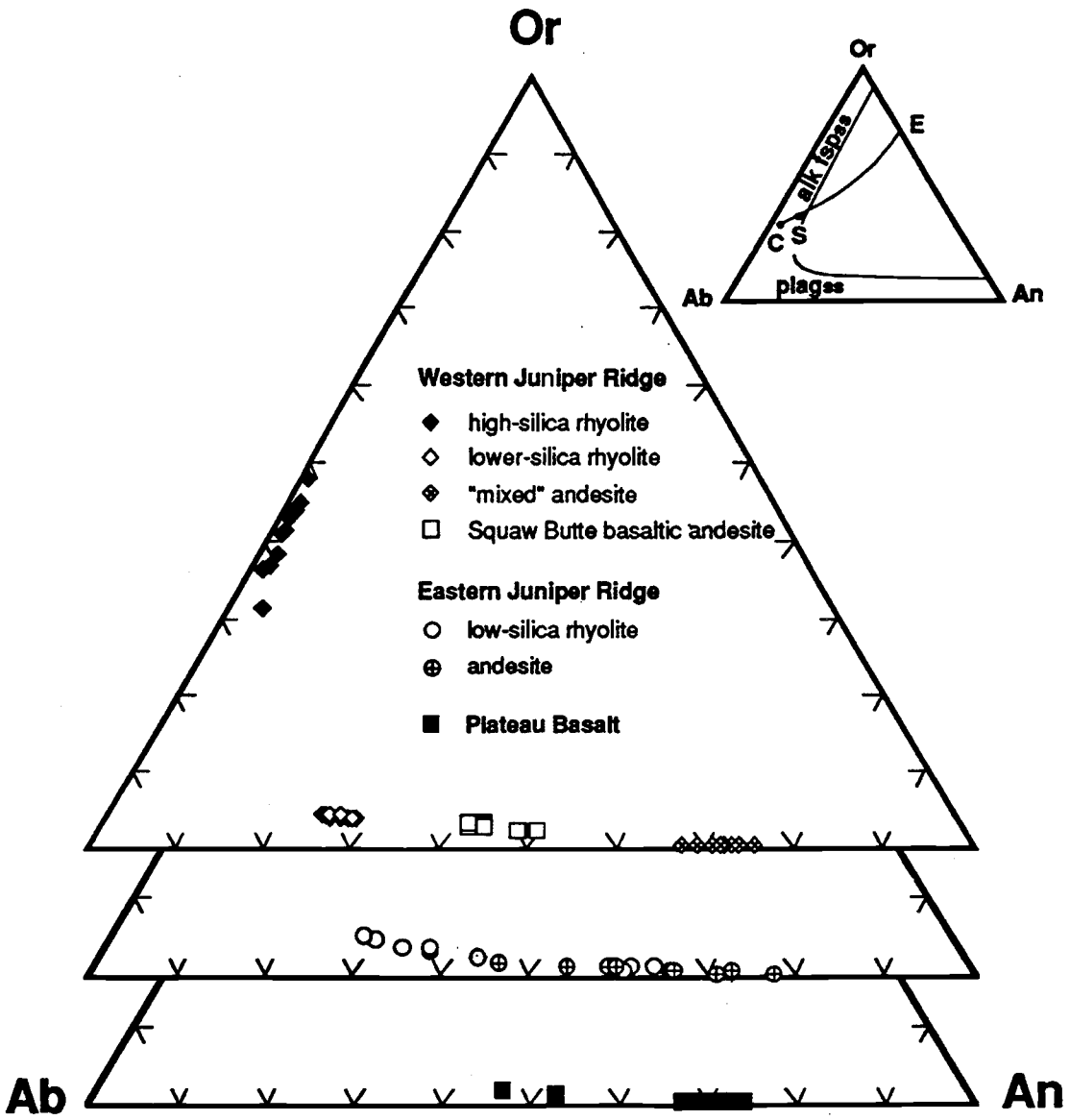

Figure 3.1: Feldspar compositions from Juniper Ridge rocks plotted on the feldspar ternary diagram. Or = orthoclase; Ab = albite, An = anorthite. Inset (above right) shows fields for plagioclase ($plag_{ss}$) and alkali feldspar (alk fsp_{ss}) and liquidus phase relationships. Point E is the binary eutectic on the An-Or join, point C represents the critical end-point, and S is the neutral point (terminology of Abbott, 1978). From E to S, the two-feldspar boundary is cotectic (two feldspars crystallize); from S to C the line is peritectic (alkali feldspar forms at the expense of plagioclase under silica-saturated conditions); at C, only alkali feldspar crystallizes.

positively with whole rock Ba content, and SrO content is below detection limits for all sanidine analyses. Alkali feldspar is present in more-evolved low-silica rhyolites at eastern Juniper Ridge and lower-silica rhyolites at western Juniper Ridge (Chapter 2), but is present only in trace amounts in the less-evolved rhyolites that were analyzed by microprobe.

3.2.3 Pyroxene: Clinopyroxene compositions (Table 3.3, Fig. 3.2a) in the Juniper Ridge suite range from augite to ferrohedenbergite, and are systematically more iron-rich with higher whole-rock silica, except in the olivine andesite of eastern Juniper Ridge, which has augite phenocrysts that are poor in both iron and calcium compared to augites in the plateau basalts. Likewise, orthopyroxene is systematically more iron-rich as whole-rock silica content increases.

Low-silica rhyolite at eastern Juniper Ridge contains two groups of orthopyroxene: larger, blocky, subhedral crystals are more iron-rich (Fs_{42} to Fs_{45}); smaller, prismatic, euhedral crystals include both iron-poor (Fs_{25} to Fs_{26}) and relatively iron-rich (Fs_{38} to Fs_{40}) compositions (Fig. 3.2a). As noted above (Section 3.2.2), feldspar texture, size and composition in the sample correlate in much the same manner.

Rhyolites at western Juniper Ridge contain orthopyroxene and clinopyroxene, but only the pyroxene pair from the lower-silica rhyolite has the appropriate tie-line orientation for estimating magmatic temperature (Fig 3.2c). Estimated equilibration temperature for the low silica rhyolite is 750 to 800°C but error based on compositional variation within the sample, analytical error and calibration error is probably on the order of 30 to 50°C. At higher pressures, the area of the "forbidden zone" expands, but temperature contours are only slightly displaced (Lindsley, 1983), so that the 1-atmosphere plot is probably applicable despite lack of independent pressure estimates.

Single clinopyroxenes provide an estimate of minimum magmatic temperature. Based on single pyroxene analyses, minimum temperatures for the plateau basalts and andesite at eastern Juniper Ridge range from about 650 to 1100°C, and are clearly too low to represent magmatic temperature except possibly in the andesite (900 to 1100°C).

TABLE 3.3: Representative microprobe analyses of pyroxene

sample #	JR-91-13	JR-91-18	JR-91-34	JR-91-34	JR-92-48	JR-92-48	JR-91-42	JR-92-53
map unit	Tr_1	Tr_2	Tr_3	Tr_3	Tr_4	Tr_4	Toa_3	Tobg
SiO_2	48.06	47.75	49.19	51.10	53.22	53.39	52.35	49.58
TiO_2	0.22	0.09	0.11	0.14	0.14	0.12	0.53	2.48
Al_2O_3	0.52	0.16	0.29	0.63	0.39	1.69	1.92	3.36
FeO	27.72	40.30	34.44	18.56	23.01	16.08	7.63	10.05
Fe_2O_3	1.24	0.77	1.06	0.56	n.d.	1.29	1.17	0.31
MnO	1.16	2.58	1.67	0.98	1.08	0.65	0.24	0.32
MgO	1.05	7.05	11.61	9.04	20.93	25.73	17.33	13.98
CaO	19.38	1.22	1.47	18.79	1.15	1.00	18.27	18.96
Na_2O	0.44	0.03	0.04	0.32	0.03	0.02	0.20	0.41
K_2O	0.01	0.01	0.02	n.d.	0.01	n.d.	n.d.	0.02
Cr_2O_3	n.d.	n.d.	n.d.	0.01	0.01	0.14	0.19	0.17
Total	99.80	99.96	99.90	100.13	99.97	100.11	99.83	99.64
Wo	45	3	3	40	2	2	38	41
En	3	22	35	27	60	72	50	42
Fs	52	75	62	33	38	26	12	17

Fe_2O_3 calculated by charge balance after Papike et al. (1974). Beam conditions: beam current, 50 na; accelerating voltage, 15 kv; beam diameter,1 micron; counting time, 10 sec. for all elements except Ti (20 sec.). Analytical precision based on repeat analysis of pyroxene standard (KAUG, n = 27) is better than 1% for SiO_2, Al_2O_3, MgO and CaO, better than 5% for TiO_2 and Na_2O, and 5 to 15 % for FeO, MnO and Cr_2O_3. Values for other elements are at or below detection limits. Pyroxene compositions: Wo = wollastonite ($Ca_2Si_2O_6$); En = enstatite ($Mg_2Si_2O_6$); Fs = ferrosilite ($Fe_2Si_2O_6$).

TABLE 3.4: Representative and average microprobe analyses of olivine

sample #	JR-91-13		JR-91-11		JR-91-21		JR-91-42	
map unit	Tr_2		Tad_1		Toa_1		Toa_3	
	avg (n=3)	std. dev.	avg (n=4)	std. dev.	avg (n=5)	std. dev.	avg (n=2)	std. dev.
SiO_2	29.10	0.17	38.07	0.41	32.15	0.18	37.90	0.38
MgO	0.68	0.01	40.43	1.02	15.26	1.12	41.44	1.73
FeO_{TOT}	66.21	0.28	20.41	1.33	50.10	1.44	19.71	2.32
Al_2O_3	n.d.		0.08	0.02	0.14	0.22	0.05	0.01
CaO	0.17	0	0.27	0.02	0.23	0.05	0.17	0
MnO	2.87	0.12	0.30	0.01	1.77	0.17	0.33	0.04
NiO	n.d.		0.11	0.02	n.d.		0.13	0.12
Total	99.03		99.67		99.65		99.73	
Fo	2		78		34		79	
Fa	94		22		64		21	
Th	4		0		2		0	

sample #	JR-92-53	JR-92-53		JR-92-59	JR-92-59	JR-92-59	JR-92-59
map unit	Tobg	Tobg		Tob_1	Tob_1	Tob_1	Tob_1
		avg (n=4)	std. dev.				
SiO_2	36.12	38.23	0.62	34.68	35.07	35.99	38.69
MgO	31.53	42.03	2.17	25.82	27.32	31.24	43.57
FeO_{TOT}	30.76	18.52	2.39	37.63	35.85	30.69	15.69
Al_2O_3	0.04	0.07	0.01	0.01	0.05	0.05	0.06
CaO	0.32	0.24	0.04	0.40	0.38	0.38	0.25
MnO	0.47	0.25	0.03	0.65	0.54	0.53	0.25
NiO	0.07	0.19	0.05	0.04	0.10	0.04	0.18
Total	99.31	99.53		99.23	99.31	98.92	98.69
Fo	65	80		55	58	64	83
Fa	35	20		45	42	36	17
Th	0	0		0	0	0	0

FeO_{TOT} = total iron as FeO. Beam conditions: beam current, 50 na; accelerating voltage, 15 kv; beam diameter, 1 micron; counting time, 10 sec. for all elements. Analytical precision based on repeat analysis of standards (FO83, n=10; FAYL, n=3) is better than 1% (1 sigma s.d.) for SiO_2, MgO (Mg-rich olivine), FeO, and MnO (Fe-rich olivine), and 5 to 15 % for MgO (Fe-rich olivine), and MnO (Mg-rich olivine). Values for Al_2O_3, CaO, and NiO are at or below detection limits. Olivine compositions: Fo = forsterite (Mg_2SiO_4); Fa = fayalite (Fe_2SiO_4); Th = tephroite (Mn_2SiO_4).

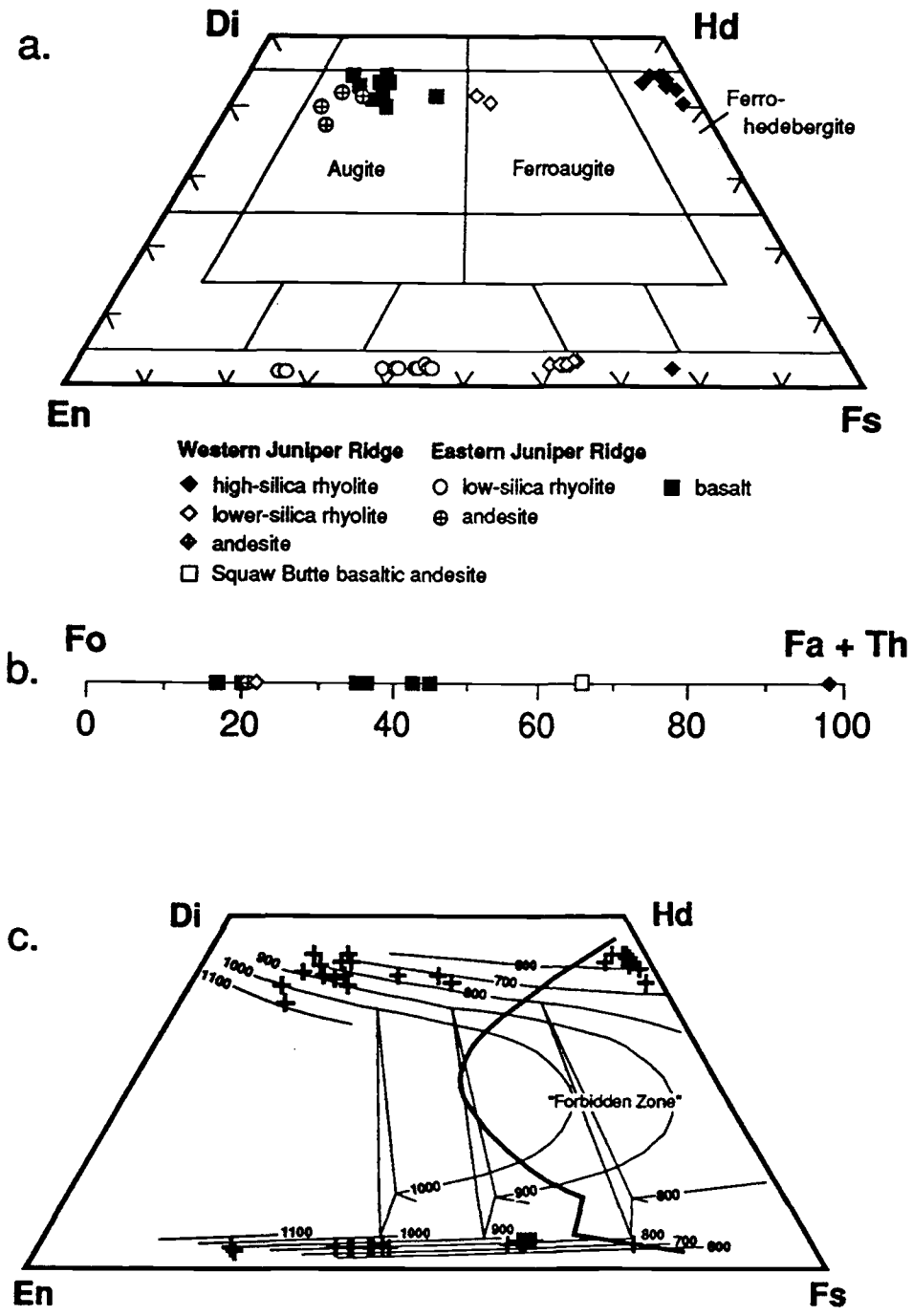

Figure 3.2: Pyroxene and olivine compositions and pyroxene geothermometry. a. Juniper Ridge pyroxenes plotted on the pyroxene quadrilateral. Di = diopside ($CaMgSi_2O_6$); Hd = hedenbergite ($FeMgSi_2O_6$); En = enstatite ($Mg_2Si_2O_6$); Fs = ferrosilite ($Fe_2Si_2O_6$). b. Juniper Ridge olivine compositions. Fo = forsterite (Mg_2SiO_4); Fa = fayalite (Fe_2SiO_4); Th = tephroite (Mn_2SiO_4). c. Recalculated pyroxene compositions plotted on the 1-atmosphere graphical geothermometer of Lindsley (1983). Recalculation displaces values to slightly higher Ca. Heavy line represents limit of the "forbidden zone" at one atmosphere.

3.2.4 Olivine: Olivine populations within Juniper Ridge samples are relatively homogeneous except in the plateau basalts, which exhibit a range of compositions from Fo_{55} to Fo_{83} (Table 3.4 and Fig. 3.2b). Most olivines in the plateau basalts, in the eastern Juniper Ridge andesite, and in the "mixed" andesite at western Juniper Ridge cluster around Fo_{80}. Euhedral olivine from the Squaw Butte basaltic andesite is anomalously iron-rich (Fo_{34}), and is the only olivine besides fayalite (Fa_{94} in high-silica rhyolite) to contain significant amounts of MnO. The presence of fayalite in the high-silica rhyolite at western Juniper Ridge is consistent with pyroxene data which plot in the "forbidden zone" of the pyroxene quadrilateral. Orthopyroxene in the fayalite-bearing rhyolite is probably not an equilibrium phase.

3.2.5 Oxide minerals: Titanomagnetite was present in all samples and ranges in composition from $X_{usp}=0.25$ to $X_{usp}=0.60$ (Table 3.5a). Minor and trace elements show some variation between samples, but within each sample, titanomagnetite compositions are fairly homogeneous. Ferrian ilmenite was found only in three samples (Table 3.5b), and ranges from $X_{ilm}=0.88$ to $X_{ilm}=0.95$ in composition. All oxide grains probed were 10 to 30 microns in diameter and euhedral phenocrysts except for the ilmenite in JR-91-42, which consisted of small (3 to 5 microns), euhedral groundmass crystals.

Of the three samples that contain oxide pairs, the two rhyolites are suitable for oxide geothermometry based on the Mg/Mn partitioning test of Bacon and Hirschmann (1988). Figure 3.3 confirms that ilmenite in JR-91-42 is a groundmass phase out of equilibrium with titanomagnetite. The mineral pair lacks Mg/Mn equilibrium, and yields anomalously low temperature and high log fO_2 (oxygen fugacity) estimates (762°C and -16.3, respectively).

Equilibrium temperature and oxygen fugacity (fO_2) for the rhyolites were estimated with the Ghiorso and Sack (1991a) numerical geothermometer and are 759 ± 30°C in the high-silica rhyolite at western Juniper Ridge and 788 ± 30°C in the low-silica rhyolite at eastern Juniper Ridge (Table 3.5b). Temperature estimates for the rhyolites derived from the Anderson and Lindsley (1988) graphical thermometer (Fig. 3.4) and the Ghiorso and Sack (1991a) numerical

TABLE 3.5a: Microprobe analyses of titanomagnetite

sample #	JR-91-13			JR-91-18			JR-91-34		
map unit	Tr_2			Tr_2			Tr_3		
	avg	(n=3)	std. dev.	avg	(n=6)	std. dev.	avg	(n=6)	std. dev.
SiO_2	0.10		0.01	0.09		0.02	0.11		0.04
TiO_2	15.48		0.03	17.25		0.19	16.11		0.45
Al_2O_3	0.39		0.01	0.42		0.02	1.13		0.03
FeO	44.49		0.05	46.05		0.17	44.47		0.41
Fe_2O_3	38.28		0.11	34.75		0.45	36.45		0.80
MnO	0.77		0.04	0.84		0.06	0.78		0.05
MgO	0.04		0.01	0.04		0.01	0.51		0.01
V_2O_5	0.08		0.01	0.12		0.05	0.23		0.04
Cr_2O_3	n.d.			0.02		0.02	0.01		0.02
ZrO_2	0.04		0.05	n.d.			0.04		0.03
Total	99.67			99.58			99.84		
X_{ulv}	0.45			0.50			0.48		

sample #	JR-92-48			JR-91-21			JR-91-42		
map unit	Tr_4			Toa_1			Toa_3		
	avg	(n=3)	std. dev.	avg	(n=3)	std. dev.	avg	(n=3)	std. dev.
SiO_2	0.07		0.01	0.08		0.03	0.06		0.01
TiO_2	8.34		1.03	20.51		1.05	17.50		0.41
Al_2O_3	1.53		0.07	0.75		0.07	1.91		0.88
FeO	36.72		1.08	48.60		0.87	44.31		0.73
Fe_2O_3	50.98		1.70	28.41		2.08	31.17		2.68
MnO	0.55		0.02	0.95		0.09	0.43		0.02
MgO	0.98		0.02	0.36		0.08	1.67		0.66
V_2O_5	0.66		0.03	0.11		0.01	0.98		0.07
Cr_2O_3	0.05		0	n.d.			1.88		2.91
ZrO_2	0.02		0.04	0.04		0.05	0.03		0.02
Total	99.90			99.81			99.94		
X_{usp}	0.25			0.60			0.57		

TABLE 3.5b: Microprobe analyses of ilmenite

sample #	JR-91-18			JR-92-48			JR-91-42		
map unit	Tr_2			Tr_4			Toa_3		
	avg	(n=6)	std. dev.	avg	(n=3)	std. dev.	avg	(n=3)	std. dev.
SiO_2	0.03		0.02	0.02		0.01	0.08		0.01
TiO_2	48.51		0.45	45.80		0.10	48.18		0.51
Al_2O_3	n.d.			n.d.			n.d.		
FeO	42.18		0.43	36.84		0.35	39.87		0.30
Fe_2O_3	5.86		0.73	13.45		0.21	7.34		1.08
MnO	1.29		0.05	0.82		0.03	0.53		0.05
MgO	0.08		0.01	1.98		0.15	1.64		0.21
V_2O_5	0.25		0.03	0.40		0.06	0.50		0.06
Cr_2O_3	0.02		0.02	0.01		0.01	0.01		0.02
ZrO_2	0.04		0.04	0.06		0.05	0.24		0.17
Nb_2O_5	0.35		0.08	0.09		0.04	0.09		0.08
Total	98.61			99.47			98.48		
X_{ilm}	0.95			0.88			0.94		
T (in C)	759			788					
log f_{O_2}	-16.4			-13.5					

n.d. = not detected. Beam conditions: beam current, 50 na; accellerating voltage, 15 kv; beam diameter, 1 micron; counting time, 10 sec. for all elements. FeO and Fe_2O_3 calculated by the method of Carmichael (1967). For titanomagnetite, analytical precision based on repeat analysis of standard (MAGT, n=10) is better than 1% (1 sigma s.d.) for FeO and Fe_2O_3, better than 10% for V_2O_5, and better than 30% for TiO_2, Cr_2O_3, and MnO. For ilmenite, analytical precision based on repeat analysis of standard (ILMN, n=10) is better than 7% (1 sigma s.d.) for MgO, TiO_2, MnO, FeO, and Nb_2O_5 and better than 15% for V_2O_5 and Fe_2O_3. All other elements are at or near detection limit. End-member compositions calculated by the method of Stormer (1983): X_{usp} = molecular proportion of ulvospinel component (Fe_2TiO_4); X_{ilm} = molecular proportion of ilmenite component ($FeTiO_3$). T and log f_{O_2} estimates were calculated with the program FeTi/GS91, which is based on the formulation of Ghiorso and Sack (1991a).

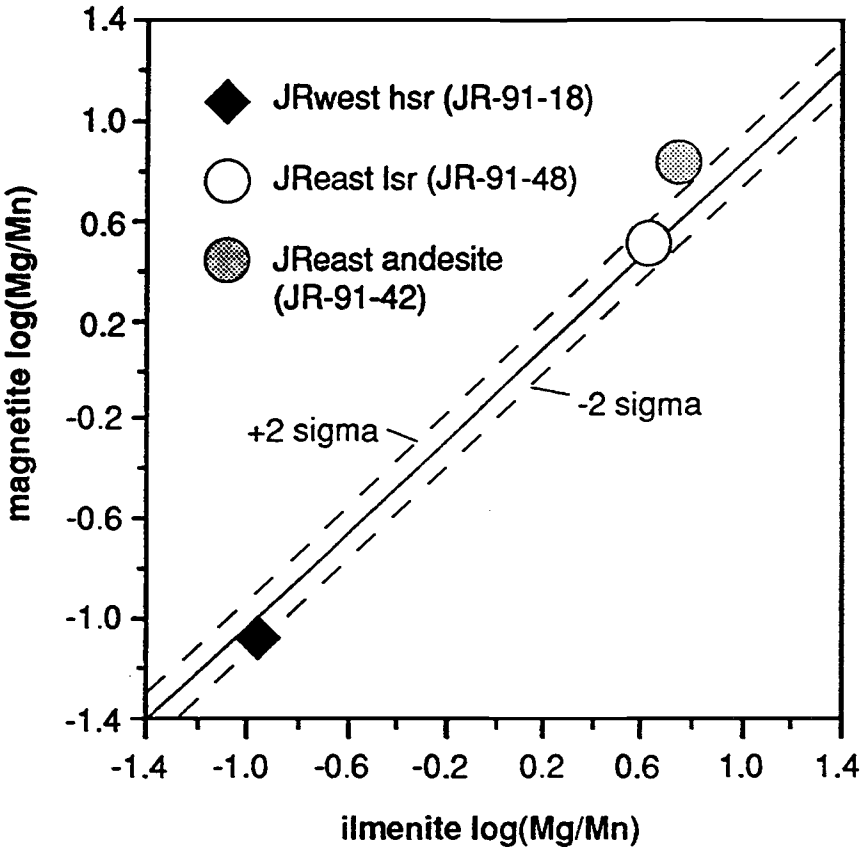

Figure 3.3: Mg/Mn partitioning test for three Juniper Ridge rocks that contain titanomagnetite and ilmenite pairs, after Bacon and Hirschmann (1988). Solid line represents linear regression for 213 ilmenite/magnetite pairs from fresh volcanic rocks. Compositions that fall outside the 2 sigma s.d. envelope are probably not in equilibrium and will produce erroneous temperature estimates. Compositions that plot within 2 sigma s.d. from the regression line can be assumed to be equilibrium pairs, but independent evidence for equilibrium (i.e. homogeneous sample population, euhedral texture, and adjoining grains) is desirable.

geothermometer (Table 3.5b) agree to within about 10°C, but are about 50°C low when estimated by the graphical version of Ghiorso and Sack (1991b), even though the same oxide recalculation method was used for both graphical estimates. Stormer (1983) showed that temperature estimates derived from graphical geothermometers can vary by up to 70°C depending on the recalculation scheme used. Therefore, the numerical temperature estimates of Ghiorso and Sack (1991a) are probably more reliable, because they do not require calculation of oxide end-member compositions.

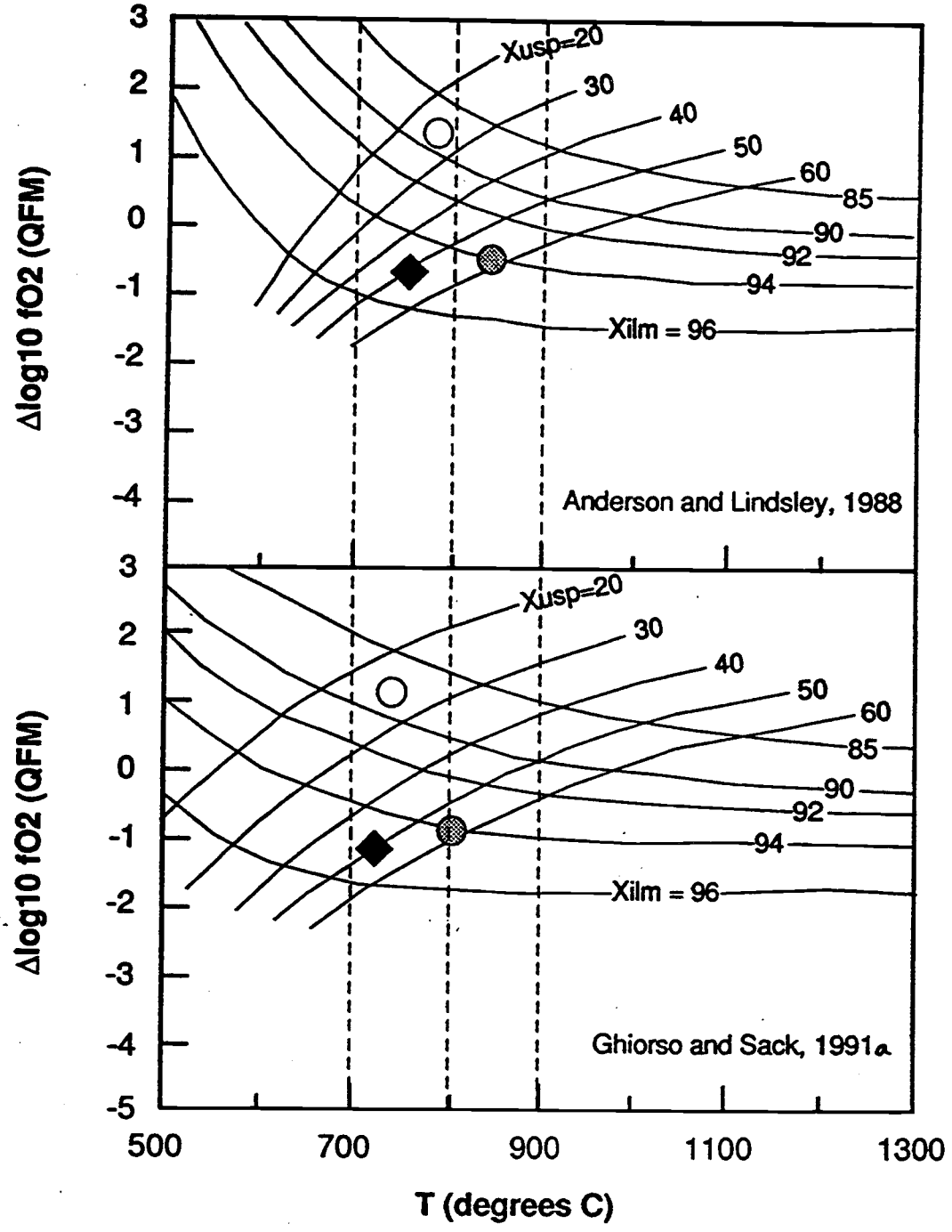

Figure 3.4: Juniper Ridge rocks plotted on the graphical oxide geothermometers of Anderson and Lindsley (1988) and Ghiorso and Sack (1991a), after Ghiorso and Sack (1991b). Symbols as in Figure 3.3. Oxide end-member compositions (X_{ulv} = mole percent ulvospinel component of spinel; X_{ilm} = mole percent ilmenite component of rhombohedral oxide) were calculated by the method of Stormer (1993).

3.2.6 Discussion: Mineral compositions, if they represent equilibrium crystalization, contain information about the conditions under which they crystallized. An explanation for the predominance of single feldspar compositions in both eastern and western Juniper Ridge lower-silica rhyolites is that they were quenched at relatively high temperature, before or shortly after reaching the An-Or cotectic (line C-E in Fig. 3.1). Conversely, the dominance of alkali feldspar and the presence of resorbed cores of plagioclase in high-silica rhyolite (Chapter 2) suggests crystallization at relatively low temperature, at or near the liquidus minimum (point C, Fig. 3.1) in the An-Ab-Or system. Abbott (1978) reports an experimental temperature of 735°C (at 1 kb pressure) for the critical point under water- and silica-saturated conditions, in agreement with the temperature estimated here (759 ± 30°C) for the high-silica rhyolite at western Juniper Ridge.

Temperature estimates for the rhyolites based on two-oxide and two-pyroxene geothermometry agree, and suggest equilibration temperatures of 750 to 800°C, but because none of the samples containing oxide pairs also contained two pyroxenes, direct comparison of the oxide and pyroxene temperature estimates is not possible. Estimated temperatures for Juniper Ridge rhyolites are considerably lower than temperaures estimated for similar rocks by Honjo et al. (1992), who used the Lindsley (1983) geothermometer to estimate magmatic temperatures of 850 to 1000 degrees for rhyolites on the Snake River Plain.

Non-equilibrium mineral compositions are harder to recognize and interpret, but also reveal useful petrologic information. The andesite of western Juniper Ridge, which contains resorbed quartz in addition to large plagioclase megacrysts and olivine-plagioclase glomerocrysts, contains unusually calcic labradorite and bytownite crystals identical to those found in the regional plateau basalts, supporting whole rock chemical data (Section 3.3.3) and field observations (Chapter 2) that suggest the andesite was produced by mixing of rhyolite and basalt shortly before eruption.

Feldspars from eastern Juniper Ridge rhyolite and andesite exhibit oscillatory zonation and include compositions that are more calcic than expected for their bulk composition, all of

which suggest a complex petrologic history. Based on the Ba content of plagiolcase and host rock, the sodic plagioclase in both rocks is most likely to be in equilibrium with the host rock, while the calcic plagioclase probably crystallized earlier in the history of each rock. Experimental and empirical relationships quantified by Blundy and Wood (1991) suggest that partitioning of Ba into plagioclase is dependent mainly on crystal chemistry (anorthite content), thus Ba content in plagioclase can be used to predict the Ba content of coexisting liquid. The anorthite content of sodic plagioclase from eastern Juniper Ridge was used to predict Ba in coexisting liquid. Estimates of 1165 ppm in rhyolite and 968 ppm in andesite closely match observed whole-rock Ba (1189 ppm in rhyolite; 982 ppm in andesite), assuming reasonable estimates of magmatic temperature (750°C for rhyolite; 900°C for andesite). Calcic plagioclase yields Ba contents for coexisting liquid that are lower than observed. If the method is reversed, Ba contents of the sodic plagioclase from both rocks yield reasonable magmatic temperatures (742°C for rhyolite; 878°C for andesite), whereas Ba content of the calcic plagioclase from both rocks yeild estimates of magmatic temperature that are probably too high (1262°C for rhyolite; 982°C for andesite).

By the criteria of Blundy and Wood (1991), Ba content of plagioclase from western Juniper Ridge rocks, including lower-silica rhyolite (Tr_3) and Squaw Butte basaltic andesite (Toa_1), is too low to be in equilibrium with the whole-rock composition, even though the phenocrysts are compositionally homogeneous and euhedral in texture. Predicted Ba content of coexisting liquids is 590 and 880 ppm for andesite and lower-silica rhyolite, respectively, but whole rock Ba in these rocks is 1523 and 1684 ppm, suggesting that the partitioning behavior described in Blundy and Wood (1991) may not apply to extremely high-Ba rocks (Squaw Butte basaltic andesite), or to rocks that contain alkali feldspar (lower-silica rhyolite).

3.3 Whole Rock Chemistry

3.3.1 Methods: Major element and some trace element compositions for Horsehead Mountain (Table 6.2) and Juniper Ridge (Table 3.6) were obtained by X-ray fluorescence (XRF) analysis at Stanford University. Precision of XRF analyses was determined by averaging repeat analyses of standards from all analytical runs performed for this study. XRF analysis for Burns Butte samples (Table 3.7) was done commercially by XRAL Laboratories. Replicate analyses for seven samples showed good agreement between the two labs, except for minor systematic differences in MnO, MgO, and P_2O_5, and non-systematic differences in Na_2O. In order to facilitate comparison of Burns Butte data with the Stanford data set, correction factors were applied to the Burns Butte data for MnO (-0.015 wt. %), MgO (-0.07 wt. % for MgO < 0.2) and P_2O_5 (-0.02 wt. %); for Na_2O, values from instrumental neutron activation analysis (INAA) were used (Na_2O from INAA and Stanford XRF agree to within 0.1 wt. % Na_2O, which is within analytical error for XRF values).

Instrumental neutron activation analysis (INAA) was performed at the Oregon State University Radiation Center using the method outlined by Laul (1979). Precision estimates were supplied by the Radiation Center and were calculated from analyses of standards from multiple reactor runs.

3.3.2 Plateau basalts: The plateau basalts analyzed for this study are classified as "potassium-poor" tholeiitic basalts by the system of Irvine and Baragar (1971). The porphyritic plateau basalt (JR-92-59) is identical in composition to the non-porphyritic basalt (JR-92-53) with the exception of slightly depleted MgO, Sr and Ni, which is due to removal of olivine and accumulation of plagioclase phenocrysts (Chapter 4). The basalts analyzed for this study are slightly more evolved with respect to SiO_2 and MgO than representative high-alumina olivine tholeiites (HAOT) described by Hart et al. (1984) and Draper (1991), but they share many of the same textural, mineralogical and geochemical characteristics, such as a diktytaxitic, subophitic

TABLE 3.6: Whole-rock compositions of Juniper Ridge samples

sample #	JR-91-2	JR-91-4	JR-91-5	JR-91-11	JR-91-12	JR-91-13	JR-91-14
map unit	Tr_2	Tr_1	Tr_3	Tad_1	Toa_1	Tr_2	Tobg
XRF analyses (wt. %)							
SiO_2	77.4	77.3	75.1	61.3	54.4	77.1	48.8
TiO_2	0.07	0.07	0.17	0.96	1.64	0.07	1.64
Al_2O_3	12.13	11.96	13.40	14.67	14.59	12.14	16.72
$Fe_2O_3^*$	1.28	1.36	1.74	7.61	13.63	1.21	11.50
MnO	0.03	0.03	0.05	0.12	0.40	0.03	0.19
MgO	n.d.	n.d.	0.09	3.84	2.12	0.02	7.17
CaO	0.42	0.25	1.02	5.52	5.52	0.83	10.06
Na_2O	4.10	4.39	4.32	3.64	4.66	3.96	3.05
K_2O	4.56	4.60	4.06	2.12	2.09	4.63	0.42
P_2O_5	n.d.	0.00	0.02	0.18	0.95	0.01	0.39
Total	99.45	99.61	99.27	100.41	99.57	99.68	100.31
XRF analyses (ppm)							
V	n.d.	0.5	2.1	155	13	1.5	253
Ni	14	14	6	50	17	13	93
Cu	1.6	1.4	2.9	40	16	3.7	63
Zn	113	141	45	117	205	106	96
Ga	19	22	15	19	28	19	19
Rb	100	102	91	46.6	34	105	3.4
Sr	10	3.1	74	133	256	12.5	325
Ba	733	422	1526	408	1684	332	371
Y	93	110	43	78	130	88	37
Zr	247	318	252	157	873	207	114
Nb	21.8	25.8	10.8	13	56.3	21.8	6.9
Pb	19	19	16	11	13	18	5
INAA analyses (ppm)							
Sc	0.8	0.4	4.8	19.1	41.3	0.8	32.8
Cr	2	3	1	49	5	2	166
Co	n.d.	n.d.	0.8	24.6	7.5	0.2	42.7
Cs	3.0	3.3	2.7	1.4	0.7	3.5	n.d.
As	3.4	4.1	2.4	1.9	n.d.	4.4	n.d.
Sb	0.6	0.8	0.6	0.4	n.d.	0.8	n.d.
Se	n.d.	1.9	0.7	1.2	3.9	1.6	n.d.
La	35.1	33.1	27.5	20.1	62.1	20.2	14.1
Ce	76	81	57	41	138	54	24
Nd	40	45	23	29	70	29	15
Sm	12.1	12.7	6.5	10.0	21.9	10.8	5.6
Eu	0.95	0.92	1.17	1.32	6.0	0.61	1.78
Tb	2.2	2.6	1.05	1.79	3.5	2.1	0.97
Yb	9.3	10.7	4.7	7.8	13.3	9.2	3.2
Lu	1.27	1.45	0.69	1.06	1.88	1.24	0.44
Hf	8.8	11.4	7.0	5.1	17.5	7.9	2.8
Ta	1.3	1.5	0.7	0.7	2.7	1.3	0.3
Th	9.2	9.9	8.2	4.2	3.5	8.8	0.3
U	3.6	4.0	3.3	1.9	1.4	4.1	n.d

Major element data normalized to 100% anhydrous. Totals are pre-normalization. n.d. = not detected. $Fe_2O_3^*$ = total iron as Fe_2O_3. Precision for major elements is better than 1% (1 sigma s.d.) for all elements except MnO, MgO, Na_2O, and P_2O_5 (<5%). For XRF trace elements, one-sigma precision estimates are better than 1% for Zr, Sr, Rb (for Rb>50), Zn, and Cr (for Cr>100), better than 3 % for Nb, Ga, Cu, and Ba (for Ba>500), and better than 10 % for Y, Pb, Ni, V, Cr (for Cr<100), Ba (for Ba<500) and Rb (for Rb<50). INAA precision values are estimated to be better than 5% for Sc, Co, La, Eu, Tb, and Hf, better than 10% for Cr, Sm, Yb, Lu, Ta, and Th, and 10 to 20% for Cs, As, Sb, Se, Ce, Nd, and U.

TABLE 3.6 (continued)

sample #	JR-91-18	JR-91-19	JR-91-20	JR-91-21	JR-91-25	JR-91-27	JR-91-34
map unit	Tr_2	Tad_1	Tr_1	Toa_1	Tr_1	Tad_1	Tr_3
XRF analyses (wt. %)							
SiO_2	77.0	73.6	77.4	53.9	77.3	59.7	75.2
TiO_2	0.08	0.27	0.08	1.72	0.07	1.10	0.14
Al_2O_3	12.13	12.50	11.94	14.66	11.93	14.28	13.06
Fe_2O_3*	1.32	2.74	1.45	13.98	1.39	8.79	1.63
MnO	0.03	0.05	0.03	0.39	0.03	0.15	0.05
MgO	0.00	1.02	0.01	2.13	0.00	4.22	0.15
CaO	0.68	1.85	0.37	5.56	0.28	5.69	1.30
Na_2O	4.13	4.05	3.99	4.62	4.24	3.51	3.99
K_2O	4.68	3.91	4.76	2.07	4.76	2.36	4.49
P_2O_5	0.00	0.05	0.00	0.99	0.00	0.22	0.01
Total	99.85	99.66	99.44	99.61	99.66	99.76	99.80
XRF analyses (ppm)							
V	3.5	34	1.0	6.8	1.7	172	1.1
Ni	12	21	15	14	15	56	8
Cu	2.0	9.0	2.2	14.9	4.5	56	4.0
Zn	109	111	134	211	139	124	46
Ga	19	20	21	27	22	21	16
Rb	97	90	97	34.1	104	37.4	92
Sr	15.5	42	6.8	255	4.5	146	52
Ba	709	480	364	1552	408	645	1539
Y	91	88	106	130	111	74	53
Zr	256	242	306	834	318	300	224
Nb	21.5	20.3	24.8	54.9	25.6	13.8	13.9
Pb	18	18	19	12	20	11	16
INAA analyses (ppm)							
Sc	0.8	4.7	0.6	42.7	0.5	20.9	4.9
Cr	2	14	3	3	3	47	1
Co	n.d.	5.8	0.3	8.1	0.3	30.4	0.5
Cs	3.1	3.0	3.1	0.7	3.2	1.2	3.2
As	4.1	3.7	4.2	n.d.	4.3	1.8	3.3
Sb	0.8	0.7	0.8	n.d.	0.9	0.4	0.7
Se	1.5	1.3	1.5	3.8	1.8	n.d.	0.9
La	33.1	28.3	33.4	59.4	33.9	32.0	31.9
Ce	76	n.d.	77	141	81	68	62
Nd	36	n.d.	36	74	40	33	29
Sm	12.4	9.9	13.7	22.7	14.0	11.0	8.5
Eu	0.87	0.88	0.91	6.15	0.91	1.82	1.12
Tb	2.1	2.1	2.5	3.5	2.6	1.9	1.4
Yb	9.2	9.3	11.1	13.6	11.4	7.4	6.0
Lu	1.23	1.22	1.46	1.89	1.51	1.02	0.84
Hf	8.7	8.6	10.7	17.2	10.9	8.1	7.1
Ta	1.3	1.3	1.4	2.8	1.5	0.7	0.9
Th	8.3	7.7	8.5	3.3	8.9	3.8	8.8
U	3.6	3.4	3.9	1.8	4.0	1.4	3.7

TABLE 3.6 (continued)

sample #	JR-91-35	JR-91-42	JR-91-44	JR-91-46	HP-91-13	JR-92-47
map unit	Tr_3	Toa_3	Tad_2	Toa_2	Tr_2	Tob_2
XRF analyses (wt. %)						
SiO_2	75.3	57.7	67.5	61.4	77.5	50.8
TiO_2	0.14	1.26	0.61	0.92	0.09	1.58
Al_2O_3	12.91	16.22	14.26	15.90	12.15	16.47
$Fe_2O_3^*$	1.63	8.12	4.97	6.50	1.23	10.91
MnO	0.04	0.16	0.11	0.13	0.03	0.20
MgO	0.20	3.66	1.47	3.02	0.02	6.33
CaO	1.24	6.45	2.67	4.94	0.36	8.71
Na_2O	3.86	3.85	4.59	4.11	4.04	3.37
K_2O	4.60	2.11	3.70	2.75	4.55	1.05
P_2O_5	0.02	0.45	0.13	0.30	0.01	0.53
Total	99.34	100.14	99.50	100.18	99.59	99.51
XRF analyses (ppm)						
V	4.8	159	74	112	0.5	211
Ni	7	25	26	22	11	74
Cu	5.1	41	27	22	0.4	63
Zn	48	91	87	82	112	96
Ga	15	18	19	18	20	19
Rb	95	30.2	78	45.3	99	15.4
Sr	55	334	110	273	8.6	371
Ba	1523	982	1363	1111	747	657
Y	55	33	59	33	94	33
Zr	228	248	411	318	245	149
Nb	13.6	12.2	21.8	13.8	22.0	9.2
Pb	14	≤	15	10	17	3
INAA analyses (ppm)						
Sc	4.8	21.1	14.4	16.8		27.8
Cr	n.d.	50	39	52		111
Co	0.5	20.0	10.9	16.3		36.6
Cs	3.4	0.8	2.6	1.5		0.9
As	4.2	n.d.	n.d.	n.d.		n.d.
Sb	0.8	n.d.	0.5	0.3		0.2
Se	n.d.	n.d.	1.4	1.0		n.d.
La	30.3	22.4	30.7	24.1		14.7
Ce	72	43	63	49		38
Nd	34	21	29	21		25
Sm	7.7	6.5	8.9	6.2		5.2
Eu	1.06	1.75	1.40	1.59		1.80
Tb	1.3	0.9	1.4	0.9		0.9
Yb	5.7	3.3	5.9	3.6		3.2
Lu	0.84	0.48	0.88	0.51		0.42
Hf	6.8	5.4	10.0	7.3		3.5
Ta	0.9	0.6	1.3	0.7		0.5
Th	8.6	2.1	6.7	3.4		1.4
U	3.8	1.3	3.8	1.3		n.d.

TABLE 3.6 (continued)

sample #	JR-92-48	JR-92-50	JR-92-51	JR-92-53	JR-92-54	JR-92-56
map unit	Tr_4	Tad_2	Tr_4	Tobg	Tr_4	Tr_5
XRF analyses (wt. %)						
SiO_2	72.6	63.2	72.3	47.6	72.6	73.7
TiO_2	0.28	0.95	0.31	1.56	0.32	0.21
Al_2O_3	14.27	15.00	14.33	16.37	14.30	13.37
$Fe_2O_3^*$	2.19	6.21	2.17	11.81	2.14	2.40
MnO	0.05	0.12	0.05	0.19	0.04	0.09
MgO	0.63	2.66	0.35	9.13	0.56	0.08
CaO	2.18	4.37	1.17	9.80	1.75	0.51
Na_2O	3.61	3.98	4.23	2.88	3.74	4.95
K_2O	4.13	3.19	5.07	0.32	4.47	4.62
P_2O_5	0.07	0.30	0.05	0.32	0.07	0.02
Total	99.79	99.83	99.50	99.59	99.65	99.72
XRF analyses (ppm)						
V	16	118	11	243	18	n.d.
Ni	7	30	6	175	6	9
Cu	8.2	39	6.5	71	8.3	5.5
Zn	32	78	44	97	36	86
Ga	13	18	17	18	14	18
Rb	107	70	107	2.7	114	109
Sr	157	221	64	277	122	8
Ba	1189	873	1083	270	1224	1175
Y	24	40	42	28	26	61
Zr	196	262	349	107	251	513
Nb	10.1	16.7	18.9	5.3	12.2	27.3
Pb	14	12	15	2	12	15
INAA analyses (ppm)						
Sc	5.0	15.6	4.3	32.0	4.8	6.9
Cr	5	40	n.d.	279	4	n.d.
Co	3.3	16.6	2.0	52.2	2.9	0.4
Cs	4.8	2.6	4.8	n.d.	5.5	4.9
As	2.4	2.2	2.5	1.9	3.1	3.1
Sb	0.7	0.4	0.8	n.d.	0.8	0.7
Se						
La	22.4	24.7	27.3	8.0	22.5	36.2
Ce	44	52	61	19	47	80
Nd	19	29	28	14	20	37
Sm	3.5	6.0	5.3	4.0	3.7	8.0
Eu	0.69	1.28	0.80	1.56	0.71	1.13
Tb	0.6	1.0	0.9	0.8	0.6	1.5
Yb	2.7	4.3	4.4	2.6	3.0	6.8
Lu	0.44	0.61	0.68	0.38	0.49	0.99
Hf	5.7	6.6	9.3	2.8	6.5	12.4
Ta	0.8	1.0	1.2	0.2	0.9	1.6
Th	10.1	5.9	9.0	0.4	10.9	9.4
U	4.5	2.5	3.6	n.d.	4.7	4.2

TABLE 3.6 (continued)

sample #	JR-92-59	JR-92-62	JR-92-63	JR-92-65	JR-92-71	JR-92-72
map unit	Tob_1	Tr_3	Tad_3	Tr_6	Tad_1	Tr_3
XRF analyses (wt. %)						
SiO_2	47.7	75.1	64.7	76.6	63.1	75.0
TiO_2	1.61	0.17	0.94	0.15	0.87	0.17
Al_2O_3	16.95	13.34	15.07	12.99	14.02	13.52
$Fe_2O_3^*$	11.83	1.75	6.37	1.11	6.92	1.73
MnO	0.20	0.05	0.14	0.03	0.11	0.05
MgO	7.04	0.15	1.49	0.13	3.61	0.14
CaO	11.16	1.03	3.76	0.86	5.03	1.03
Na_2O	2.90	4.48	4.69	3.68	3.74	4.38
K_2O	0.34	3.90	2.56	4.42	2.43	3.92
P_2O_5	0.32	0.02	0.25	0.02	0.17	0.02
Total	100.24	99.37	99.88	99.34	100.01	99.70
XRF analyses (ppm)						
V	278	3.0	74	7.6	139	n.d.
Ni	102	8	7	5	46	7
Cu	92	3.8	12.5	4.0	36	4.4
Zn	93	45	93	24	116	46
Ga	19	15	18	13	19	15
Rb	1.5	90	52	122	56	90
Sr	223	74	210	59	120	74
Ba	431	1558	1192	1400	335	1546
Y	32	44	47	25	62	43
Zr	131	251	310	146	161	253
Nb	6.6	10.5	14.9	7.3	13.5	10.6
Pb	4	16	10	14	11	15
INAA analyses (ppm)						
Sc	40.4	4.8	15.7	2.3	17.7	4.9
Cr	273	n.d.	3	n.d.	49	n.d.
Co	43.7	0.7	9.8	0.8	23.1	0.7
Cs	n.d.	2.6	1.6	3.7	1.6	2.7
As	n.d.	2.0	n.d.	2.5	n.d.	2.5
Sb	n.d.	0.6	0.3	0.6	0.5	0.6
Se	n.d.	n.d.	n.d.	n.d.	n.d.	n.d.
La	10.3	27.2	26.0	21.7	16.2	27.8
Ce	22	63	57	41	40	54
Nd	16	28	31	15	24	24
Sm	4.3	5.6	6.8	3.8	8.6	7.0
Eu	1.78	1.16	2.07	0.57	1.15	1.17
Tb	0.9	0.9	1.1	n.d.	1.5	1.0
Yb	3.0	4.8	4.9	3.1	6.4	4.9
Lu	0.41	0.69	0.69	0.49	0.94	0.73
Hf	2.9	7.0	7.4	4.8	5.6	7.1
Ta	0.3	0.7	0.7	0.7	0.8	0.7
Th	n.d.	8.2	4.8	11.3	5.0	8.4
U	n.d.	3.4	2.3	5.2	2.9	3.7

groundmass of olivine, plagioclase and augitic clinopyroxene, flat to slightly LREE-enriched rare-earth element patterns, low incompatible element concentrations, and relatively high MgO/FeO (0.69 to 0.71). By the criteria of Hart et al. (1984), who documented a continuous compositional spectrum between the high-alumina olivine tholeiites of the Oregon High Lava Plains (HAOT) and the olivine tholeiites of the Snake River Plain (SROT), plateau basalts in vicinity of Juniper Ridge are classified as low-K, low-Ti, transitional tholeiites, and are intermediate in character between the compositional end-members, but closer in composition to HAOT. Chondrite-normalized REE patterns of plateau basalts around Juniper Ridge (Fig. 3.8b) lie within the REE-enriched part of the field of HAOT analyses compiled by Draper (1991).

3.3.3 Western Juniper Ridge: Rocks from western Juniper Ridge range from basaltic andesite to high-silica rhyolite (Fig. 3.5). All are metaluminous and subalkaline, with the exception of several slightly peralkaline lower-silica rhyolites (JR-91-5, 62, 72) and the Squaw Butte basaltic andesite, which is an alkaline, sodic andesite by the classification of Irvine and Baragar (1971). Several glassy rhyolites are slightly peraluminous, but may have undergone minor loss of alkalies due to hydration or weathering.

Samples from western Juniper Ridge form a discontinuous, linear trend in which most intermediate compositions fall on straight lines between the plateau basalts and aphyric high-silica rhyolite (Figs. 3.6, 3.7). Rhyolites fall into three chemical groups that correlate with the map units Tr_1, Tr_2 and Tr_3. Aphyric and phyric high-silica rhyolites (Tr_1 and Tr_2, respectively) show a large degree of compositional overlap, but the aphyric group generally has higher concentrations of transition metals (Cr, Co, Ni, Cu and Zn), high field strength elements (HFSE: Zr, Y, Hf, Ta and Nb), and heavy rare earth elements (HREE: Tb, Yb and Lu), and lower abundances of Ba, Sr and Sc (Fig 3.7). In many respects, phyric high-silica rhyolite is transitional in character between aphyric high-silica rhyolite and lower-silica rhyolite (including both aphyric and phyric varieties of map unit Tr_3), which contains lower elemental abundances

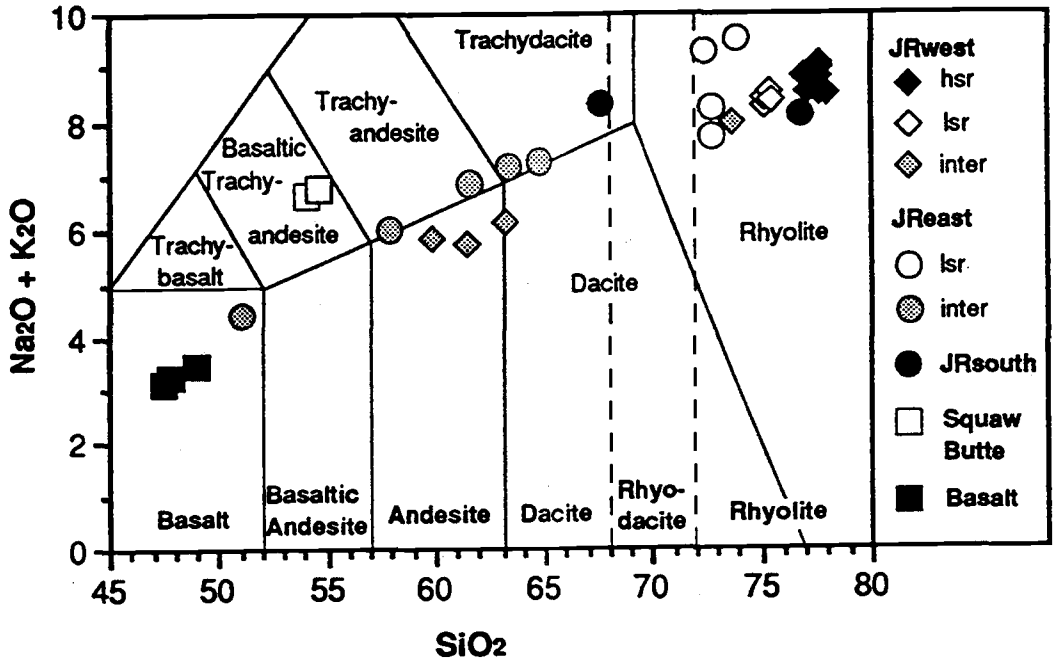

Figure 3.5: $Na_2O + K_2O$ vs. SiO_2 for Juniper Ridge rocks, with the I.U.G.S. classification scheme of LeBas et al. (1986) shown for reference. Nomenclature for Juniper Ridge rocks is shown in bold print: trachy- prefixes are not utilized; "rhyodacite" refers to all rocks between 68 and 72 wt. % SiO_2; "rhyolite" refers to all rocks between 72 and 75.5 wt. % SiO_2; "high-silica" rhyolite refers to rocks with over 75.5 wt. % SiO_2.

than high-silica rhyolites in almost all incompatible trace elements, including transition metals, REE, and HFSE, and higher abundances of Sr, Ba, and Sc (Fig. 3.7).

Squaw Butte basaltic andesite (Toa_1) is chemically unusual because of its extreme enrichments in selected incompatible trace elements: REE (including Eu), HFSE, Ba, Sc, Zn and Ga (Figs. 3.7, 3.8). LREE and HFSE abundances are more than twice that in the high-silica rhyolites. In contrast, Sr, Sb, Cs, Rb, U, Pb and Th abundances are similar to other basaltic andesites in the area (i.e. Toa_2). V, Ni, Cu and Co are depleted with respect to Toa_2, which is regarded as a "normal" basaltic andesite.

On chondrite-normalized rare-earth element diagrams, rhyolites at western Juniper Ridge display systematic increases in overall REE abundance from aphyric LSR to phyric LSR to phyric

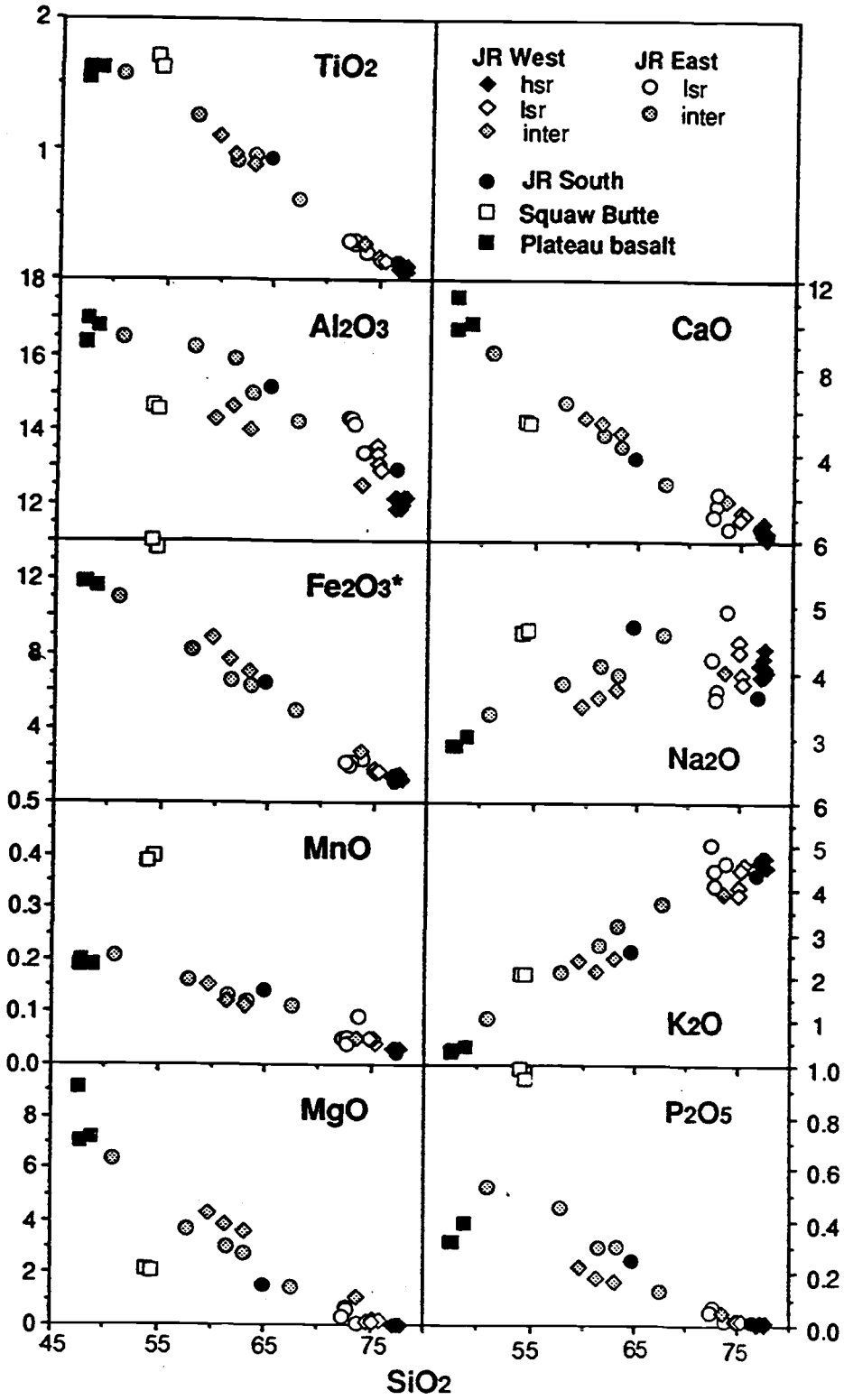

Figure 3.6: Harker variation diagrams for Juniper Ridge rocks. $Fe_2O_3^*$ = total iron as Fe_2O_3. All values in wt. %.

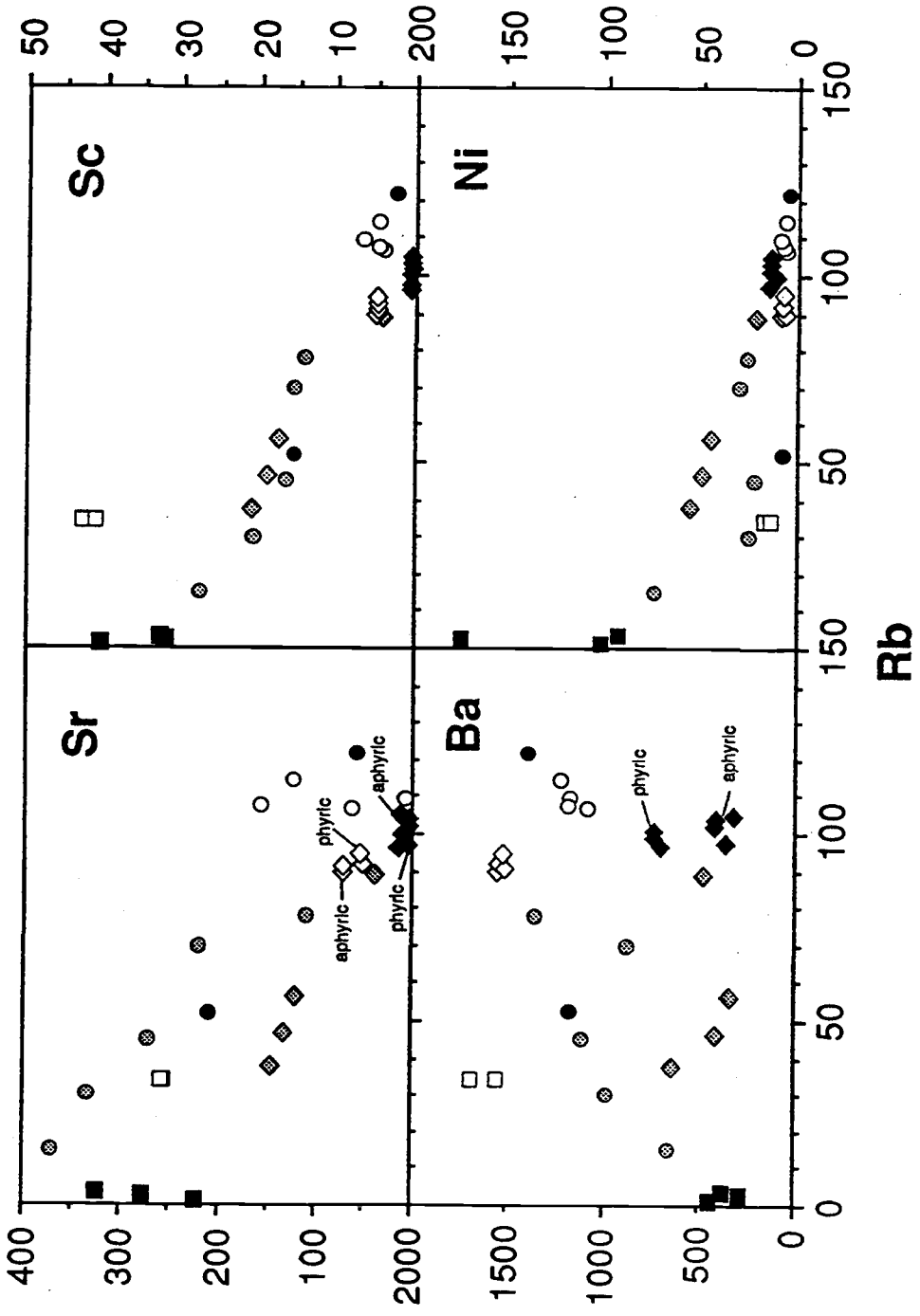

Figure 3.7a: Variation of selected "compatible" trace elements versus Rb. Symbols as in Figure 3.6. All values in ppm.

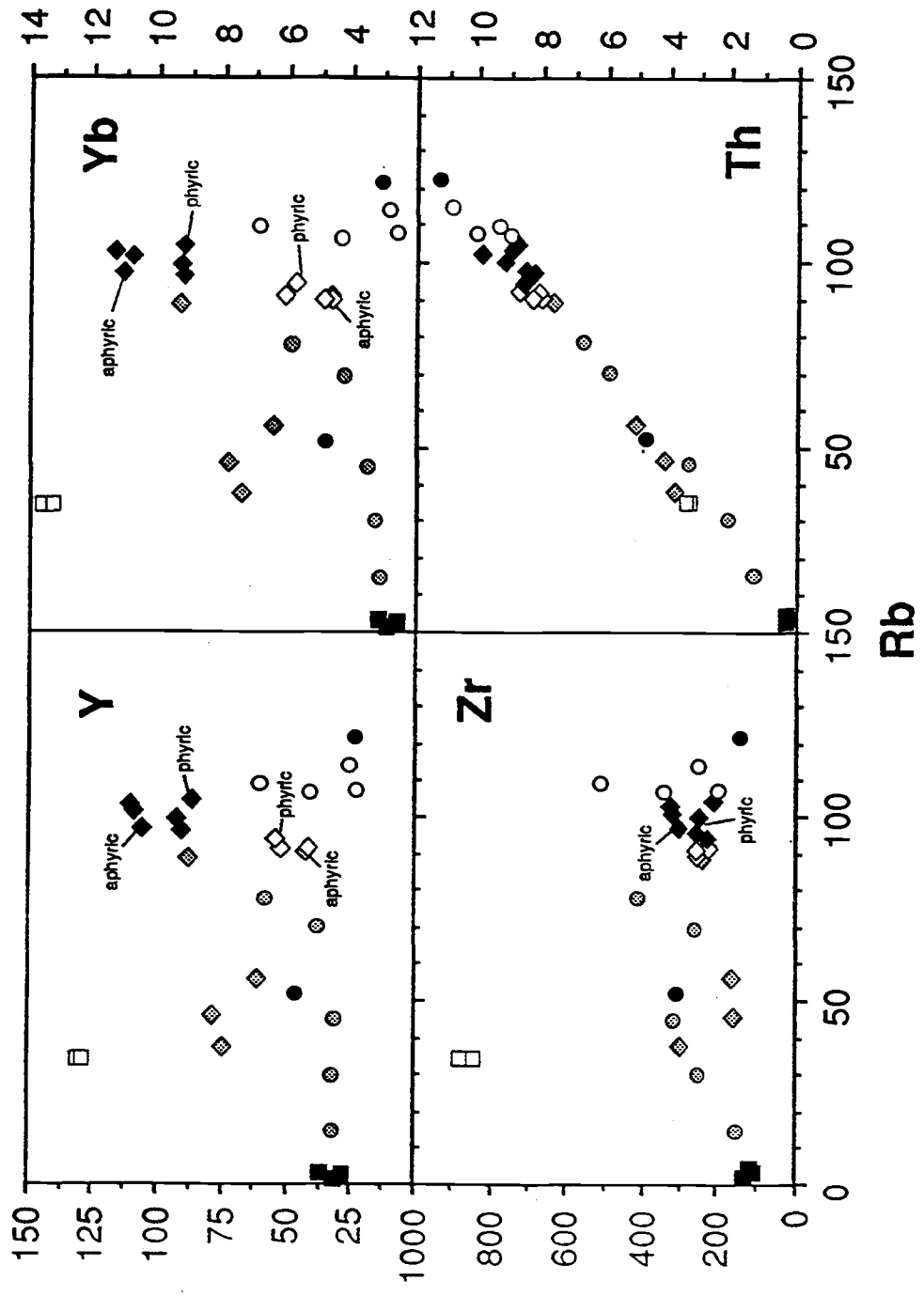

Figure 3.7b: Variation of selected "incompatible" trace elements versus Rb. Symbols as in Figure 3.6. All values in ppm.

HSR to aphyric HSR (Fig. 3.8a), accompanied by a progressively larger Eu anomaly. With evolution, HREE are enriched preferentially with respect to LREE, leading to a flattening of the REE pattern; one phyric HSR (JR-91-13, not shown), with the largest Eu anomaly, is depleted in LREE with respect to the rest of the rhyolites. Intermediate rocks at western Juniper Ridge have REE patterns that overlap LSR, but lie consistently between high-silica rhyolite and plateau basalt patterns (Fig. 3.8b).

3.3.4 Eastern Juniper Ridge: Rocks at eastern Juniper Ridge encompass a wider range of intermediate compositions than at western Juniper Ridge, despite lower overall volume of lavas. Compositions are all metaluminous (the slightly peraluminous composition of one rhyolite vitrophyre may be due to alkali loss during weathering or hydration) and range from andesitic basalt to low-silica rhyolite (Fig. 3.5). Mafic and intermediate compositions at eastern Juniper Ridge constitute a curvilinear trend with the mafic endpoint at HAOT (Figs. 3.6, 3.7). The trend is characterized by decreasing major element abundances (except for Na_2O and K_2O), increasing abundances of alkalies (Ba, Rb and Cs), arsenides (As, Sb and Se), HFSE, REE (except Eu), U, Th, and Pb, and decreasing abundance of Sr, Sc, Co, Cu, Ni, V and Eu. Despite alkali element (including Rb and Cs) abundances that are equal to or greater than those in the high-silica rhyolites at western Juniper Ridge, rhyolites at eastern Juniper Ridge display trace element abundances that for the most part overlap those of the lower-silica rhyolites at western Juniper Ridge (Fig. 3.7). At relatively constant Rb, rhyolite compositions at eastern Juniper Ridge become more evolved with decreasing phenocryst content.

Rhyolite REE patterns at eastern Juniper Ridge overlap those of the mafic and intermediate rocks, and display a concave-upward pattern in the least evolved rhyolite and flattening of the pattern with increasing REE abundance (Fig. 3.9a). Throughout the mafic end of the eastern Juniper Ridge suite, chondrite-normalized REE patterns increase smoothly with SiO_2 content, along with an increasingly negative Eu anomaly (Fig. 3.9b).

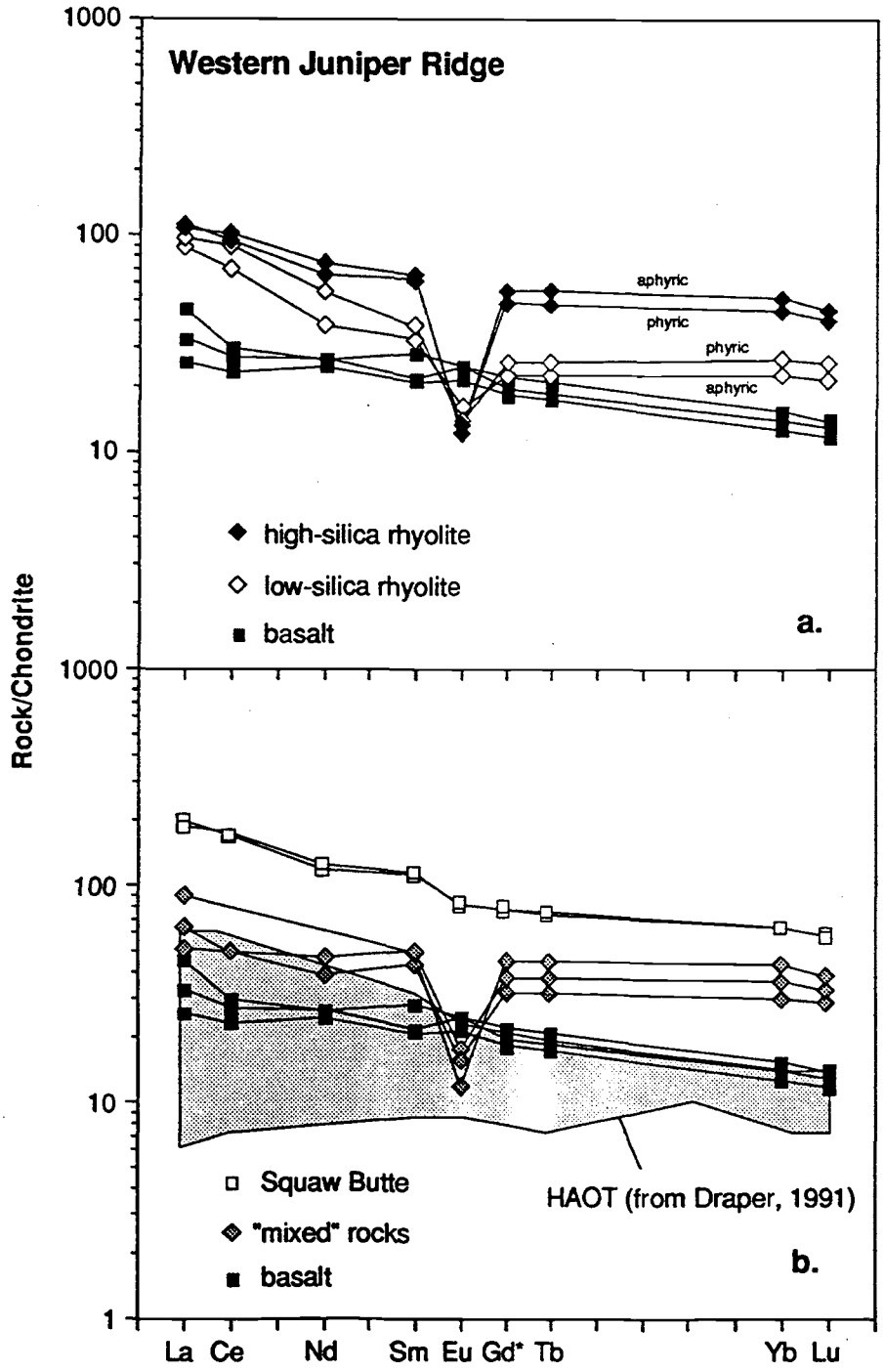

Figure 3.8: Chondrite-normalized rare-earth element diagrams for selected western Juniper Ridge rocks. a. Rhyolitic rocks. b. Mafic and intermediate rocks ("mixed" refers to intermediate and silicic rocks at western Juniper Ridge that fall on mixing lines between high-silica rhyolite and plateau basalt). Plateau basalts shown for reference. Values for non-volatile C1 chondrite from Anders and Ebihara (1982). Gd^* is extrapolated from the heavy rare-earth trend.

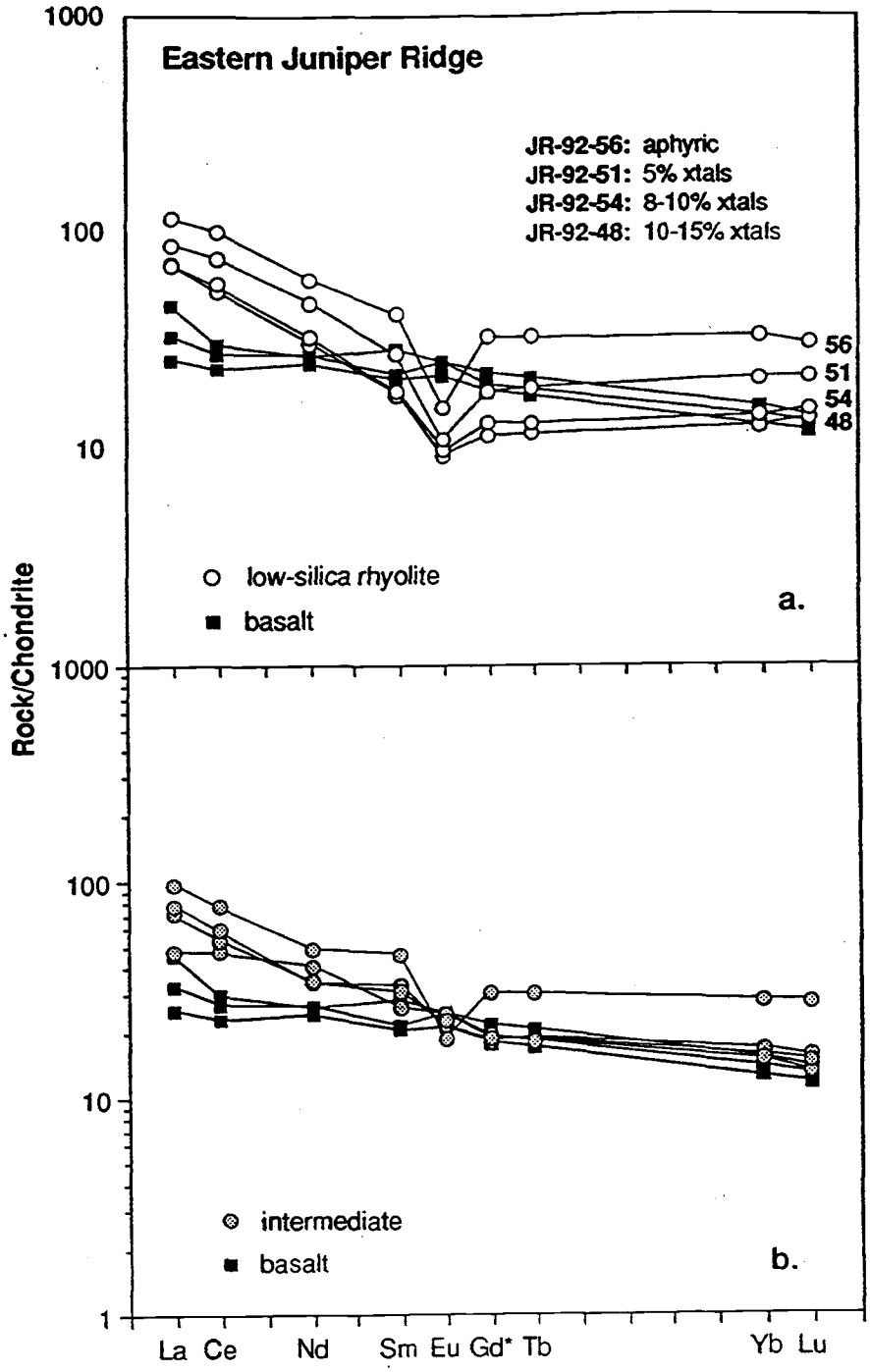

Figure 3.9: Chondrite-normalized rare-earth element diagrams for selected eastern Juniper Ridge rocks. a. Rhyolitic rocks. b. Intermediate rocks. Plateau basalts shown for reference. Values for non-volatile C1 chondrite from Anders and Ebihara (1982). Gd^* is extrapolated from the heavy rare-earth trend.

3.3.5 Southern Juniper Ridge: Two samples from the southern part of Juniper Ridge were analyzed in this study, including an aphyric high-silica rhyolite and a vitrophyric dacite (Fig. 3.5). They are broadly similar in major element composition to rocks at western and eastern Juniper Ridge (Fig. 3.6), but do not seem to be a part of the compositional trends as defined by trace element variations (Fig. 3.7).

3.3.6 Burns Butte: Samples from Burns Butte were collected and analyzed for use in examining regional chemical variations along the age progressive trend (Table 3.7), but a detailed treatment of within-suite chemical variation and petrogenesis is not attempted here.

Whole rock compositions for Burns Butte samples range from basaltic andesite to high-silica rhyolite (Fig 3.10). All compositions are metaluminous except the high-silica rhyolites, which have over 2 percent normative acmite and are slightly peralkaline.

3.3.7 Discussion: Rocks at Juniper Ridge can be divided into several groups based on their behavior on variation diagrams and rare-earth element plots (Figs. 3.5 to 3.9). These observations form the basis for petrologic modelling presented in the next chapter:

1. The plateau basalts surrounding the Juniper Ridge complex are representative of the regional HAOT basalts and constitute the mafic end member for the western Juniper Ridge mixing trend and the mafic through intermediate trend at eastern Juniper Ridge.

2. Intermediate rocks at western Juniper Ridge plot along straight lines between high-silica rhyolite and plateau basalt, and as discussed in Chapter 4, are probably mixtures or hybrids of the two end-members.

3. In contrast to intermediate rocks at western Juniper Ridge, eastern Juniper Ridge intermediates display curvilinear trace element trends whose silicic ends point away from the least-evolved rhyolites and REE patterns that overlap those of the rhyolites.

TABLE 3.7: Whole-rock compositions of Burns Butte samples

sample #	HP-91-1	HP-91-2	BB-92-1	BB-92-6	BB-92-9	BB-92-10	BB-92-11
map unit	Taw	Tmrb	Tmrb	Tmrb	Tmrg	Taw	Tmar
XRF analyses (wt. %)							
SiO_2	59.0	74.3	74.2	74.2	70.4	56.1	56.5
TiO_2	0.96	0.22	0.22	0.23	0.53	1.08	1.30
Al_2O_3	16.74	13.50	13.31	13.27	14.45	16.66	16.33
$Fe_2O_3^*$	7.35	1.68	1.76	1.69	2.88	8.39	8.74
MnO	0.13	0.04	0.04	0.04	0.06	0.14	0.14
MgO	3.05	0.16	0.12	0.12	0.65	4.07	3.77
CaO	6.06	0.68	0.60	0.60	1.65	7.26	7.02
Na_2O (INAA)	3.98	4.31	4.44	4.38	4.18	3.84	3.77
K_2O	2.28	5.05	5.03	5.12	4.78	2.03	1.84
P_2O_5	0.48	0.04	0.02	0.02	0.12	0.51	0.48
Total	99.53	99.34	99.18	99.47	97.55	99.61	99.8
XRF analyses (ppm)							
V	156	2.7					
Ni	19	7					
Cu	43	5					
Zn	83	40					
Ga	17	16					
Rb	36	115	114	127	88	35	22
Sr	431	27	14	17	132	513	441
Ba	1006	670	650	662	1300	815	788
Y	24	41	51	31	17	13	30
Zr	204	293	243	243	327	169	178
Nb	14.8	32.8	51	44	35	28	17
Pb	11	17					
INAA analyses (ppm)							
Sc	17.2	3.8	3.7	3.7	5.8	20.4	22.2
Cr	14	8	2	2	3	53	48
Co	20.0	1.1	0.9	0.9	3.1	23.4	23.2
Cs	0.7	3.3	3.4	3.5	3.1	0.6	0.6
As	n.d.	4.0	4.0	3.4	2.5	n.d.	n.d.
Sb	n.d.	1.0	1.0	0.9	0.7	n.d.	0.1
Se			2.4	2.7	1.7	1.0	n.d.
La	27.3	40.8	39.7	40.2	27.5	24.9	22.0
Ce	56	81	86	88	56	50	52
Nd	24	34	34	33	22	23	25
Sm	5.1	6.3	6.2	6.3	4.7	5.0	5.4
Eu	1.51	0.44	0.37	0.38	0.91	1.52	1.72
Tb	0.72	1.00	0.95	1.03	0.68	0.68	0.85
Yb	2.3	4.5	4.8	4.7	3.6	2.4	2.8
Lu	0.32	0.70	0.69	0.73	0.58	0.30	0.39
Hf	4.7	8.0	7.6	7.8	7.8	3.9	4.3
Ta	0.7	1.9	2.0	2.0	1.3	0.6	0.7
Th	3.0	10.1	10.8	11.0	8.6	2.1	2.4
U	1.6	5.2	4.4	4.1	3.4	0.9	1.0

HP samples Analytical information and precision as in Table 3.6. **BB samples** Anhydrous major element data corrected as described in text. Totals are pre-normalization and pre-correction. Na_2O values are from INAA. Precision estimates for XRF based on duplicate analyses are better than 1% (1 sigma s.d.) for SiO_2, Al_2O_3, CaO, Na_2O and MnO, better than 5% for TiO_2, Fe_2O_3, K_2O, Rb, Sr, Zr, and Ba, and better than 15% for P_2O_5, Y and Nb.

TABLE 3.7 (continued)

sample #	BB-92-17	BB-92-18	BB-92-22	BB-92-25	BB-92-28	BB-92-29
map unit	Tmar	Tmrb	Tmrb	Tmrb	Tmrg	Tmrg
XRF analyses (wt. %)						
SiO_2	59.5	76.5	76.8	76.8	70.3	67.0
TiO_2	1.00	0.15	0.13	0.17	0.48	0.73
Al_2O_3	16.44	11.01	11.51	10.77	14.60	15.07
$Fe_2O_3^*$	7.62	2.21	1.78	2.57	2.69	4.29
MnO	0.14	0.06	0.04	0.05	0.06	0.09
MgO	2.42	n.d.	n.d.	n.d.	0.64	1.62
CaO	5.99	0.12	0.19	0.12	1.63	3.11
Na_2O (INAA)	3.96	4.86	4.57	4.76	3.98	3.79
K_2O	2.32	4.42	4.46	4.25	5.14	4.17
P_2O_5	0.47	n.d.	n.d.	n.d.	0.10	0.24
Total	99.12	99.95	99.90	100.26	97.29	98.23
XRF analyses (ppm)						
Rb	37	113	107	121	99	73
Sr	453	<10	<10	<10	132	217
Ba	1020	<10	16	62	1250	1120
Y	20	116	92	110	25	28
Zr	192	563	465	685	304	277
Nb	26	60	49	57	22	37
INAA analyses (ppm)						
Sc	16.3	0.6	1.1	0.3	5.5	10.1
Cr	14	2	2	2	3	16
Co	20.9	0.05	0.1	0.1	3.2	8.6
Cs	0.4	3.0	3.0	5.0	3.2	2.6
As	n.d.	3.7	4.6	11.4	2.9	2.1
Sb	0.2	0.8	0.9	2.0	0.7	0.5
Se	0.6	n.d.	n.d.	3.7	1.7	1.7
La	28.0	63.1	54.8	68.2	26.1	25.4
Ce	54	136	123	153	54	56
Nd	25	55	47	69	20	24
Sm	5.2	12.0	8.6	14.2	4.4	4.7
Eu	1.46	0.26	0.11	0.89	0.87	1.14
Tb	0.76	2.10	1.76	2.40	0.70	0.76
Yb	2.5	8.8	7.8	9.8	3.5	3.1
Lu	0.35	1.26	1.10	1.35	0.52	0.46
Hf	4.4	14.6	12.6	16.2	7.7	6.7
Ta	0.7	2.9	2.8	2.8	1.3	1.1
Th	3.0	9.8	9.9	9.1	8.8	7.1
U	1.1	3.8	3.6	4.0	3.3	2.7

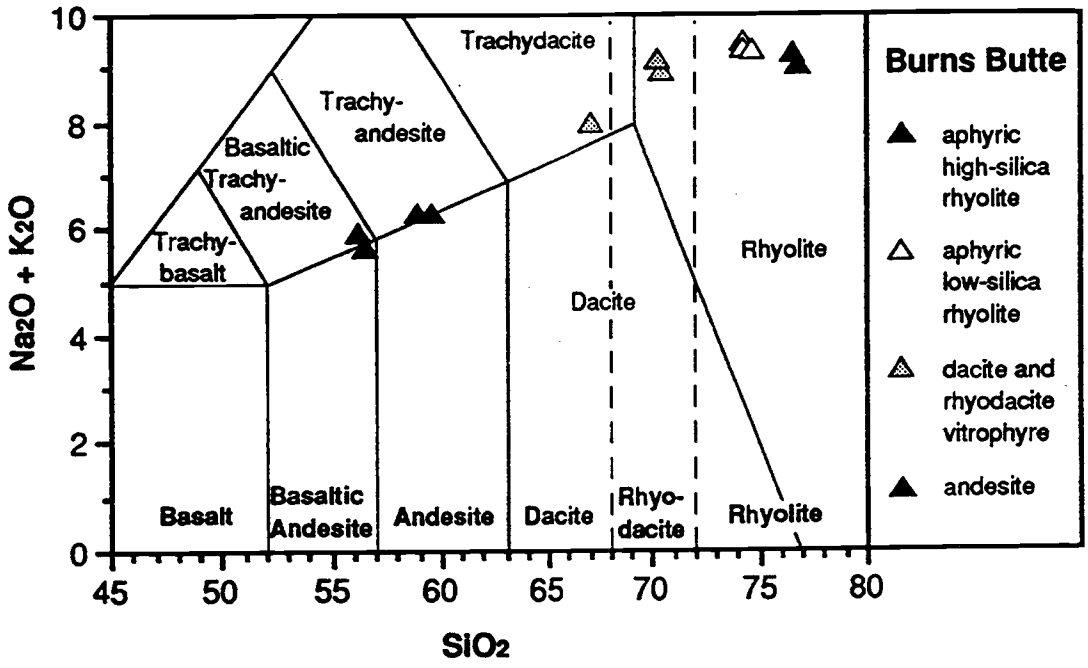

Figure 3.10: $Na_2O + K_2O$ vs. SiO_2 for Burns Butte rocks, with the I.U.G.S. classification scheme of LeBas et al. (1986) shown for reference. Nomenclature is as described in Figure 3.5.

4. Squaw Butte basaltic andesite has extreme enrichments in almost all incompatible trace elements, with only moderate depletions of compatible trace elements.

5. Rhyolites at western Juniper Ridge are related by progressive enrichment of incompatible trace elements and depletion of compatible trace elements.

6. With increasing SiO_2 and decreasing phenocryst content, low-silica rhyolites at eastern Juniper Ridge are regularly and systematically enriched in most incompatible elements and depleted in Ba, Sr, and Sc, at relatively constant Rb.

CHAPTER FOUR: PETROGENESIS AT JUNIPER RIDGE

Since about 17 Ma the Great Basin province has been characterized by extensional tectonics accompanied by what is described as "bimodal" magmatism (Noble, 1972; Snyder et al., 1976), "fundamentally basaltic" magmatism (Scholz et al., 1971; Christiansen and Lipman, 1972; Carlson and Hart, 1987), or both (Christiansen and McKee, 1978; Wernicke et al., 1987; Seedorff, 1991). Despite the bimodal character of the province, individual mid- to late-Miocene eruptive centers along the High Lava Plains are compositionally diverse. Intermediate rocks (basaltic andesite through rhyodacite) occur at some centers (Burns Butte, Double O Ranch area, Juniper Ridge), some silicic centers are devoid of intercalated basalt flows, and many basalts erupted unaccompanied by rhyolite. In this context, intermediate rocks are particularly important because, although they are scarce, they may preserve evidence for genetic links between basalt and rhyolite.

The common association of rhyolite and basalt has been explained in terms of crustal anatexis, where mafic magma originating in the mantle acts as a heat source for the partial melting of crustal rocks to produce rhyolite (i.e. Hildreth, 1981). Alternatively, mafic melts can evolve by crystal fractionation to reach rhyolitic compositions, as has been proposed for layered mafic intrusions and Icelandic volcanoes such as Thingmuli (Carmichael, 1964). Because mafic and silicic volcanic rocks in eastern Oregon have geochemical affinities to oceanic volcanic rocks (McKee et al., 1983; Carlson and Hart, 1987; Bailey and Conrey, 1992; Eby, 1992), and because they erupted in an extensional tectonic setting, both hypotheses must be considered in the petrogenesis of rhyolites at Juniper Ridge.

4.1 Origin of basalt

Regionally extensive, plateau-forming basalts on the High Lava Plains have been studied in some detail. Hart et al. (1984) noted a change in character of mafic volcanism on the High Lava Plains following the 15 to 17 Ma volcanic episode which produced the Steens flood basalts and the main pulse of the Columbia River flood basalt, and proposed that the term HAOT (high alumina olivine tholeiite) be used to describe basalts erupted on the High Lava Plains from about 12 Ma to the present. Post-12 Ma basaltic rocks in southeastern Oregon comprise a continuum of compositions between HAOT and SROT (Snake River olivine tholeiite), contemporaneous basalts from the Snake River Plain. HAOT and SROT are both primitive and show limited compositional variability in comparison to the Steens and Columbia River basalts, but they are chemically and isotopically distinct from each other, leading Hart and Carlson (1987) to suggest that the transitional basalt compostions were derived by mixing between oceanic-type mantle (HAOT) and isotopically-enriched sub-continental mantle (SROT) sources, and that little or no crustal contamination occurred in the petrogenesis of the basalts. Other workers agree that eastern Oregon basalts have oceanic affinities (McKee et al., 1983; Bailey and Conrey, 1992) and that primitive compositions were relatively unaffected by contamination or crystal fractionation (Draper, 1991). Thus, the regional plateau basalts, including those around Juniper Ridge, probably represent almost direct mantle melts that rose rapidly through the crust, and erupted without significant residence time in crustal magma chambers.

As discussed in section 3.3.2, basalts analyzed in this study are transitional between HAOT and SROT, but closer in composition to HAOT. Differences in composition between the three Juniper Ridge basalts can be attributed to crystal fractionation, which produced a slightly evolved basalt (JR-91-14) by removal of olivine, plagioclase and magnetite (Stage 1 of AFC model, section 4.2.2) and to crystal accumulation, which produced a plagioclase-rich porphyritic basalt characterized by depletion of Sr and Ni relative to the primitive plateau basalts. Low Sr in

the plagioclase-rich cumulate is due to incompatibility of Sr in plagioclase at temperatures above about 1220°C (Nielsen, 1992).

4.2 Origin of intermediate rocks

The trace element data presented in Chapter 3 show clear distinctions between eastern and western Juniper Ridge intermediate rocks: linear patterns in the western Juniper Ridge data strongly suggest a magma mixing origin for intermediate rocks, while curvilinear patterns in the eastern Juniper Ridge data and extreme trace element enrichments in the Squaw Butte basaltic andesite must be explained by other processes. Several models, including magma mixing, crystal fractionation (with and without wall-rock assimilation), and zone-refining (as an analogy to a constantly recharging, fractionating magma chamber), were constructed and tested as possible explanations for the trace element variations of the intermediate rocks.

4.2.1 Magma mixing at western Juniper Ridge: In addition to evidence for mixing such as disequilibrium mineral assemblages and textures (Chapter 2), intermediate rocks at western Juniper Ridge have the following geochemical characteristics that are among those required for rocks formed by magma mixing: (1) intermediate compositions are arranged linearly between high-silica rhyolite and basalt on element-element plots; and (2) relative positions of compositions on the linear trends are consistent regardless of the elements considered. Also, unusually high compatible element concentrations (i.e. Ni) and unusually low incompatible element concentrations (i.e. Ba) in the intermediate rocks that are difficult to account for by other processes are easily explained by mixing (Fig. 4.3)

Mixing relationships were evaluated using the general mixing equations of Langmuir et al. (1978), and probable end-member compositions were determined by comparing rock compositions to calculated mixtures between selected end-members. Figures 4.1 and 4.2 were constructed following the procedure of Langmuir et. al (1978), in which element ratio plots are

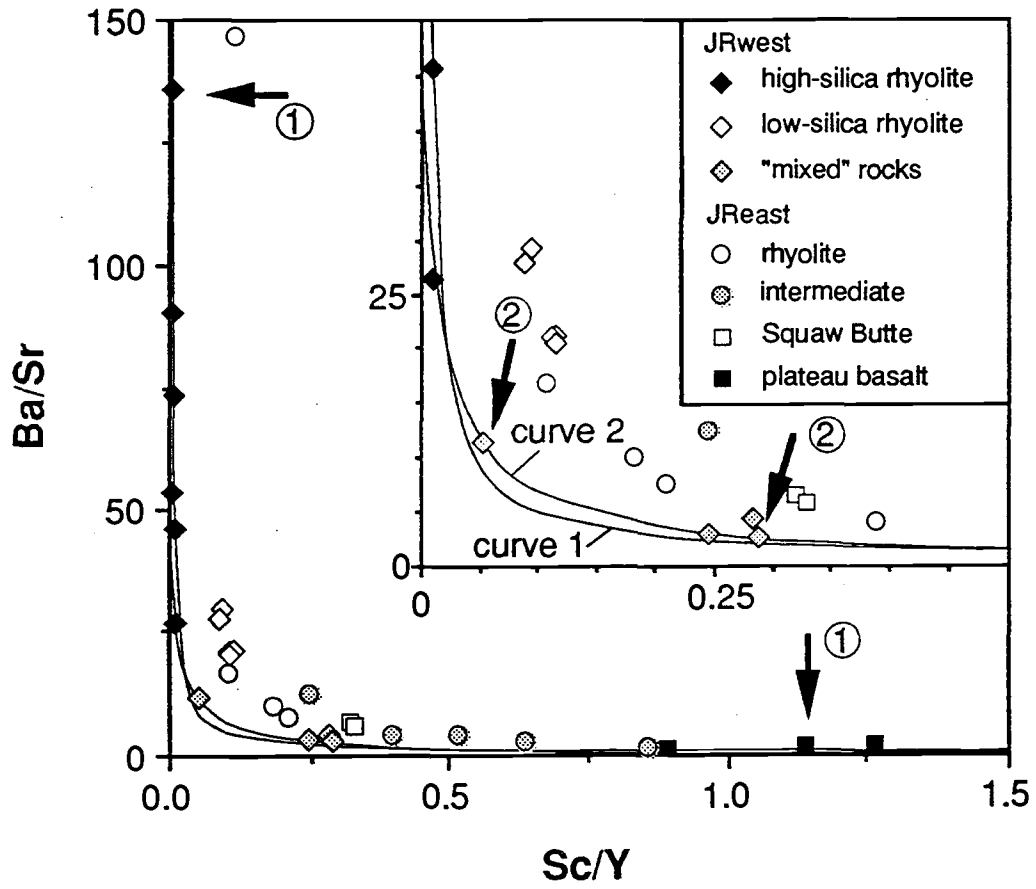

Figure 4.1: Mixing relations between high-silica rhyolite and primitive basalt. Compositions used in calculating mixing curves are shown by heavy arrows. Inset focuses on intermediate and lower silica rhyolite compositions.

used in conjunction with linear "companion plots". Element ratio plots, using elements with drastically different geochemical behavior, are useful because mixing relationships between more than two elements can be tested simultaneously. Companion plots provide a check on the element ratio plots, and because they are linear, consistency of mixing degrees is easier to test. By plotting all of the Juniper Ridge data on Figure 4.1, mixing between basalt and high-silica rhyolite can be ruled out as an origin for eastern Juniper Ridge intermediate rocks, lower silica rhyolites at western Juniper Ridge, and the Squaw Butte basaltic andesite, but is confirmed as a possible origin for western Juniper Ridge intermediate rocks. Curve 1 in Figures 4.1 and 4.2 was

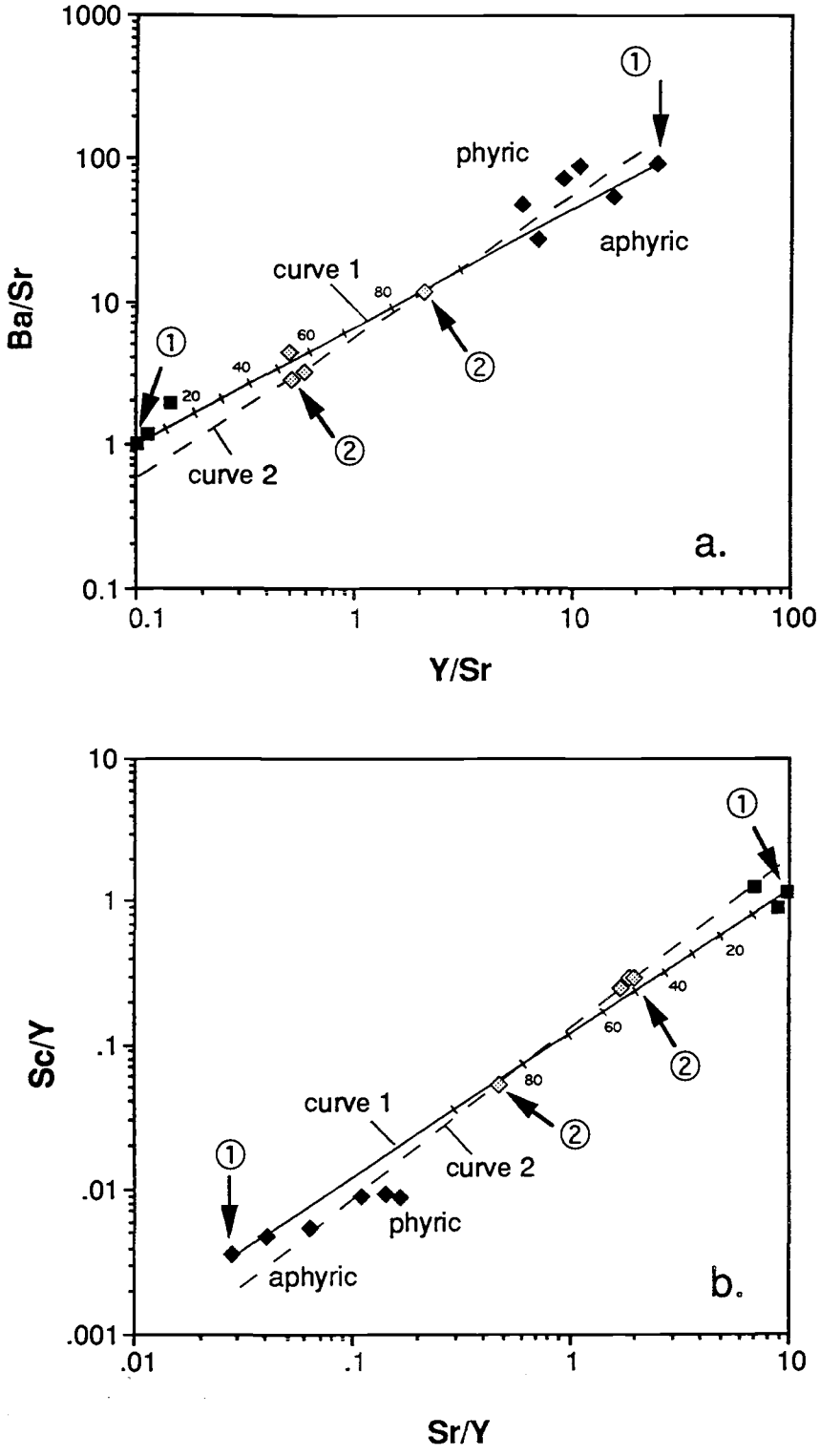

Figure 4.2: Companion plots to Figure 4.1, with end-member compositions for each mixing curve marked by heavy arrows. Degrees of mixing in increments of 10% rhyolite are plotted on curve 1, and high-silica rhyolites are labelled according to crystal content.

calculated using the least-evolved basalt (JR-92-53) and most-evolved high-silica rhyolite (JR-91-4) end-members and demonstrates that for the chosen elements, almost any combination of basalt and high-silica rhyolite could produce the observed hybrids, because all basalts and all but one high silica rhyolite lie on or near the mixing curve. Curve 2 is the mixing curve calculated from the actual mixed compositions, and shows the compositions required if all of the mixed rocks are assumed to have identical end-members. For clarity, only the hybrid rocks and postulated end-members were used in the companion plots.

Available analyses provide a spectrum of compositions from which to choose possible mixing end-members. The end-members for curve 1 were chosen arbitrarily and only approximately fit the observed data. In order to test for more suitable end-members, compositions of the hybrid rocks were compared to the compositions of calculated mixtures between various possible end-member combinations. Aphyric high-silica rhyolite usually provides better fits to the data than crystal-bearing high-silica rhyolite, but regardless of the choice of basaltic end-members, Zr, Sr, Hf and Cr are consistently lower in hybrid rocks than in calculated mixes, and HREE are slightly higher, even when the majority of other elements match the calculated composition to within 10 to 15 percent. Also, mixing relationships shown in Figure 4.2 seem to rule out identical end-members for all hybrids, because no data points intersect the mafic end of curve 2. Therefore, although mixing between basalt and high-silica rhyolite is undoubtedly the origin for the intermediate rocks at western Juniper Ridge, several similar basalt end-members are required in order to reproduce the observed hybrid compositions. Slightly evolved basalt (JR-91-14) seems to provide the best overall fit (see also Figs. 4.4 and 4.5).

Proportions of mixing calculated from major elements are 46% rhyolite for the most mafic hybrid and 88% rhyolite for the most silicic (Figs. 4.2 to 4.5). Average proportions of high-silica rhyolite and basalt calculated from major element data are consistent regardless of the specific end-members that are used, but mixing proportions calculated from trace elements are

variable, ranging from 36 to 55% rhyolite for the most mafic hybrid and from 81 to 89% rhyolite for the most silicic. According to Frost and Mahood (1987), viscosity differences between silicic and mafic magmas prevent homogenization unless the compositional difference between end-members is less than 10% SiO_2 or unless the mass fraction of mafic magma is greater than 0.5. By the terminology of Frost and Mahood (1987) the andesites could be thought of as homogenized, hybrid magmas (except that xenocrysts indicate incomplete equilibration), but the mixed rhyolite is better described as "mingled," namely, a high-silica rhyolite with quenched basaltic inclusions, as the textural evidence confirms (Chapter 2).

Hybridization, mingling, and eruption of the mixed magmas probably occurred within a very short time. Field and petrographic observations suggest that there was no break in eruption between the hybrid andesite lava (Tad_1) and the overlying high-silica rhyolite (Tr_1). The sharp contact between the two is conformable to flow-layering within both, and pods of uncontaminated silicic magma occur in the andesite. Rhyolite and andesite flows each contain xenoliths and xenocrysts of the other, suggesting incomplete equilibration, and lastly, hybrid andesite and "mingled" rhyolite occur in the same stratigraphic position, suggesting that they may have erupted simultaneously. When combined with the chemical evidence for mixing, these observations suggest that hybridization occurred at an interface between basalt and evolved high-silica rhyolite magmas, and that injection of fresh, primitive basaltic magma to the base of the chamber may have initiated eruption, forming the mingled rhyolite in the process.

4.2.2 Assimilation and fractional crystallization at eastern Juniper Ridge: In contrast to western Juniper Ridge, non-linear element variations in the intermediate rocks at eastern Juniper Ridge exclude magma mixing as the main mechanism of differentiation, but are consistent with crystal fractionation from a basaltic magma. Several criteria were used to develop major- and trace-element fractionation models for eastern Juniper Ridge intermediate rocks. First, the models incorporate constraints from both major- and trace element data. Second, mineral assemblages are consistent with those observed in petrographic studies, and

mineral compositions used in the major element model were selected from Juniper Ridge microprobe data. Third, model modes were determined by empirical least-squares calculations (Geist et al., 1989), and are broadly consistent with phase appearances and proportions predicted by experimental models (Mixnfrac = updated version of Nielsen, 1985; Weaver and Langmuir, 1990). Finally, crystal-liquid partition coefficients were adjusted in the trace element model to account for changes in temperature, magma chemistry, and mineral chemistry using data compiled by Nielsen (1992).

Starting compositions, modes and mineral compositions used in the major- and trace-element model are summarized in Table 4.1. Full analyses of parent compositions for each stage of the model are in Appendix 4. The phase assemblages and modes for each stage were estimated initially by least squares mixing using MacGPP (Geist et al. 1989) and adjusted slightly to fit observed chemical variation. Adjustments are less than 10% for calculated mineral abundances greater than 25% of the mode and less than 5% for calculated abundances less than 25%. Phase appearances are roughly consistent with those predicted by experiment-based predictive models such as that of Nielsen (Mixnfrac) and Weaver and Langmuir (1990), except for the relatively early appearance of pyroxene and magnetite, which may reflect higher pressure and/or oxygen fugacity than the one-atmosphere experimental models. In the first stage, modest enrichment of Al_2O_3 (Fig. 4.3) and depletion of Mg and Ni (Fig. 4.4) require concurrent fractionation of plagioclase and olivine. Because even the most primitive HAOT may have experienced small degrees of olivine and plagioclase fractionation (Draper, 1991), fractionation of almost 40% plagioclase in the first stages of the model is considered to be reasonable. Early crystallization of pyroxene is required by Sc, which declines steadily after a small initial enrichment of about 1 ppm (Fig. 4.5). Appearance of ilmenite and apatite are dictated by depletion of TiO_2 and P_2O_5 at about 1.7 % TiO_2 and 0.6 % P_2O_5, respectively (Fig. 4.3). The appearance of orthopyroxene in the fourth stage is justified on the basis of least squares calculations, however orthopyroxene was not observed in the mineralogy of the dacites.

Table 4.1: Mineral modes and compositions used in AFC model

	Stage 1:	Stage 2:	Stage 3:	Stage 4:
F (%)	**0 to 10**	**10 to 40**	**40 to 70**	**70 to 85**
parent	47.6 % SiO_2 (JR-92-53)	49.0 % SiO_2	52.7 % SiO_2	60.9 % SiO_2
plagioclase	37.7 % An_{72} (JR-92-59)	53 % An_{64} (JR-92-48)	59.1 % An_{50} calculated	66 % An_{46} (JR-91-42)
olivine	59 % Fo_{83} (JR-92-59)	10 % Fo_{79} (JR-92-42)	10.5 % Fo_{65} (JR-92-53)	
magnetite	3.3 % Usp_{57} (JR-91-42)	7.4 % Usp_{25} (JR-91-48)	5.4 % Usp_{25} (JR-91-48)	3 % Usp_{25} (JR-91-48)
clinopyroxene		28.7 % $Wo_{41}En_{42}Fs_{17}$ (JR-92-53)	20.4 % $Wo_{38}En_{50}Fs_{12}$ (JR-92-42)	10.5 % $Wo_{40}En_{27}Fs_{33}$ (JR-92-34)
ilmenite		0.9 % Ilm_{94} (JR-91-42)	3 % Ilm_{94} (JR-91-42)	2.2 % Ilm_{94} (JR-91-42)
apatite			1.6 % (DHZ #5)	1.3 % (DHZ #5)
orthopyroxene				17 % $Wo_2En_{72}Fs_{26}$ (JR-92-48)
contaminant	r = 0.22 rhyolite (JR-92-48)	r = 0.15 rhyolite (JR-92-48)	r = 0.10 rhyolite (JR-92-48)	r = 0

F = % crystallized; r = rate of assimilation/rate of crystalization (DePaolo, 1981); mineral compositions are from tables in Chapter 3 unless otherwise noted (DHZ = Deer et al., 1966); An_{50} plagioclase in Stage 3 is a composite calculated by least-squares (Geist et al., 1989); full analyses of starting compositions for each stage are in Appendix 4.

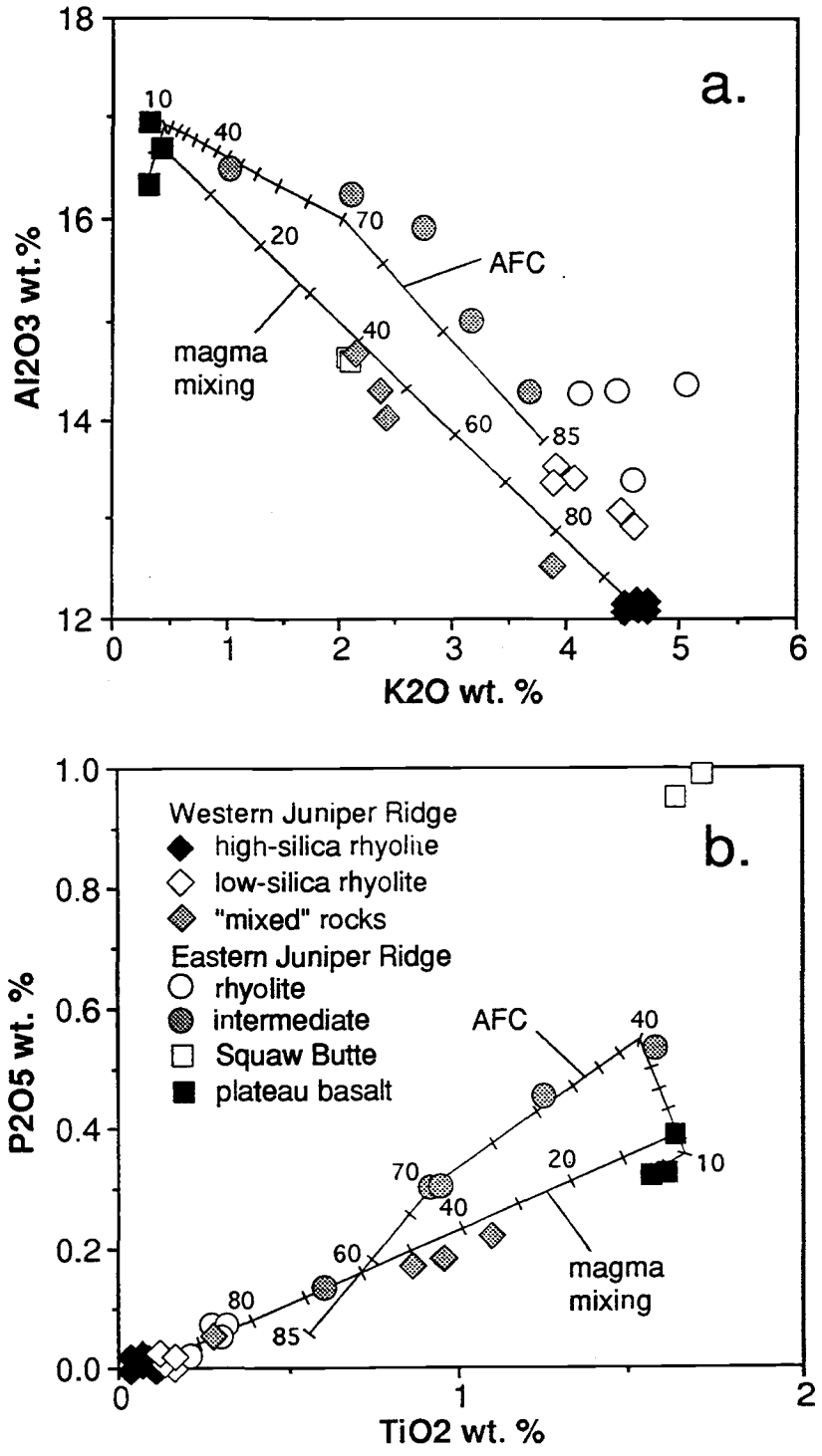

Figure 4.3: Results of major element models for intermediate rocks at Juniper Ridge, including paths of evolution for assimilation and fractional crystallization (AFC) and for magma mixing. Degrees of fractionation during AFC are marked in 5% increments, degree of mixing is marked in increments of 10% rhyolite.

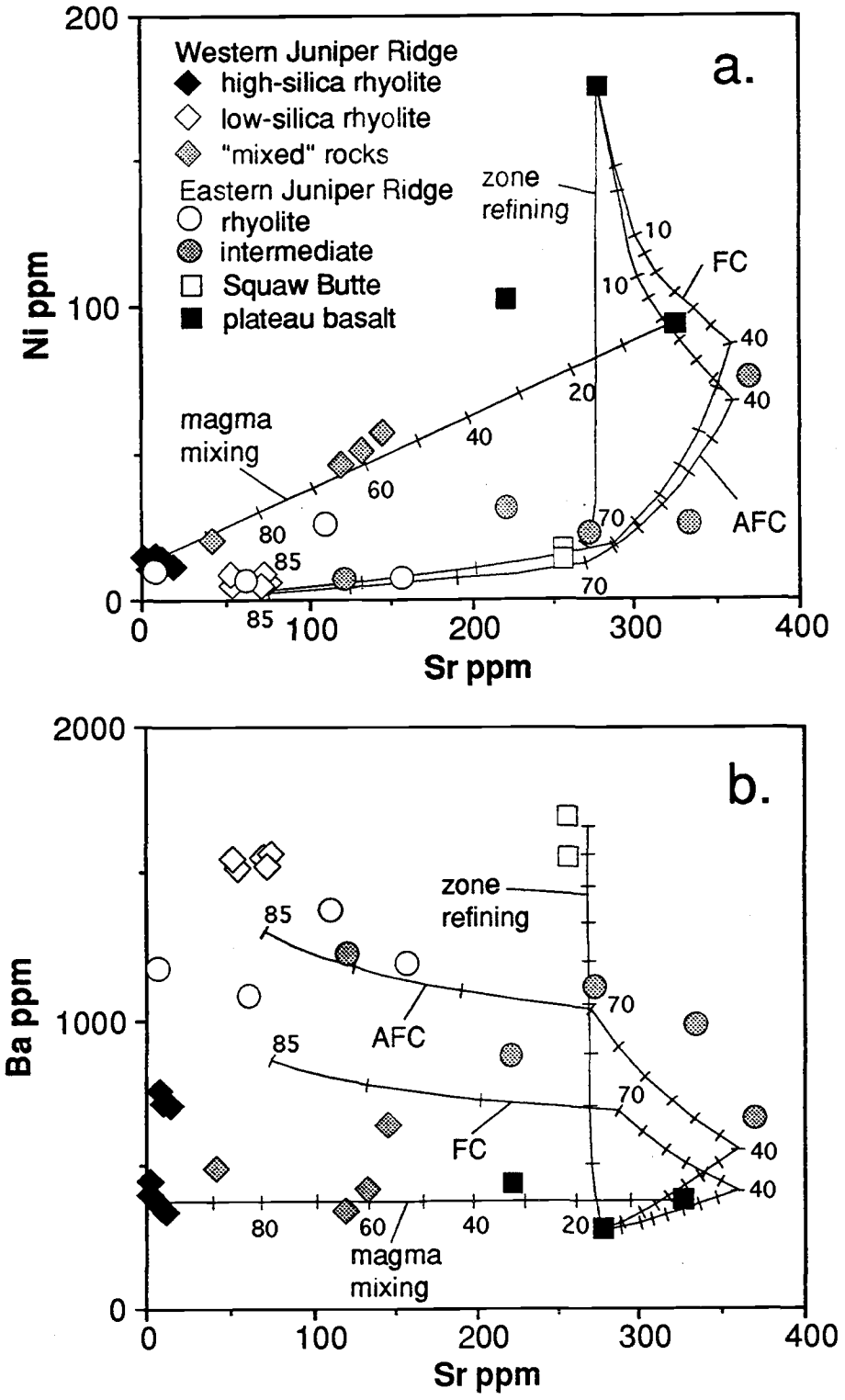

Figure 4.4: Trace element variation diagrams showing the results of geochemical models for Juniper Ridge intermediate rocks, including fractional crystallization (FC), fractional crystallization accompanied by wall-rock assimilation (AFC), zone refining and magma mixing models.

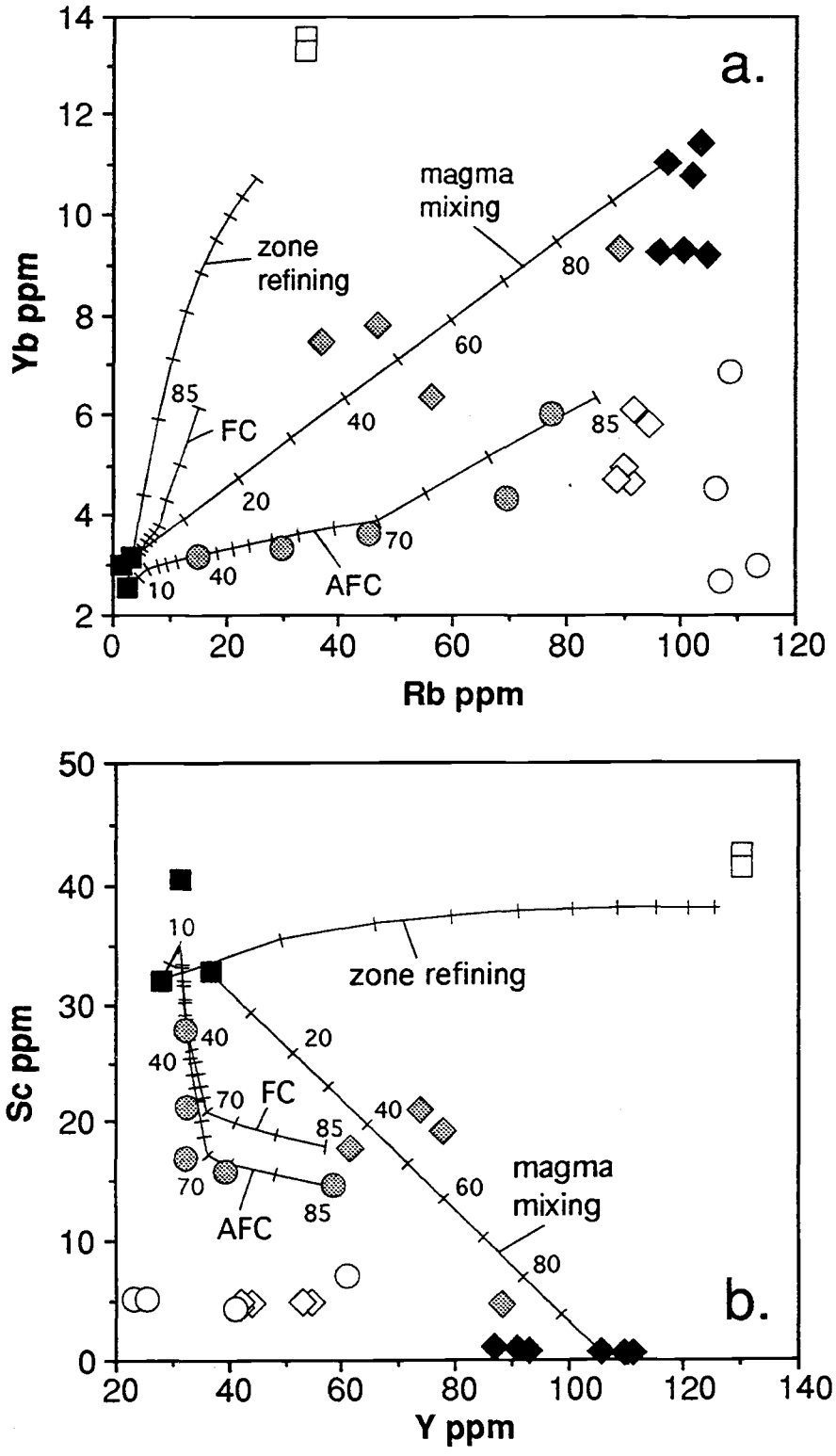

Figure 4.5: Trace element diagrams showing the results of geochemical models for intermediate rocks. Symbols are the same as in Figure 4.4

For internal consistency between models of major- and trace-element variations and in order to account for incompatible trace element enrichments that are greater than can be accomplished by fractionation alone, crystal fractionation must be accompanied by considerable assimilation of partially melted wall rock. The percentage and composition of crustal contaminant in the mode was determined by trace element data, as described below.

Mineral compositions used in the major element model were chosen from Juniper Ridge mineral data (Chapter 3), except for the apatite analysis (Sample #5; Deer et al., 1966). General mineralogical features of the model are that olivine decreases in abundance with evolution and becomes less magnesian, plagioclase increases in abundance and becomes less calcic, clinopyroxene becomes less calcic and less magnesian with evolution, and magnetite is less titaniferous after the first stage.

Trace element variations in eastern Juniper Ridge intermediate rocks are accounted for in a model that uses the assimilation and fractionation (AFC) equations of DePaolo (1981) and the same modes as the major element model (Table 4.1). Appendix 5 contains partition coefficients and assimilation rates used in the trace element model. Partition coefficients were estimated for each stage with the program BIGD.FOR (Nielsen, 1992), which uses melt composition- and temperature-dependent mineral-melt expressions derived from a large experimental data set. For pyroxene and titanomagnetite, additional constraints on partitioning behavior are provided by mineral chemistry. Appropriate temperatures for each stage of the model were selected with reference to the predictive models of Neilsen (Mixnfrac) and Weaver and Langmuir (1990), both of which predict plagioclase and olivine appearing on the liquidus at about 1225°C. Relatively high temperatures are required to account for the incompatible behavior of Sr*, which increases by almost 100 ppm in the initial stages of the model

* The model of Blundy and Wood (1991) predicts $Kd_{Sr}^{plagioclase} > 1$ for the temperature and feldspar composition used in the first two stages of the model, but according to Nielsen (pers. comm. 1993), the data of Drake and Weill (1975) used in BIGD.FOR (Nielsen, 1992) is more appropriate for temperatures above about 1200°C, because the estimate of Blundy and Wood (1991) is extrapolated from lower-temperature data.

Some partition coefficients estimated from BIGD.FOR (Neilsen, 1992) were adjusted in the model to better fit observed elemental variation. In particular, slightly larger partition coefficients, appropriate for higher-pressure, were used for REE and Y in clinopyroxene, even though lower-pressure Sc partition coefficients provide a better fit to the data. Green and Pearson (1983) showed that partition coefficients for the rare earth elements increase with an increase in pressure, and that the increase is larger for the light rare earths. Slightly smaller partition coefficients than those recommended by Nielsen (1992) are necessary for $Kd_{Ni}^{olivine}$ and $Kd_{Ni}^{clinopyroxene}$ to account for observed variation in Ni. Kd values for Ni used in the model are within the range for basaltic magmas reported in the literature (e.g. Henderson, 1982).

Other partition coefficients predicted by BIGD.FOR are clearly inapproriate for the Juniper Ridge data and were not usable in the model. Partition coefficents for the transition metals, especially Cr, Co, V and Zn, in oxide minerals are especially problematic. BIGD.FOR (Nielsen, 1992) predicts Kds for Cr that are much too high in magnetite, for Co and Zn that are too low in magnetite, and for V that are too low in ilmenite to account for observed variations in the above elements. The model partition coefficients for Cr, Co, V and Zn were therefore selected to fit the Juniper Ridge data, and are not based on experimental data, but are within the range of values reported in the literature (Irving, 1978; Dostal et al., 1983).

For many incompatible trace elements (especially Rb, Ba, Ta, Th, and LREE), observed enrichment with evolution in the eastern Juniper Ridge suite is substantially greater than can be accounted for by fractionation alone (Figs. 4.4, 4.5). A rhyolite from eastern Juniper Ridge was chosen as the crustal contaminant, because it is thought to represent a partial crustal melt (section 4.3.3), and because it contains high Ba, high Rb and low REE in comparison to the basaltic parent, thus allowing increase of Ba and Rb without greatly affecting REE in the model. The parameter r (mass of assimilant with respect to mass of fractionates; DePaolo, 1981) was chosen by balancing the required enrichment of Ba and Rb (enriched by assimilation) with the

neccessity of enriching Sr (depleted by assimilation) in the initial stages of fractionation. The amount of contaminant needed in successive stages decreases.

The combined major and trace element model presented above is not intended to be unique, but is considered robust because it can explain the chemical variation in the intermediate rocks at eastern Juniper Ridge by incorporating a wide range of geochemical, mineralogical and experimental constraints. As discussed above, deviations of model parameters from experimental data are few, and can be explained by different conditions (higher pressure and/or oxygen fugacity) during magma evolution than those in the experiments.

Several important conclusions can be reached from the AFC model. For one, the model ties all Juniper Ridge intermediate rocks to a common basaltic parent: the same regional basalt (JR-91-14) that is a likely end-member for mixing in western Juniper Ridge intermediates lies along the fractionation path that produced eastern Juniper Ridge intermediates. Second, scatter of the eastern Juniper Ridge data around the liquid lines of descent derived from the model (Figs. 4.4, 4.5) implies that the rocks may not come from the exact same batch of magma, but were produced by very similar processes. Small eruptive volumes also suggest that the intermediate rocks were produced independently in small, unconnected magma chambers. Third, the model predicts that the rate of wall-rock assimilation is higher in the initial stages of fractionation and declines as temperature decreases. This suggests that input of heat from underplating basaltic magma was not continuous at eastern Juniper Ridge, but sporadic, allowing individual batches of basaltic magma to fractionate in place before injection of new magma. Fourth, the liquid lines of descent calculated from the model fail to account for the trace element characteristics of the rhyolites, thus ruling out a fractionation origin for the silicic rocks at Juniper Ridge (see section 4.3).

4.2.3 Zone refining or recharge and crystallization at Squaw Butte: The unusual composition of the Squaw Butte basaltic andesite presents an interesting petrologic problem. Concentrations of incompatible trace elements are much too high to be explained by

assimilation and fractional crystallization, even if extremely high rates of assimilation are assumed. Extreme enrichments of incompatible elements can be achieved by processes such as zone refining (Cox et al., 1979), in which a body of magma consumes wall rock of identical composition at the same rate as it solidifies. Similar geochemical results can be expected in a magma chamber experiencing periodic recharge of primitive magma along with fractionation and bulk assimilation of wall-rock. In both processes, incompatible trace elements are constantly replenished in the magma, but are excluded from fractionating phases and can be highly enriched, while major and compatible element concentrations are buffered to the composition of the added material, either the newly injected magma or assimilated wall-rock. Figures 4.4 and 4.5 show the results of zone refining calculations, offered as an analogy for a recharge model, using a HAOT starting composition, a fractionating assemblage that includes olivine, plagioclase, clinopyroxene and magnetite (ol:pl:cpx:mgt = 60:25:10:5), and partition coefficients listed in Appendix 5. Each step represents assimilation of a volume of wall rock equivalent to the volume of the magma chamber along with removal of the same volume of crystals, so that the size of the chamber is constant. Although the steps required to reach Squaw Butte basaltic andesite compositions are fairly high (nine are shown in Figs. 4.4 and 4.5), the model produces compositional trajectories that point in the right direction, while other models (AFC, FC and mixing) fail to do so.

An objection to the applicability of zone refining to geological situations is that it requires large volumes of crust similar in composition to the injected magma, as well as an abundant, continuous source of heat (Cox et al., 1979). Likewise, fractionation and recharge has been proposed for areas such as island arcs, where magma production is both voluminous and steady (O'Hara, 1977). At Squaw Butte, either zone refining or recharge seems possible in light of abundant basaltic volcanism and probable mafic crustal composition of the High Lava Plains.

4.3 Origin of rhyolites

Modelling of rare earth element patterns, characterized by rhyolites depleted with respect to basaltic and intermediate rocks (Chapter 3), indicates that rhyolites at both western and eastern Juniper Ridge could not have evolved as fractionates from the observed intermediate compositions, because to do so would require abrupt reversals of behavior in many trace elements from incompatible to compatible and to incompatible again (i.e. Y, Yb; Fig. 4.5). This is considered unlikely because it requires the sudden appearance and disappearance of trace mineral phases, none of which, apart from zircon in rhyolite, are observed in the rocks. Therefore, rhyolites at Juniper Ridge probably originated as partial melts of the crust. Trace element variations *within* rhyolite suites, on the other hand, imply that the silicic melts may have been modified by varying degrees of crystal fractionation.

4.3.1 Dehydration melting: Indirect evidence points to dehydration melting of amphibolite crust as the probable origin of Juniper Ridge rhyolites. This evidence includes: (1) geophysical and isotopic evidence that the lower crust beneath the High Lava Plain is composed of primitive, mafic material (Catchings and Mooney, 1988; Wilson et al. 1983; Hart, 1984), and (2) experimental melts produced by melting of amphibolite that provide close compositional matches to Juniper Ridge rhyolites (Beard and Lofgren, 1991; Rapp et al., 1991).

Although no basement rocks are exposed in the High Lava Plains, geological studies of the surrounding areas support the inference that the crust is composed of mafic material. In the Blue Mountains, directly to the north of the High Lava Plains, a belt of volcanic arc rocks known as the Huntington arc terrane can be traced southward to the Juniper Ridge area (Dickinson, 1979). Catchings and Mooney (1988) derived a crustal velocity model for southeastern Oregon based on a 180 km seismic refraction transect from the eastern Cascades, through the Newberry Volcano, and eastward to the Harney Basin. They discerned a high velocity (6.5 km/sec) layer from 15 to about 30 km that they interpreted as amphibolite. Below the

amphibolite layer, to a depth of 35 km, is a slightly higher velocity (7.4 km/sec) layer that they believe is mafic material added to the base of the crust during extension.

Reconnaissance isotopic studies on rhyolites and basalts in southeastern Oregon, southwestern Idaho and northern Nevada also suggest that the crust underlying the High Lava Plains is mafic in character. To the east of an isotopic boundary that marks the western edge of the North American craton in Idaho, rhyolites have elevated initial strontium isotopic ratios that indicate derivation from evolved crust (Hart, 1984). To the west of the boundary, in southeastern Oregon, rhyolites have initial strontium isotopic ratios that are identical to associated basaltic rocks (Hart, 1984; Wilson et al., 1983), suggesting that they were derived from a primitive mafic source. Hart and Carlson (1987) believe that the crust beneath southeastern Oregon was created by back-arc spreading during early Miocene time, but whatever its origin, either as accreted island arc terranes or as newly generated crust behind the Cascades arc, most workers agree that the lower crust in southeastern Oregon is composed of primitive, mafic material.

Somewhat more direct petrologic evidence that Juniper Ridge rhyolites were produced from an amphibolite parent comes from recent dehydration melting experiments. Experiments show that melting under water-saturated conditions almost invariably produces peraluminous melts (e.g. Beard and Lofgren, 1991; Rapp et al., 1991; Wolff and Wylie, 1992). Metaluminous melt compositions can, however, be produced by dehydration melting, in which water is present only through the breakdown of hydrous phases such as biotite and amphibole. For example, melt compositions reported by Rapp et al. (1991), who used an olivine-normative amphibolite protolith, are almost identical to high-silica rhyolites at western Juniper Ridge at about 7% melting. Beard and Lofgren (1991) melted an amphibolite with major element composition nearly identical to HAOT, and produced silicic melts (through 5 to 30% melting) similar in major element composition to the least-evolved rhyolites at Juniper Ridge, with the exception that K_2O values in the experimental melts are 2 to 3 wt. % lower than in Juniper Ridge rocks. K_2O concentration in the amphibolite melts is extremely sensitive to its concentration in the starting

material, but elevated K_2O may also result from the presence of K-rich phases such as biotite or alkali feldspar in the melt protolith (Patino-Douce and Johnston, 1991). Melts derived from dehydration melting of metapelites are also high in potassium but are almost uniformly peraluminous (Wolff and Wylie, 1992; Vielzeuf and Holloway, 1988).

4.3.2 Fractionation from low-silica rhyolite: Compositional variation within the rhyolite suites could have been produced in at least two ways: by variations in degree of crustal melting (progressive partial melting), or by modification of crustal melts by subsequent processes such as crystal fractionation or contamination. Trace element systematics argue against progressive partial melting and in favor of crystal fractionation in the petrogenesis of the rhyolites.

For example, if the rhyolites at eastern Juniper Ridge are progressive partial melts, the protolith must have high initial Rb and Ba content and must have bulk D_{Rb} and $D_{Ba} \geq 1$ in order to buffer Rb and Ba at constant, high values in progressive melts (Figs. 4.4 and 4.5). Biotite is the most likely major phase that has both high Kd_{Ba} and Kd_{Rb}. However, a biotite-bearing amphibolite protolith cannot produce progressive melts that match eastern Juniper Ridge compositions and trends because biotite and amphibole also have high partition coefficients for Nb and Y (Pearce and Norry, 1979; Nash and Crecraft, 1985), both of which must be incompatible in the melt residuum in order to be depleted in progressive melts. Generation of the observed trace element patterns of Juniper Ridge rhyolites by progressive partial melting is therefore considered unlikely.

In contrast, it is possible to devise trace element models (Figs. 4.6 and 4.7) in which sanidine, plagioclase, quartz, pyroxene, magnetite and trace zircon and allanite are removed from lower silica rhyolites in order to arrive at observed higher-silica rhyolite compositions, using the modes and partition coefficients in Appendix 5. Sources for trace element partition coefficients for rhyolites include Nash and Crecraft (1985), Mahood and Hildreth (1983), Sawka (1988), Arth (1976), and Pearce and Norry (1979).

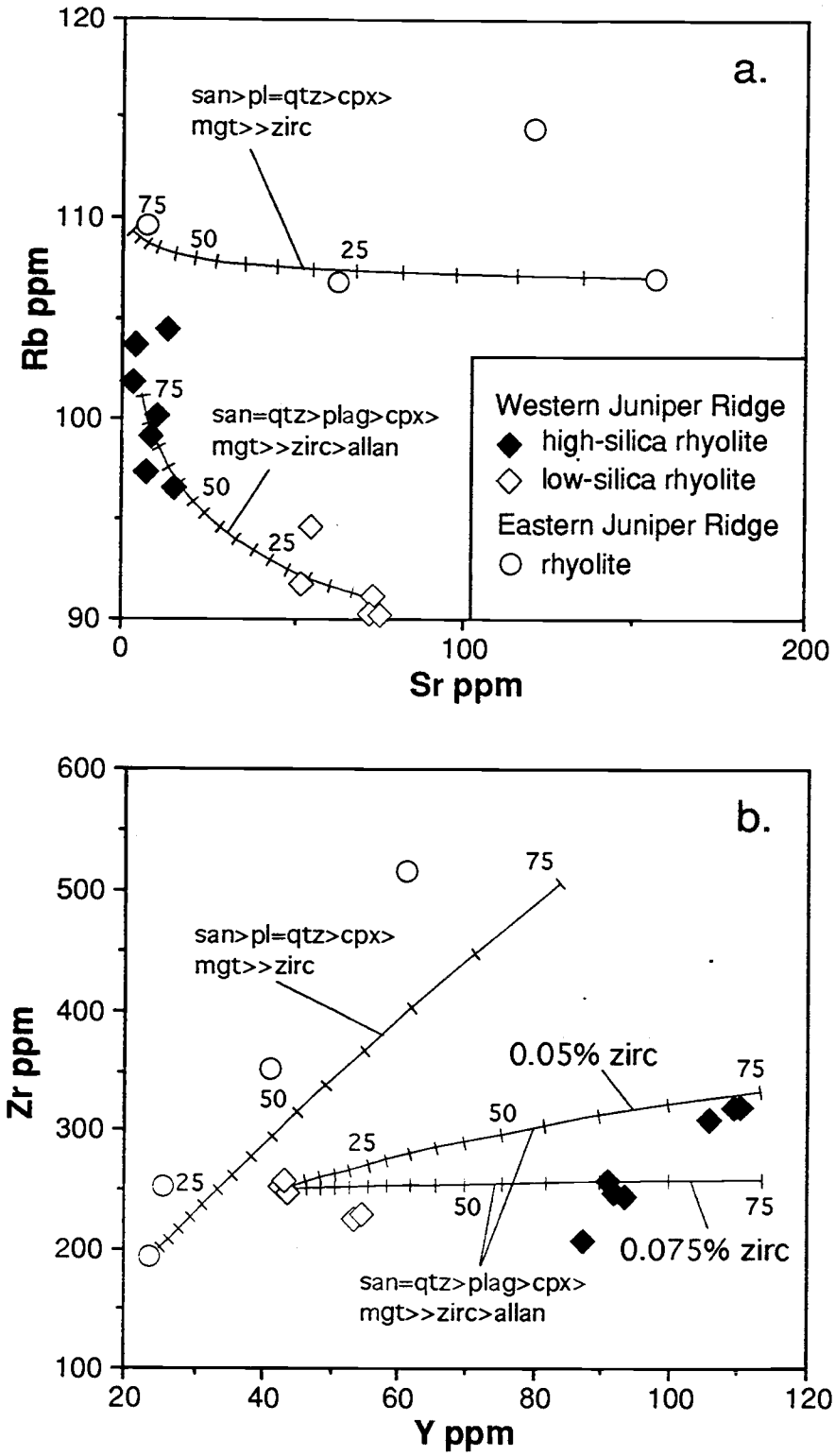

Figure 4.6: Trace element diagrams showing possible petrogenetic models for the derivation of high-silica rhyolites by crystal fractionation. Modes for the two models are given in Appendix 5.

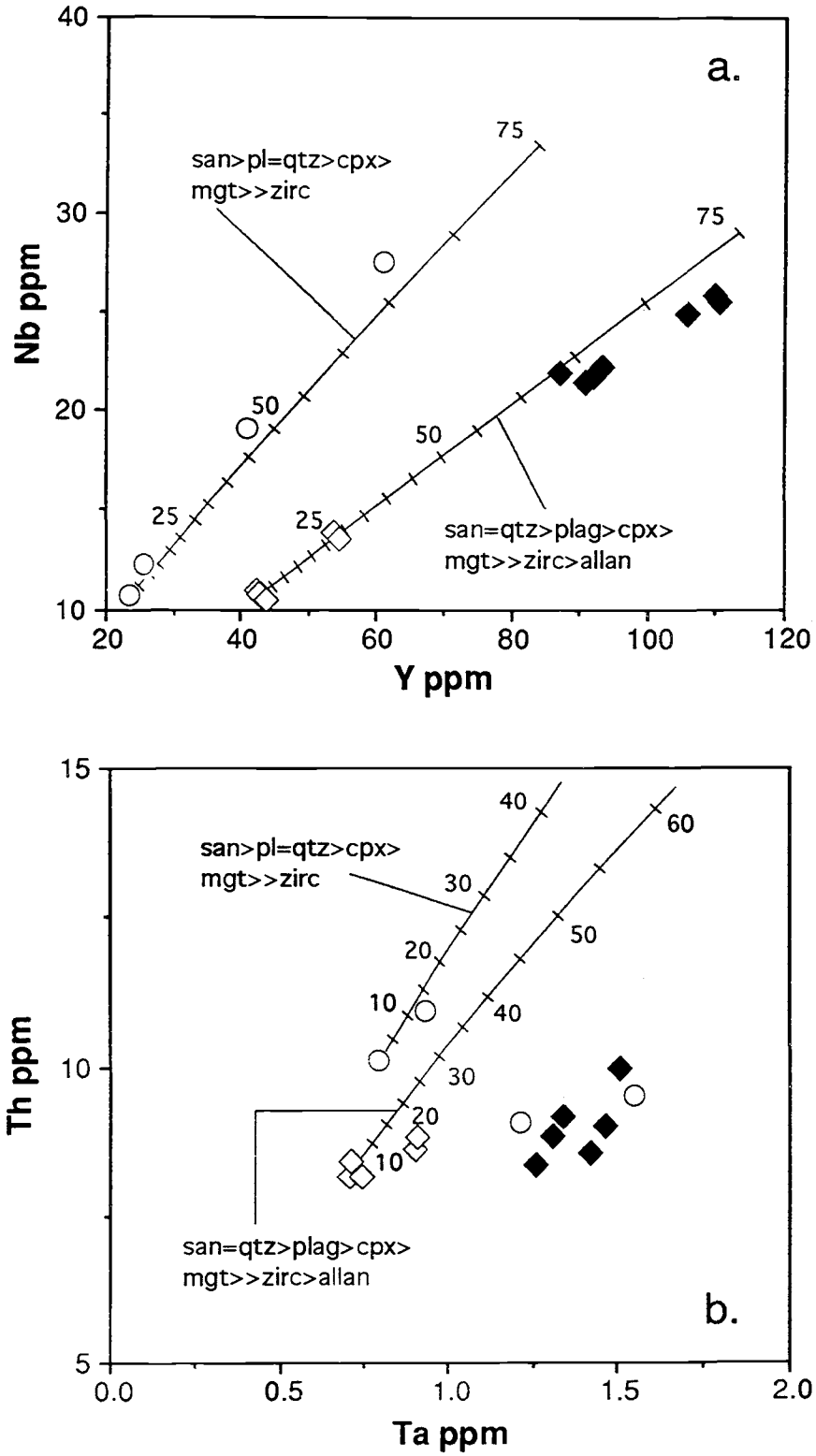

Figure 4.7: Trace element diagrams showing possible petrogenetic models for the derivation of high-silica rhyolites by crystal fractionation. Symbols as in Figure 4.6.

At both eastern and western Juniper Ridge, elevated incompatible elements (Y and Nb, Figs. 4.6 and 4.7) in the high-silica rhyolites require considerable amounts of quartz in the fractionating assemblage in order to dilute the effects of clinopyroxene, which has $Kd_Y > 1$ and $Kd_{Nb} = 1$ (Pearce and Norry, 1979). Differences in the behavior of Rb (Fig. 4.6a) can be accounted for by more or less sanidine in the fractionating assemblage, however, Ba variations (not shown) require bulk $D_{Ba} = D_{Rb}$ for eastern Juniper Ridge rhyolites and bulk $D_{Ba} > D_{Rb}$ for western Juniper Ridge rhyolites.

Near-constant or declining abundances of Zr with differentiation at western Juniper Ridge (Fig. 4.6b) and Th at eastern and western Juniper Ridge (Fig. 4.7b) are problematic because zircon and allanite are the only common igneous phases that can significantly increase bulk partition coefficients for Zr, Hf, and Th, but zircon and allanite also have extremely high partition coefficients for HREE and LREE, respectively (Sawka, 1988). Therefore, the percentage of both in the model assemblage must be low in order to maintain low bulk partition coeffients for the rare earth elements (for example, bulk D_{Yb} and bulk D_{La} cannot exceed 0.3 and 0.7, respectively, at 60 % fractionation). Modest amounts of zircon in the fractionating assemblage can explain variation of Zr (Fig. 4.6b), but even when extremely generous partition coefficients for Th in magnetite and allanite are used, fractionation models fail to account for the lack of significant increase of Th in Juniper Ridge rhyolites (Fig. 4.7b).

Crystal fractionation models for rhyolites, especially high-silica rhyolites, are difficult to evaluate because of uncertainties in partitioning behavior and relative lack of experimental constraints on phase equilibria compared with basaltic systems. Wide ranges of reported partition coefficients in the literature allow flexiblity in modelling rhyolites, but such models are rarely unique. The models presented in Figures 4.6 and 4.7 are therefore not meant to be exclusive of other options, but serve to show that derivation of the high-silica rhyolites by crystal fractionation is possible, if not probable.

4.4 Discussion and conclusions

The petrogenesis of rocks at Juniper Ridge shows that a wide range of rock types can be produced by diverse magmatic processes in areas considered to be "bimodal" or "fundamentally basaltic." Still, both terms are accurate in a regional sense because (1) volcanism in the area is dominated by both basaltic and rhyolitic compositions, (2) significant compositional gaps are present even in suites with intermediate rocks, and (3), perhaps most importantly, the petrogenesis of intermediate and silicic rocks seems to be intimately tied to the presence of regional basaltic magmas.

Results of major and trace element modelling show that several processes acted to produce the range of rock compositions observed at Juniper Ridge. When these constraints are combined with age data and field relations, a scenario for the development of Juniper Ridge can be constructed (Fig. 4.8).

First, it should be noted that despite a common basaltic parent and mixing end-member, the magmatic systems at eastern and western Juniper Ridge evolved independently in time and in location. In order to compare the differences in petrogenesis at eastern and western Juniper Ridge, Figure 4.8 shows the systems overlapping in time, but dating shows that events at eastern Juniper Ridge preceded those at western Juniper Ridge by about 1 Ma.

At both eastern and western Juniper Ridge, basalt compositions are only slightly more evolved than primitive HAOTs, suggesting that voluminous mantle-derived basaltic magma experienced only slight fractionation of olivine and plagioclase before being erupted to the surface (Fig. 4.8a). Partial melting of amphibolitic lower to middle crust, in response to heat input from the basalts, resulted in ponding of basaltic magma, where it either mixed directly with rhyolitic melts (western Juniper Ridge), or evolved locally to dacitic compositions by crystal fractionation accompanied by assimilation of rhyolite (eastern Juniper Ridge).

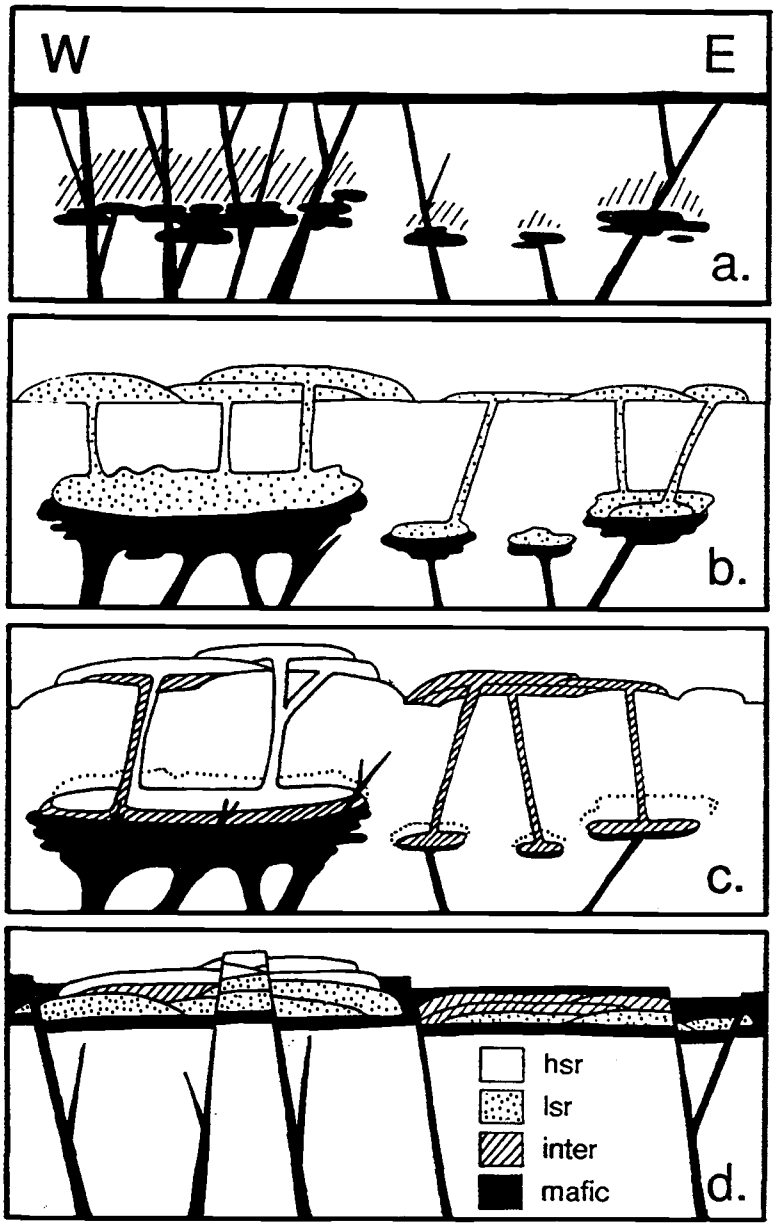

Figure 4.8: Stages in the development of eastern and western Juniper Ridge. Events at eastern Juniper Ridge precede those at western Juniper Ridge by about 1 Ma. a. Inception of extension allows the intrusion and eruption of mafic melts from the mantle. Ruled area shows crust subject to heating and partial melting. b. partial melts coalesce to form silicic magma chambers, with larger chambers in areas of greater extension and mafic input (cf. Hildreth, 1981). c. Silicic magmatism wanes with cooling; dotted lines show former extent of rhyolitic magma chambers. At western Juniper Ridge, rhyolite evolves to high-silica compositions and mixes with underplating basalt to form intermediate hybrids. Some basaltic intrusions penetrate into the rhyolite chamber to form mingled magmas. At eastern Juniper Ridge, mafic magma evolves by crystal fractionation to produce intermediate rocks. d. Basaltic eruptions and faulting resumes following solidificaton of silicic magma.

At western Juniper Ridge, a relatively large silicic magma chamber was tapped periodically by eruptions that record at least two stages of development of the chamber: an early, less-evolved stage (4.8b) and a later, high-silica rhyolite stage (Fig. 4.8c). Intermediate rocks formed late in the history of western Juniper Ridge by mixing and mingling between high-silica rhyolite and primitive basalt, perhaps at an interface between the silicic magma chamber and underplating basalts (Fig. 4.8c). Eruption of the hybrid magma probably occurred very shortly after mixing, and may have been triggered by injection of fresh basalt to the base of the chamber. Declining volumes of increasingly evolved rhyolite (Chapter 2), trace element evidence that high-silica rhyolite evolved from lower-silica rhyolite (section 4.3.2), and mineral data that record a decrease in temperature from lower-silica rhyolite to high-silica rhyolite (section 3.2.5) may reflect progressive solidification of the western Juniper Ridge magma chamber.

At eastern Juniper Ridge, exposed volumes of silicic magma are much less than at western Juniper Ridge, and the compositions of silicic and intermediate rocks are much more diverse. Silicic rocks probably evolved from scattered pods of melted crust by crystal fractionation (Fig. 4.8b), or alternatively, represent different degrees of melting from similar crustal sources, while intermediate rocks evolved in small mafic chambers to dacitic compositions accompanied by up to 20 percent assimilation of rhyolitic partial melt (Fig. 4.8c). The amount of contaminant required by the trace element model decreases with evolution, which is consistent with successively lower magma temperature, and lack of fresh mafic magma.

After the decline of silicic volcanism at eastern and western Juniper Ridge, basaltic volcanism resumed, followed by faulting (Fig. 4.8d).

Differences in the evolution of rocks at western and eastern Juniper Ridge may be due to local variations in extension along the High Lava Plains. Hildreth (1981) emphasized that small variations in degree or rate of extension affects the amount of heat provided by basaltic intrusion, and hence the degree of partial melting of the overlying crust. At western Juniper Ridge, greater extension may have allowed greater degrees of partial melting, resulting in a

large, compositionally homogeneous silicic magma chamber which was tapped to form relatively thick, widespread flows, while at eastern Juniper Ridge, less extension resulted in generation of small, independent magma chambers that produced smaller volumes of compositionally diverse silicic eruptives (Fig. 4.8b). Northwest-trending faults of the Brothers fault zone that dissect western Juniper Ridge are largely absent at eastern Juniper Ridge, where rocks are mainly exposed along a single east-west trending normal fault. Influx of mafic magma may therefore have been less at eastern Juniper Ridge, resulting in less crustal melting and lower volumes of rhyolite.

CHAPTER FIVE: TRACE ELEMENT VARIATIONS IN AGE-PROGRESSIVE RHYOLITES ALONG THE HIGH LAVA PLAINS

During the course of the study, age and chemical data were collected from Juniper Ridge and from other dome complexes and ash-flow tuffs of the High Lava Plains age-progressive trend. Regional chemical variations and an interpretation of their petrologic significance are presented in this chapter.

Trace element systematics were used to identify batches of related melts and to evaluate differences in magmatic history. Ratios of highly incompatible trace elements are not likely to change during the course of most magmatic processes, and thus may be characteristic of batches of magma with similar protolith and melting history. Elements compatible only in selected mineral phases may be used as tracers for those minerals in subsequent petrogenetic processes such as wall-rock assimilation and crystal-liquid fractionation.

Despite differences in mineralogy and petrologic history, rhyolites along the 5 to 10 Ma portion of the High Lava Plains trend exhibit trace element signatures that vary systematically with age and geographic position. These systematic variations are important because they may reflect changes in petrogenesis of the rhyolites through time, and therefore have implications for the tectonic and magmatic evolution of the High Lava Plains.

5.1 Location, age, and petrology of rhyolite suites in western Harney Basin

The volcanic suites exposed at Juniper Ridge are two of at least ten rhyolite vent complexes, with ages between 5 and 10 Ma, located in the western half of the Harney Basin (Fig. 5.1). Other rhyolite dome complexes in the western Harney Basin for which age and geochemical data are currently available include (from east to west) Burns Butte (7.5 to 7.8 Ma), Palomino Butte (6.5 Ma), and Glass Buttes (4.9 Ma). Contemporaneous, regionally extensive ash-flow tuff sheets in the area include the Devine Canyon Tuff (9.7 Ma), the Prater Creek Tuff (8.4 Ma), the Rattlesnake Tuff (7.1 Ma) and the tuff of Buckaroo Lake (6.8 Ma). Vent locations for the ash-flow tuffs have yet to be positively identified, but outcrop patterns, isopach maps, and facies variations within the deposits indicate possible sources in the Harney Basin and allow rough estimates to be made as to locations of vents (Fig. 5.1).

Rhyolites from the western Harney Basin include silica compositions from 72 to 77 wt. % SiO_2, and are either aphyric, or contain a few percent anhydrous minerals such as sanidine, plagioclase, pyroxene and Fe-Ti oxides. Biotite and hornblende-bearing rhyolites occur at Palomino Butte and at Glass Buttes but are relatively minor. Short summaries of age relations, rock types, and mineralogy of the western Harney Basin rhyolite vent complexes follow.

5.1.1 Burns Butte: Burns Butte is the easternmost rhyolite dome complex in the western Harney Basin. Rocks exposed at Burns Butte include andesite, porphyritic dacite and rhyodacite (67.0 to 70.4 wt. % SiO_2), and aphyric rhyolite (lower-silica: 74.2 to 74.3 wt. % SiO_2; higher-silica; 76.5 to 76.8 wt. % SiO_2; section 3.3.6). K-Ar age data and field exposures suggest that the aphyric rhyolite (7.8 Ma) pre-dates the porphyritic dacite and rhyodacite (7.5 Ma; Brown, 1982). New ^{40}Ar-^{39}Ar dating of aphyric rhyolite (7.75 ± 0.06 Ma; Grunder and Deino, unpub. data) confirms the previous K-Ar age. Porphyritic dacites and rhyodacites at Burns Butte contain 5 to 15 percent phenocrysts of sanidine > plagioclase > clinopyroxene >

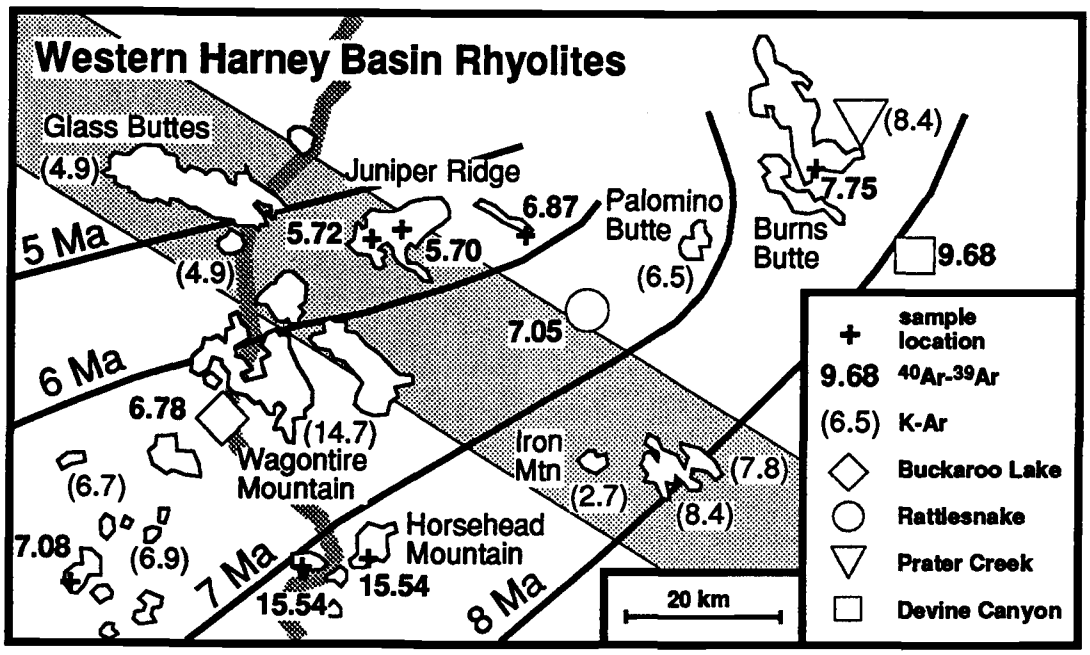

Figure 5.1: Locations and ages (in Ma) of rhyolite vent complexes dicussed in this chapter. Ages in bold print are from new $^{40}Ar/^{39}Ar$ data collected by Grunder and Deino (unpub. data, 1992); K-Ar ages and isochrons showing age progression of silicic domes are from MacLeod et al. (1975). Dark shaded line marks the western limit of Harney Basin (Walker, 1979). Light shaded band represents the axis of the Brothers fault zone. Ash-flow tuff vent locations were estimated from maps compiled by Greene (1972), Walker (1979) and Streck (1991), and include, from east to west, the Devine Canyon Tuff (9.68 Ma), the Prater Creek Tuff (8.4 Ma), the Rattlesnake Tuff (7.05 Ma), and the tuff of Buckaroo Lake (6.78 Ma).

orthopyroxene >> Fe-Ti oxides. There is no biotite in the porphyritic dacites and rhyolites, as was reported by Brown (1982).

5.1.2 Palomino Butte: Dated by K-Ar at 6.5 ± 0.3 Ma (K-Ar; Walker, 1974), Palomino Butte is a biotite-phyric rhyolite dome which lies geographically between Burns Butte and eastern Juniper Ridge. Two analyses of low-silica, metaluminous rhyolite (73.3 wt. % SiO_2) were obtained from Palomino Butte (Grunder, unpub. data).

5.1.3 Juniper Ridge: Juniper Ridge consists of two major suites of rocks, each with an independent petrogenetic history (Chapter 4). In previous geochronological studies (McKee and Walker, 1976), an aphyric rhyolite from the extreme eastern end of Juniper Ridge was dated by K-Ar at 5.7 ± 0.7 Ma and an age of 5.12 ± 0.08 Ma was obtained from a high-silica rhyolite at

western Juniper Ridge. New ^{40}Ar-^{39}Ar dating of the same units suggest that they are older (6.87 ± 0.02 and 5.72 ± 0.02 for eastern and western Juniper Ridge, respectively; section 3.1).

Two distinct rhyolite groups, designated as lower-silica and high-silica, are present at western Juniper Ridge. Both groups include aphyric and slightly porphyritic varieties. Lower-silica (75.0 to 75.3 wt. % SiO_2) rhyolite crops out in west-central Juniper Ridge as slightly porphyritic (alkali feldspar = plagioclase >> clinopyroxene) vesicular glass, and in western Juniper Ridge as dense, black, microlitic glass. High-silica rhyolites include slightly porphyritic vesicular glass (77.0 to 77.4 wt. % SiO_2; less than 1 % alkali feldspar > plagioclase > quartz > clinopyroxene) and aphyric black glass (77.3 to 77.4 wt. % SiO_2).

The eastern Juniper Ridge suite is exposed in the east-west striking scarp of the Juniper Ridge normal fault, ranges from primitive high-alumina olivine tholeiitic (HAOT) basalt to low-silica rhyolite, with relatively minor andesite, dacite and rhyodacite. The intermediate compositions evolved from the primitive basalt by removal of olivine, plagioclase and clinopyroxene in small, unconnected magma chambers (section 4.2.2). Rhyolites from eastern Juniper Ridge range from 72.3 to 73.7 wt. % SiO_2 and contain 0 to 15 % crystals of alkali feldspar > plagioclase > orthopyroxene > clinopyroxene > Fe-Ti oxide >> zircon (section 2.3.5).

5.1.4 Glass Buttes: The Glass Buttes complex consists of at least 10 separate vents that produced a range of rocks from rhyodacite to high-silica rhyolite (Cummings, 1985). Dates collected from Glass Buttes range from 5.8 ± 0.3 to 5.0 ± 0.8 Ma* (McKee and Walker, 1976; Roche, 1988) and generally define an east-west age progression that mimics that of the High Lava Plains as a whole, but poor resolution of the K-Ar age dates leaves this conclusion unconfirmed. According to Cummings (1984), the low-silica (70.8 to 75.9 wt. % SiO_2) rhyolites

*A previouly published age of 7.7 ± 0.4 Ma (Cummings, 1985) was obtained from a sample that had undergone hydrothermal alteration and is considered to be too old (Cummings, pers. comm. 1992).

and rhyodacites appear to post-date the high-silica (77.5 to 78.8 wt. % SiO_2) rhyolites. Unlike Juniper Ridge and Burns Butte, porphyritic Glass Buttes rhyolites contain hydrous phases, including hornblende and biotite, in addition to plagioclase, orthopyroxene and quartz (Roche, 1988).

5.1.5 Devine Canyon Tuff: The Devine Canyon Tuff is the oldest of at least three regionally extensive tuff sheets in the western Harney Basin (Walker, 1979). A range of K-Ar ages from 8.5 to 10 Ma have been reported by several different laboratories, but most K-Ar estimates cluster around 9.3 Ma (Walker, 1979). New ^{40}Ar-^{39}Ar dating places the tuff at 9.68 ± 0.03 Ma (Grunder and Deino, unpub. data).

Greene (1973) used isopach data and outcrop patterns to place the probable source area for the Devine Canyon Tuff about 10 km southeast of Burns Butte. Phenocrysts include alkali feldspar, quartz, and minor iron-rich pyroxene in abundances ranging from 1% lower in the tuff to 29% in the upper portions of the tuff (Greene, 1973).

5.1.6 Prater Creek Tuff: Occurrences of the Prater Creek Tuff are concentrated just east of Burns Butte, where the unit forms a distinct marker between ledges of Devine Canyon and Rattlesnake Tuff. An average of two K-Ar dates on the Prater Creek Tuff indicates an age of about 8.4 ± 0.7 Ma (Walker, 1979). In comparison to the Devine Canyon and Rattlesnake Tuffs, the Prater Creek Tuff is limited in extent and exceedingly crystal poor, with only trace alkali feldspar and quartz (Walker, 1979).

5.1.7 Rattlesnake Tuff: Although lack of a well-defined caldera and poor exposures in the central portion of the outcrop area make the vent area impossible to locate precisely, isopach data and facies distribution of the tuff suggest that the Rattlesnake Tuff erupted from somewhere between Silver Lake and Highway 395, putting it at about same longitude or slightly east of the eastern end of Juniper Ridge (Fig. 5.1; Streck, 1991). New ^{40}Ar-^{39}Ar data give a radiometric age on the tuff of 7.05 ± 0.02 Ma, intermediate between that of Burns Butte and Juniper Ridge, and slightly older than that of Palomino Butte. The Rattlesnake Tuff erupted from

a large magma chamber that was zoned from relatively high-silica rhyolite (up to 77.4 wt. % SiO_2) in the upper part of the chamber to slightly lower-silica rhyolite (down to 75.1 wt. % SiO_2) in the later-erupted, lower part (Streck and Grunder, 1991). In addition to mafic inclusions, the tuff also contains clasts of dacitic pumice which range in composition from about 62 to 67 wt. % SiO_2 (Streck, 1992).

5.1.8 Tuff of Buckaroo Lake: In outcrops south and southwest of Wagontire Mountain, the Rattlesnake Tuff is overlain by a thin vitric ash-flow tuff informally known as the tuff of Buckaroo Lake. Based on extensive field reconnaissance and trace element similarities, Streck (pers. comm. 1993) correlates the tuff of Buckaroo Lake with another tuff sheet that crops out to the west of Hampton Butte, previously known as the Hampton Tuff. A ^{40}Ar-^{39}Ar age of 6.78 ± 0.05 Ma on the tuff of Buckaroo Lake (Grunder and Deino, unpub. data) disagrees with a K-Ar age of 3.6 Ma on a tuff east of Hampton Butte (MacLeod et al., 1975), but because the tuffs are almost identical chemically, they are grouped here under the name Buckaroo Lake. Outcrop patterns of the tuff of Buckaroo Lake suggest a vent west of Wagontire Mountain (Fig. 5.1).

5.2 Trace element composition and regional geochemical variations

All high-silica rhyolites in the western Harney Basin can be classified as within-plate or A-type granitoids, according to the criteria of Pearce et al. (1984) and Whalen et al. (1987), respectively. Palomino Butte rhyolites, as well as some of the lower-silica rhyolites at Juniper Ridge, plot into the volcanic arc/syn-collisional and "other granite type" fields of Pearce et al. (1984) and Whalen et al. (1987), with respect to concentrations of Y, Nb, Yb and Ta. Eby (1990, 1992) divided the A-type granites into two series, one with trace element signatures resembling ocean island basalts (A_1) and the other resembling island arc basalts (A_2). Eastern Oregon rhyolites group with the A_2 variety, which Eby (1992) suggests were derived by crustal melting of

rocks from which a previous melt had been extracted, i.e. crust composed of continental arc or island arc rocks.

Rhyolite suites from the western Harney Basin plot along straight lines on an Y vs. Nb discriminant diagram (Fig. 5.2), with more evolved compositions plotting at successively higher Y and Nb. Y/Nb values for each suite increase systematically to the west, from about 1 at Burns Butte to about 4 at western Juniper Ridge, remaining relatively constant with evolution within each suite (Fig. 5.3). Ce/Yb, a measure of the steepness of the rare-earth element pattern, varies inversely with Y/Nb for the least-evolved rhyolites in each suite, and decreases regularly in each suite as degree of evolution increases. The envelope limiting the least-evolved tuffs defines a somewhat steeper trend than that delimiting the least evolved lavas (Fig. 5.3). Y/Nb and Ce/Yb for Palomino Butte (Y/Nb = 1.58 to 1.62; Ce/Yb = 16.9 to 17.0) and Iron Mountain (Y/Nb = 1.1; Ce/Yb = 25.7) correlate with position along the regional trend, but were omitted from Figures 5.2 to 5.5 to avoid cluttering the diagrams.

Neither age nor geographic position corresponds perfectly with Y/Nb, but the correlation with position is stronger. For one, Y/Nb ratios increase in the correct relative order with respect to position, but not with respect to age. Secondly, Iron Mountain, which is probably anomalously young with respect to the age-progressive trend (MacLeod, pers. comm. 1991; Grunder and Deino, unpub. data), has a Y/Nb ratio that correlates well with its location, implying that geographic position, rather than age, is an important control on Y/Nb.

Because trace element data commonly obtained by X-ray fluorescence are not available for Glass Buttes, chemical analogues for Y and Nb were tested in order to extend characterization of the trend past Juniper Ridge. As seen in Figure 5.4, Yb and Ta in the rhyolites vary in much the same manner as Y and Nb, producing similar clusters and arrays of data. Like Y/Nb, Yb/Ta ratios of the least evolved rhyolites decrease in younger/western rocks, but within-suite values are not as regular. At eastern and western Juniper Ridge and in tuff of Buckaroo Lake, for example, Yb/Ta increases slightly with evolution, but decreases with

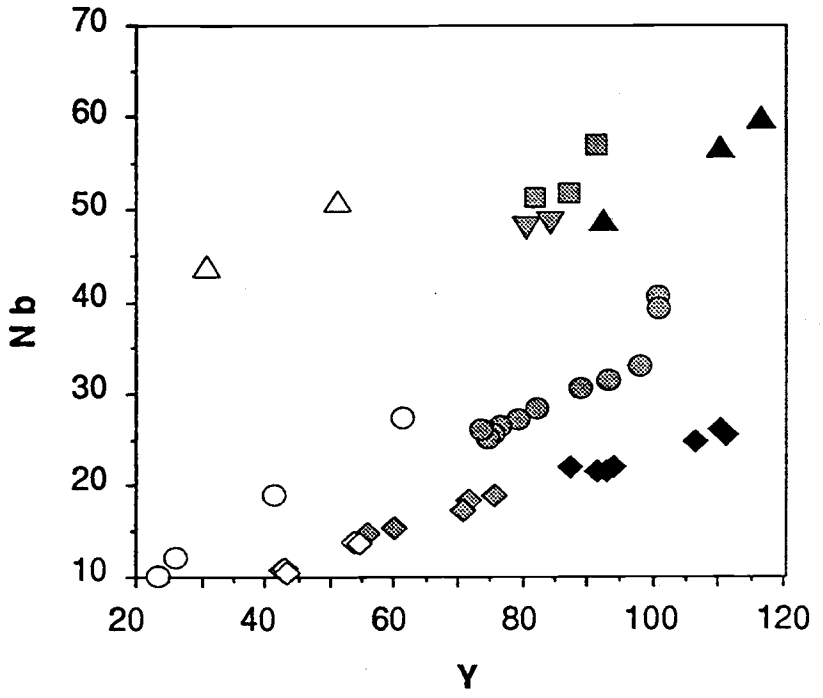

Figure 5.2: Y vs. Nb variation diagram for western Harney Basin rhyolites. Symbols as in Figure 5.3.

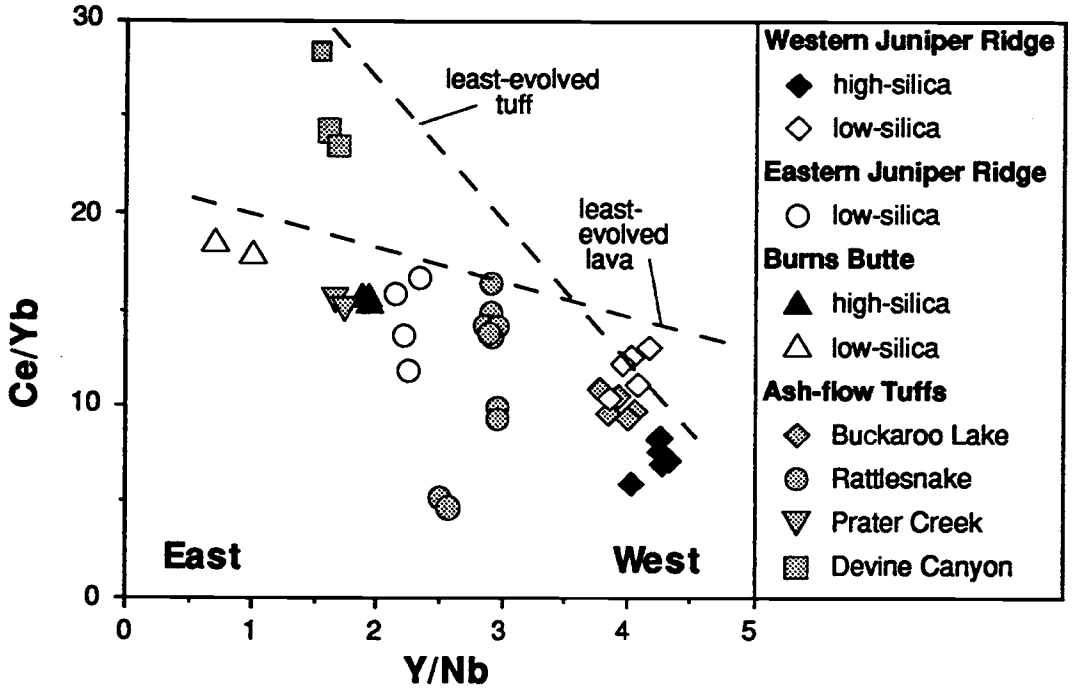

Figure 5.3: Y/Nb vs. Ce/Yb for western Harney Basin rhyolites, after Eby (1990). Dashed lines show inverse correllation of Y/Nb with steepness of rare-earth element (REE) pattern, as denoted by Ce/Yb. Y/Nb also correlates with age and geographical position, as discussed in text.

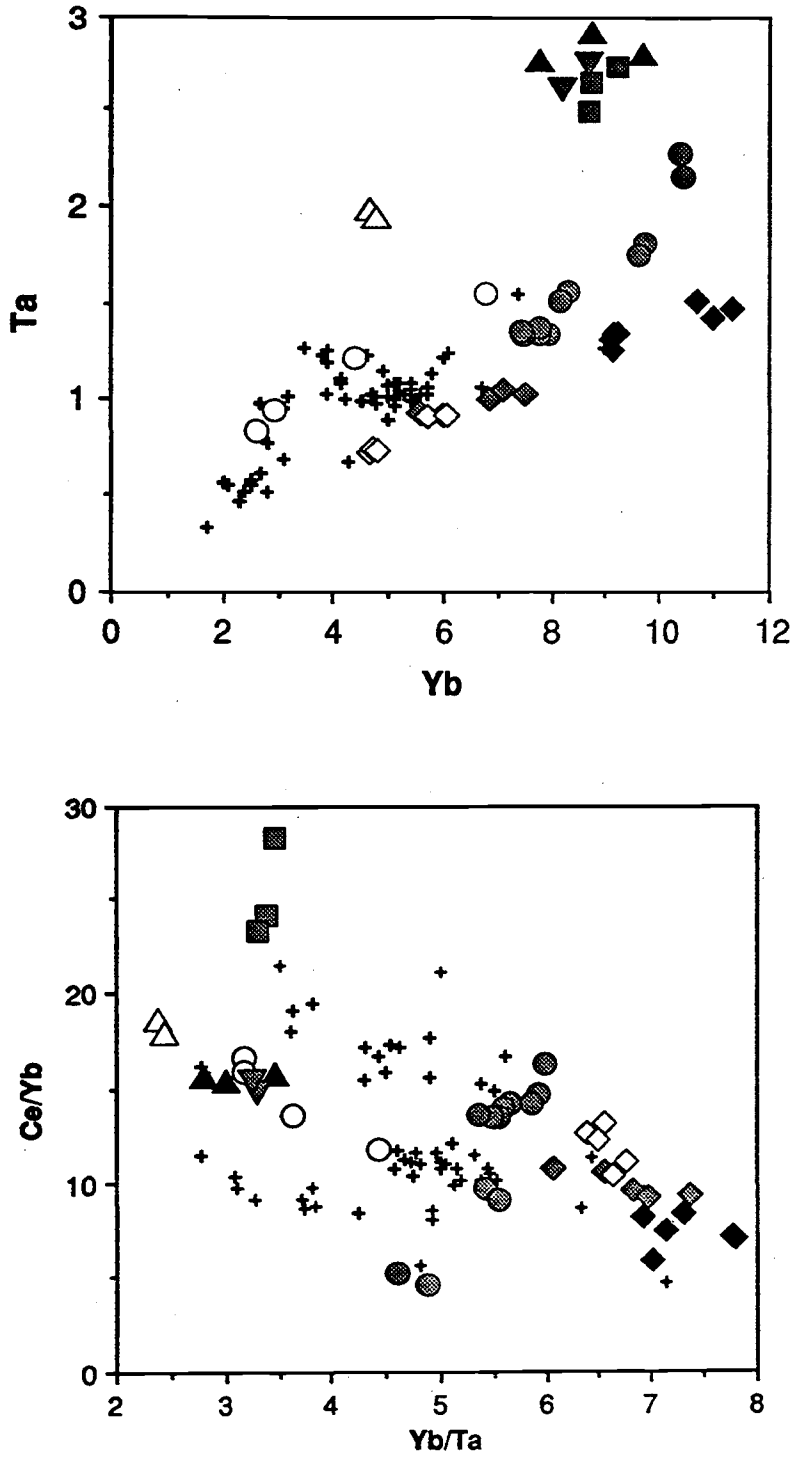

Figure 5.4: Yb vs. Ta and Yb/Ta vs. Ce/Yb for western Harney Basin rhyolites. Symbols as in Figure 5.3, except for the addition of Glass Buttes data (+).

evolution in the Rattlesnake Tuff. Yb/Ta in Glass Buttes rhyolites encompasses almost the entire range of Yb/Ta in the other suites combined.

In summary, systematic variation of Y/Nb, Ce/Yb, and Yb/Ta with geographic position is observed in the least-evolved rhyolites of western Harney Basin: Y/Nb and Yb/Ta are lower the east and increase to the west; Ce/Yb is higher to the east and decreases to the west. It is important to emphasize that due to the effects of within-suite differentiation, these variations apply mainly to the least-evolved rhyolites in each suite.

5.3 Petrogenetic implications for regional variations

Correlation of Y/Nb and other geochemical parameters of rhyolitic rocks with position in western Harney Basin is not exact, but is too strong to be accidental. It is important, therefore, to examine possible influences on Y/Nb, including the effects of crystal fractionation, contamination, and crustal melting, in each of the rhyolite suites. The discussion and conclusions are based in part on the model of rhyolite petrogenesis developed for Juniper Ridge (Chapter 4).

5.3.1 Crystal Fractionation: Examination of trace element behavior in each of the rhyolite suites suggests that separation of crystals from magma was not the controlling factor in establishing systematic differences in Y/Nb ratios along the trend.

Figure 5.5 shows the influence of various mineral phases on the trace element chemistry of rhyolitic rocks as a result of crystal fractionation. For example, Sr/Rb is used as a tracer for removal of plagioclase feldspar. With evolution, Sr/Rb decreases at eastern and western Juniper Ridge, in the Rattlesnake Tuff and in the tuff of Buckaroo Lake, the magnitude of the decrease corresponding to the proportion of plagioclase in the fractionation assemblage. Similarly, decreasing Ba/Rb is a signature for removal of alkali feldspar, Sc/Y for clinopyroxene and Zr/Y for zircon. Except in tight data clusters, where analytical uncertainty exceeds variation,

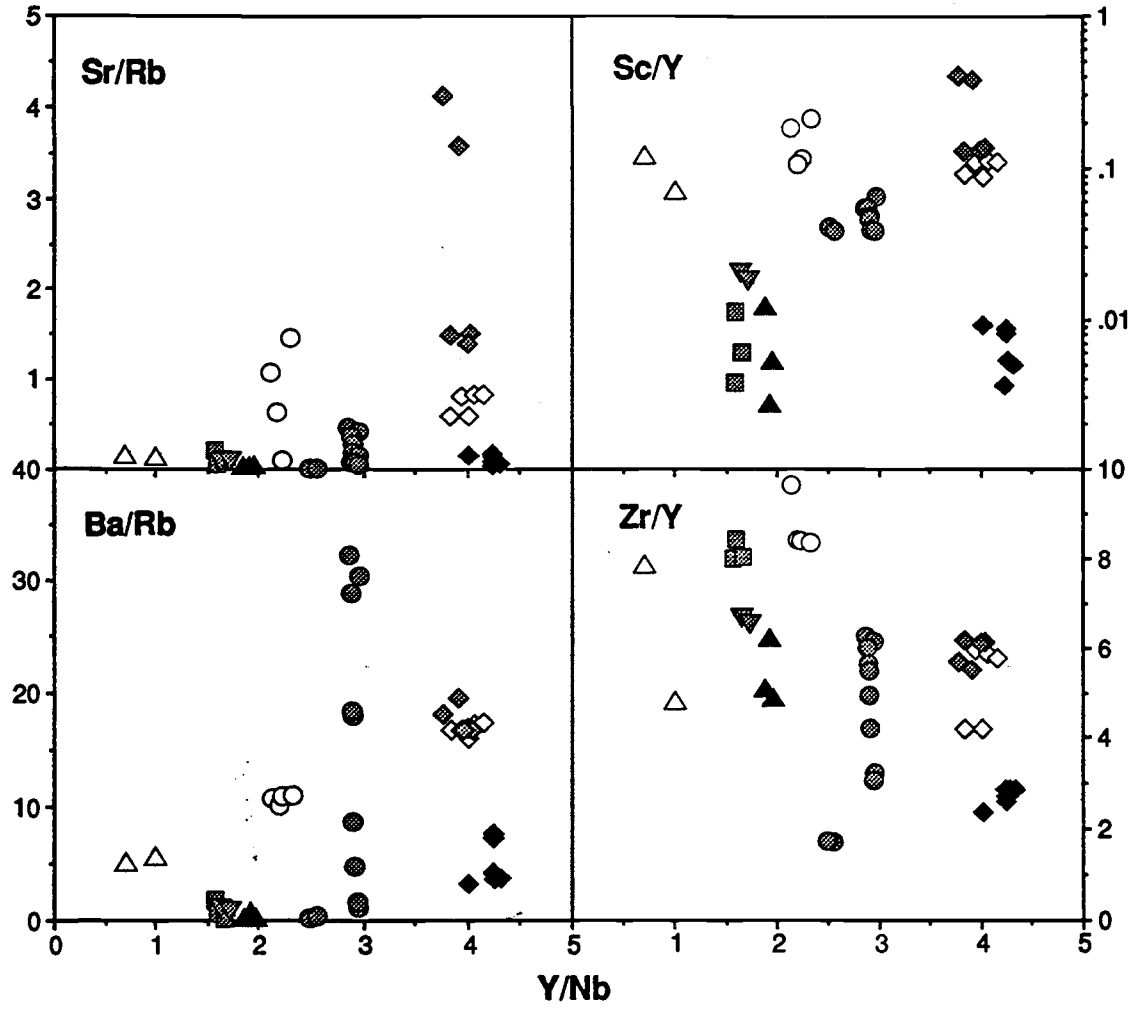

Figure 5.5: Effects of the removal of various minerals during evolution of rhyolite suites, as illustrated by decreasing Sr/Rb (plagioclase), Ba/Rb (alkali feldspar), Sc/Y (clinopyroxene), and Zr/Y (zircon) with evolution within each suite. Symbols as in Figure 5.3.

relative position of each of the data points in each suite is constant, supporting the possibility that rocks in each suite are related by crystal fractionation.

Rhyolite suites in western Harney Basin experienced differences in both degree of fractionation and mineral assemblage, but these differences are not systematic with position and thus cannot account for systematic changes in Y/Nb. The only observed mineral phase capable of fractionating Y from Nb based on differences in partition coefficients is clinopyroxene. All suites seem to have experienced at least some clinopyroxene fractionation, but its abundance in the fractionated mineral assemblage appears to have been small enough that the effect on Y/Nb is negligible (c.f. Eby, 1990).

Y/Nb may change during evolution of a magma by removal of amphibole or biotite from rhyolitic melts, since these phases have significantly different partition coefficients for Y and Nb (Pearce and Norry, 1979; Nash and Crecraft, 1985). By analogy to Y and Nb, Yb and Ta may have been affected by removal of biotite and amphibole during evolution at Glass Buttes, which does not fit the geochemical trend with respect to its position. Biotite and hornblende have opposite effects on Yb/Ta ($Kd_{Yb/Ta}^{biotite} < 1$; Nash and Crecraft, 1985; $Kd_{Yb/Ta}^{amphibole} > 1$; Henderson, 1982), perhaps explaining the large degree of scatter observed in Yb/Ta at Glass Buttes (Fig. 5.4).

Only the most-evolved Rattlesnake Tuff experienced a change in Y/Nb during evolution, possibly due to removal of allanite (again assuming that Yb/Ta is analogous to Y/Nb; Table 5.1). Allanite fractionation in the most-evolved Rattlesnake tuff is indicated by extreme depletion in LREE (c.f. Miller and Mittlefehlt, 1982).

5.3.2 Contamination: Contamination of rhyolitic magma with partial melts of garnet, apatite, amphibole, biotite and/or clinopyroxene-bearing wall-rocks is another method by which Y/Nb can potentially be affected. Garnet and apatite would have the greatest effect, because of extremely high partition coefficients for Y in both phases ($Kd_Y^{garnet} = 35$, $Kd_Y^{apatite} = 40$; Pearce and Norry, 1979). This process is considered unlikely because probable wall-rock

lithologies (i.e. amphibolite) have low Y and Nb compared to silicic magma compositions, requiring unreasonably high degrees of contamination in order to affect Y/Nb.

5.3.3 Crustal melting: Using the petrogenetic model for Juniper Ridge as an example, the least-evolved rhyolites in each suite can be considered to be crustal melts from which the rest of the rhyolites evolved by crystal fractionation. Changes in degree of partial melting with either amphibole, clinopyroxene, or garnet in the melt residuum can change Y/Nb ratios in partial melts. These are phases that are likely to be present in an amphibolite lower crust and which have significantly different partition coefficients for Y and Nb, as well as for Ce/Yb and Yb/Ta (Table 5.1).

Because of its high partition coefficient for Y and correspondingly low partition coefficient for Nb, garnet would have the most drastic effect, whereby significant differences in Y/Nb could be generated with only modest differences in degree of melting. These differences would be largest at small degrees of partial melting, and would decrease as the melt fraction increases (Fig. 5.6). Specifically, high concentrations of Nb in early melts would produce low Y/Nb ratios. Nb decreases rapidly in successive melts while Y is relatively constant, thus, Y/Nb increases with increasing degree of melting. Available partitioning data (Table 5.1) suggest that other trace element variations seen in the western Harney Basin rhyolites can also be explained by greater degrees of partial melting from east to west. Systematic decrease in Ce/Yb and increase in Yb/Ta in the least evolved rhyolites is compatible with such a scenario, because garnet, amphibole and clinopyroxene all have high $Kd_{HREE/LREE}$ and $Kd_{Yb/Ta}$, so that greater degrees of melting would result in lower Ce/Yb and higher Yb/Ta to the west.

5.3.4 Discussion: Changes in degree of partial melting as the dominant control on trace element variation in western Harney Basin rhyolites is favored for several reasons. First, no evidence exists to support differences in crustal lithology as a factor. The crustal structure studies of Catchings and Mooney (1988) show a slight deepening of the crust-mantle boundary to the east, but no marked lateral discontinuities that would indicate a progressive change in

TABLE 5.1: Rhyolite Partition Coefficients and Coefficient Ratios

	KdY	KdNb	KdYb	KdTa	KdCe	KdY/Nb	KdYb/Ta	KdCe/Yb
amphibole	6	4	9	0.3	2	1.5	30	0.2
clinopyroxene	4	0.8	11.6	0.57	2.9	5	20	0.25
garnet	35	0.02*	40*	0.06*	0.1	1750	666	0.003
zircon	n.a	n.a.	225	4.8	2.4	n.a.	47	0.01
allanite	n.a.	n.a.	22	3.2	1279	n.a.	6.9	58

Some partition coeffients for garnet (*) are for basaltic or andesitic liquids. For rhyolitic liquids, KdYb is probably higher; KdNb and KdCe may be lower. Partitioning data is from Pearce and Norry (1979), Nicholls and Harris (1980), Henderson (1982), Nash and Crecraft (1985), Green and Pearson (1985), and Sawka (1988).

lithology along the transect. Instead, isotopic studies indicate that the crust beneath southeastern Oregon is remarkably uniform. Initial strontium isotopic ratios for rhyolites west of the Idaho border are on the order of 0.704 (Wilson et al., 1983; Hart, 1984), similar to the isotopic ratios of the regional basalts.

Second, systematic variations in trace elements can be explained by adapting the petrogenetic model developed for rhyolites at Juniper Ridge. As discussed in section 4.3.1, amphibolite is a likely source rock for crustal melting, as suggested by experimental melting of similar rocks, by the isotopic composition of the rhyolites (Carlson and Hart, 1987), and because amphibolite is probably present in the lower crust (Catchings and Mooney, 1988). The presence of garnet and/or pyroxene in the melt residuum can affect variations in Y/Nb, and in other trace element parameters, including Ce/Yb and Yb/Ta.

Lastly, the connection between extension, mafic magmatism and crustal melting is well-established (Hildreth, 1981), and provides a ready explanation for variation in degree of melting. The geographical trend of rocks studied in this chapter is almost east-west, slightly oblique to the northwest-trending axis of the Brothers fault zone (Fig. 5.1). Extensional faulting near the Brothers fault zone may have produced conduits for mafic magma, which in turn promoted crustal melting in proportion to the amount of mafic input to the crust. Degree of extensional faulting probably correlates with the volume of silicic volcanism, as seems to be the case at Juniper Ridge, where a thick pile rhyolite lavas to the west are dissected by many faults, and

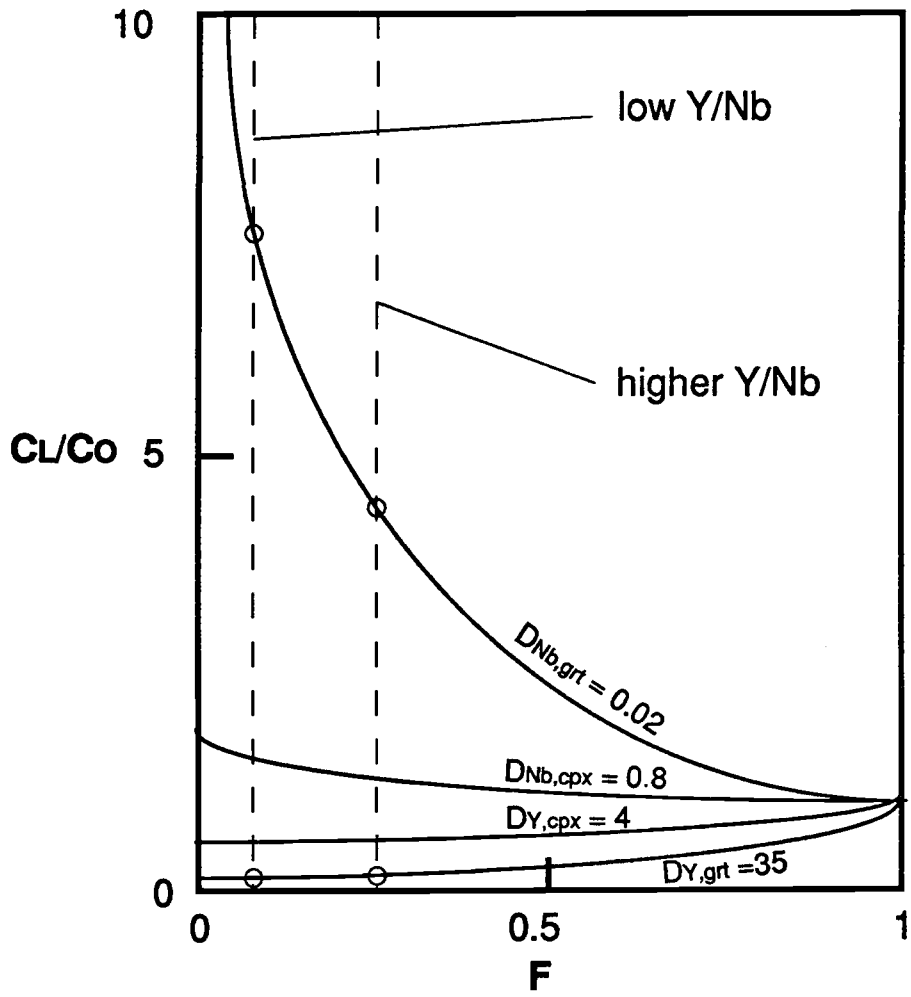

Figure 5.6: Variation in concentration of trace elements with progressive equilibrium melting (after Cox et al, 1979). C_L = concentration of an element in the liquid (melt). C_O = concentration of an element in the resiuum (mineral). F = fraction of melt. Initial melts (F = O) are enriched in incompatible elements and become less enriched in subsequent melt fractions. For highly incompatible elements such as Nb in garnet (shown), small differences in degree of melting (F) can result in substantial differences in trace element composition of the melt.

much lower volumes of rhyolite are exposed in the relatively unfaulted eastern part. Alternatively, changes in degree of melting may be tied to progressively greater extension with time along the Brothers fault zone. Although no data exists on the timing of faulting on the Brothers fault zone, faulting and volcanism in the Great Basin are inextricably linked (Gans et al., 1989; Seedorff, 1991).

5.4 Conclusions

Trace element ratios for age-progressive rhyolites in the western Harney Basin vary systematically with position, and consequently with age. Y/Nb and Yb/Ta increase from east to west for rhyolites in each of seven volcanic suites, including dome complexes and ash-flow tuffs. Concurrently, Ce/Yb decreases from east to west for the least-evolved rhyolite of each suite. The correlation of chemical variation with age is considered secondary to the correlation with position, because anomalously young rhyolites at Iron Mountain have chemical signatures appropriate to their position along the High Lava Plains rather than to their age.

Variations of Ba/Sr, Rb/Sr, Sc/Y and Zr/Y at fixed Y/Nb show that alkali feldspar, plagioclase, pyroxene and zircon, respectively, played important but variable roles as fractionates in all suites, but only the most-evolved portions of the Rattlesnake Tuff show evidence that fractionation altered Y/Nb. Y/Nb ratios were imparted to the least evolved rhyolite at each suite, namely the crustal melt from which each suite evolved, and must have been imparted at the source. Systematic variations in crustal lithology are considered unlikely because of isotopic homogeneity and lack of lateral discontinuities in crustal structure. Therefore, progressive change in degree of melting in the source regions of the silicic melts is preferred. The hypothesis that changes in degree of melting could have produced the observed elemental variations is supported by trace element partitioning behavior for the above elements in garnet, clinopyroxene, and amphibole, all of which are likely to be in a partially melted amphibolitic lower crust.

Since variation in degree of melting is related to amount of crustal extension and heat input from the mantle in the form of basalts, trace element chemistry is potentially related to the timing and degree of extension along the High Lava Plains. Changes in degree of melting with position could have been due to progressive extension along the Brothers Fault zone, which is the dominant structural feature on the High Lava Plain and generally parallels the age-progressive trend (Lawrence, 1976), or to distance from the axis of the Brothers fault zone.

5.5 Hotspot versus continental rifting revisited

This thesis documents petrologic processes in a series of rhyolites that erupted on the northern boundary of a major extensional province, the Great Basin of the western United States. Assuming that rhyolites at Juniper Ridge are representative of other rhyolites in the northern Great Basin, as the trace element data in this chapter suggests, melting in response to crustal extension is the primary way in which rhyolites are formed along the High Lava Plains province and its counterpart to the east, the Snake River Plain.

The close link between extension and melting is the basis for preferring a rifting model over a hotspot model for the generation of age progressive rhyolites on the High Lava Plains as well as on the Snake River Plain. Although the hotspot theory cannot be entirely ruled out on the basis of available data, a progressive rifting model by itself can explain almost every aspect of late Cenozoic volcanism in the northern Great Basin while a hotspot model cannot. Lack of age progression in the basalts, symmetry of the age-progression and the links between volcanism and faulting are just three characteristics that cannot be accounted for by a hotspot. Conversely, greater volumes of rhyolitic (but not basaltic) volcanism on the Snake River Plain as compared to the High Lava Plains may be the only characteristic better accounted for by a fixed melting anomaly in the mantle below Yellowstone.

CHAPTER SIX: GEOLOGY AND GEOCHEMISTRY OF HORSEHEAD MOUNTAIN

Horsehead Mountain lavas consist of calc-alkaline andesites and dacites that are associated in time and space with the pulse of magmatism that produced the Steens and Columbia River flood basalts, along with several smaller basaltic to intermediate vent complexes, from about 15 to 17 Ma. These lavas predate the HAOTs and age progressive rhyolites that erupted in later Miocene time, and probably represent inception of the latest episode of rifting and extension in the northern Great Basin.

6.1 Age, Field Relationships, and Petrography

Horsehead Mountain was dated by ^{40}Ar-^{39}Ar at 15.54 ± 0.03 Ma (Table 6.1) and is thus one of several dome complexes on the High Lava Plains that predate the age-progressive trend of the later Miocene silicic rocks. Little Juniper Mountain, located about 5 km southwest of Horsehead Mountain, has an identical isotopic age (15.54 ± 0.05 Ma; Grunder, unpub. data) and similar chemical composition. Both Horsehead Mountain and Little Juniper Mountain are overlain by the Rattlesnake Ash-flow Tuff (7.05 Ma), a regionally extensive unit that serves as a marker bed for southeastern Oregon stratigraphy (Walker, 1979).

At the Horsehead Mountain volcanic complex, andesitic to rhyodacitic lavas and tuffs erupted from at least six vents, which are crudely aligned to the northeast (Plate II). Contact relations between flow units from different vents indicate a general decrease in age to the northeast. At each vent, crystal-poor dacite and andesite (Td) flows are intercalated with relatively crystal-rich dacite and rhyodacite (Trd), however, crystal-rich dacite and rhyodacite is the last-erupted rock type at each vent. Lithic, pumiceous ash-flow tuff (Tp) occurs at the base of several crystal-rich lavas, and is texturally gradational with welded volcanic breccia that formed a carapace around crystal-rich lava flows. Occasional dikes and flows of aphanitic andesite (Ta) occur at several of the Horsehead Mountain vents.

Field characteristics and general petrographic descriptions of the map units at Horsehead Mountain follow in general order of youngest to oldest. Detailed petrographic descriptions of Horsehead Mountain rocks are in Appendix 2.

6.1.1 Hampton Tuff (Tuff of Buckaroo Lake): Outcrops of grey-brown, poorly welded tuff occur in the northwest corner of the map area and are probably correlative with a tuff or series of tuffs known informally as the Hampton tuff or tuff of Buckaroo Lake. Correlation of the Hampton tuff, exposed just west of Hampton Butte, and the tuff of Buckaroo Lake, exposed along Highway 395 south of the town of Wagontire and at Wagontire Mountain, is based on

TABLE 6.1: ^{40}Ar-^{39}Ar Analytical Data for Horsehead Mountain Sample

Lab ID#	Ca/K	$^{36}Ar/^{39}Ar$	$^{40}Ar^*/^{39}Ar$	$\%^{40}Ar^*$	Age (Ma) ±1σ
Sample HP-91-14					
Sanidine					
5360-05	0.023	0.00010	1.732	97.1	15.51 ± 0.04
5360-01	0.027	0.00006	1.734	97.9	15.53 ± 0.04
5361-01	0.061	0.00012	1.735	96.9	15.54 ± 0.04
5360-06	0.022	0.00030	1.735	94.1	15.54 ± 0.04
5361-06	0.024	0.00008	1.737	97.4	15.55 ± 0.04
5361-08	0.023	0.00008	1.737	97.6	15.56 ± 0.04
			Weighted average =		15.54 ± 0.03
Plagioclase					
5361-09	5.959	0.00172	1.667	84.8	14.93 ± 0.22
5361-04	5.369	0.00137	1.689	88.6	15.13 ± 0.14
5360-04	4.327	0.00117	1.709	89.6	15.31 ± 0.10
5361-07	4.682	0.00208	1.714	79.1	15.35 ± 0.16
5361-03	3.414	0.00090	1.727	91.8	15.47 ± 0.12
5361-05	5.122	0.00129	1.729	89.4	15.48 ± 0.13
5360-03	4.808	0.00122	1.750	90.0	15.68 ± 0.11
5360-02	7.625	0.00512	1.763	58.7	15.79 ± 0.19
5361-02	4.734	0.00104	1.779	92.4	15.94 ± 0.14
			Weighted average =		15.47 ± 0.09

Notes: Errors in age quoted for individual runs are 1σ analytical uncertainty. Weighted averages are calculated using the inverse variance as the weighting factor (Taylor, 1982), while errors in the weighted averages are 1σ standard error of the mean and incorporate error in J (see below) (Samson and Alexander, 1987). Ca/K is calculated from $^{37}Ar/^{39}Ar$ using a multiplier of 1.96. $^{40}Ar^*$ refers to radiogenic argon. $\lambda = 5.543 \times 10^{-10}\ y^{-1}$. Isotopic interference corrections: $(^{36}Ar/^{37}Ar)_{Ca} = (2.58 \pm 0.06) \times 10^{-4}$, $(^{39}Ar/^{37}Ar)_{Ca} = (6.7 \pm 0.3) \times 10^{-4}$, $(^{40}Ar/^{39}Ar)_K = (2.19 \pm 0.02) \times 10^{-2}$. $J = (4.986 \pm 0.010) \times 10^{-3}$.

similarity in composition and age (Streck, pers. comm, 1993). At other localities to the west and northwest of Horsehead Mountain, the tuff overlies Rattlesnake Tuff, but at Horsehead Mountain, contact relationships are indeterminate.

In addition to 5 to 10 percent sanidine, plagioclase and trace mafic phenocrysts, the tuff contains about 10 percent white pumice fragments and about 5 percent angular lithic and glass fragments in a fine-grained, grey-brown tuffaceous matrix.

6.1.2 Rattlesnake Ash-flow Tuff (Trt): Brown, pockmarked, moderately to slightly welded Rattlesnake Tuff with abundant silky pumice fragments occurs at the foot of the southwestern slope of Horsehead Mountain, and along the west, southeast, and east margins of the complex (Plate II). It is identified by a characteristic assemblage of black, white, and mixed pumice, minor rounded lithic fragments, and less than a percent crystal fragments. Along the northern margin of the complex, black rheomorphic tuff with white bands and pink to gray pumiceous tuff containing sparse white and grey pumice in a pink ash matrix have also been identified as Rattlesnake Tuff (Streck, pers. comm., 1992). Therefore, Rattlesnake Tuff surrounds the Horsehead Mountain complex on nearly all sides, but field relations between the Rattlesnake Tuff and lavas of the Horsehead Mountain complex are unclear. In several locations, the Rattlesnake Tuff appears to overlap ridges that at higher elevations are composed of rhyodacite lava, but the two lithologies are never in direct contact. ^{40}Ar-^{39}Ar age dating confirms the inference that the Rattlesnake Tuff is younger.

6.1.3 Crystal-rich rhyodacite and dacite (Trd): Crystal-rich lava is commonly the last or only rock type erupted from Horsehead Mountain vents. Outcrops of crystal-rich rhyodacite and dacite are blocky or jumbled, and range in appearance from massive, black vitrophyre to banded or streaky, brick red oxidized glass to stony, pinkish grey, fully devitrified lava. Devitrification usually increases inward from inferred flow margins and inward toward the cores of younger domes. Approximately 0.5 to 2 m of dense black vitrophyre overlies volcanic breccia in many crystal-rich flows and grades abruptly upward into devitrified lava.

Foliation in crystal-rich rhyodacite flows is commonly defined by bands of oxidized or differentially devitrified glass, by jointing, or by zones of tension gashes, which occur in narrow (1 to 3 cm) bands parallel to the flow direction. At several inferred vent locations, flow banding and platy jointing (10 to 20 cm thick) of devitrified rhyodacite is concentric and inwardly dipping, while younger, glassier flows dip away from the vent. Rounded, glassy blocks commonly rest on an erosional surface of massive, devitrified, flow-banded lava.

Crystal-rich rhyodacite commonly contains as much as 20 to 30% fine-grained, oxidized or devitrified inclusions that range in size from less than 0.5 cm to as much as 1 m, though most range between 5 and 10 cm in diameter. Larger and more abundant inclusions occur nearer to inferred vent locations. The inclusions commonly have air pockets at their lateral margins, as well as layers of elongate minerals and flow foliation bending around them, indicating that they were solid bodies at the time of eruption. Other inclusion types include white to greenish yellow or tan, weathered inclusions.

Dikes and irregular intrusions of crystal-rich rhyodacite cut both crystal-poor lava and volcanic breccia. One 3 to 5 meter thick dike, on the west flank of the Horsehead Mountain complex, can be traced upward to a moderately crystal-rich rhyodacite lava flow. Small felsic dikes also intrude crystal-poor lavas and are usually light in color, vesicular, with 0.5 to 1 cm thick dark, glassy chilled margins.

Phenocrysts in Trd include mainly plagioclase, pyroxenes and oxides, with minor alkali feldspar and rare (xenocrystic?) amphibole. Large (1 to 10 cm) sieved plagioclase, occuring in glomerocrysts with pyroxene, is the most abundant and most characteristic phenocryst phase in crystal-rich (Trd) lavas, where it can reach up to 20% of the mode. Subordinate feldspar textures include euhedral, elongate laths and subhedral grains with finely sieved margins. Pyroxene content is variable; crystal-rich lavas can contain up to about 8% pleochroic light green to tan biaxial (-) clinopyroxene, light green biaxial (+) orthopyroxene, or both. Embayed or rounded, equant oxide minerals (2 to 6%) in crystal-rich lavas range up to 0.4 mm in

diameter. Some crystal-rich lavas contain up to 5% untwinned alkali feldspar with feathery margins consisting of thin subparallel growths that are perpendicular to the grain margins. Glassy groundmass for Trd and Td consists of up to 70% brown glass, microlitic colorless glass, or intricate interfingerings of both (Appendix 2).

6.1.4 Crystal-poor rhyodacite and dacite (Td): In the northern part of the Horsehead Mountain complex, the oldest exposed rock type is black, crystal-poor, hydrated to partially devitrified dacite and rhyodacite that has a hackly, finely jointed (1 to 3 cm) appearance in outcrop. In general, crystal-poor dacites and rhyodacites are more mafic than crystal-rich rhyodacites, though there is considerable compositional overlap between the two textural types. Where both are exposed near the same vent area, crystal-poor lavas underlie relatively crystal-rich lavas or are intruded by them. Crystal-poor lavas seem to be hydrated rather than devitrified, and are occasionally brecciated. With the exception of fewer crystals, they are petrographically identical to crystal-rich lavas at Horsehead Mountain (Trd), containing the same minerals in roughly the same proportions.

6.1.5 Andesite (Ta): Rocks of andesitic composition, exhibiting textural and mineralogical differences from the rest of Horsehead Mountain rocks, occur at two locations in the map area (Plate I). An outcrop in the southwestern portion of the map area consists of sparsely phyric to aphyric brown to black andesite with angular, stretched out vesicles with nearly vertical foliation, while adjacent rhyodacitic carapace breccia to the north and south of the andesite dips gently to the north. Though contact relations are unclear, it appears that the andesite may be a shallow dike. An aphyric, vesicular andesite flow is the lowest flow in the series of flows that makes up the northern half of the map area (Plate II).

Andesite flows contain less than 3% plagioclase, 0 to 1% pyroxene (including both clinopyroxene and orthopyroxene), and less than 1% oxide minerals, usually enclosed in a felty, trachytoid groundmass, or in blotchy, partially devitrified glass. Plagioclase exhibits a multitude

of textures (Appendix 2), but none of the large, sieved grains that characterize other Horsehead Mountain lavas.

6.1.6 Pyroclastic deposits (Tp): Thin (3 to 20 m) beds of lithic-rich pumiceous tuff underlie crystal-rich rhyodacite lavas, or are interbedded within flows of crystal-poor lava. Tuff beds are unwelded, range from white to buff in color, and consist of black, white or light grey pumice fragments, angular, glassy volcanic rock fragments (up to 15 cm across), and light grey to white fine-grained ash. Rock fragments range from 20 to 30% in abundance and contain glomerophyric and skeletal plagioclase phenocrysts that are identical to those found in rhyodacite lava flows. Less abundant rock fragments include crystal-poor dacite and devitrified rhyodacite. Ash content varies from about 10% to over 50% in different exposures, which may represent several different ash-flow tuffs, or different facies of the same tuff.

Crudely bedded (0.25-3m), unwelded to strongly welded volcanic breccia occurs near the base of most crystal-rich rhyodacite flows. Beds of breccia are often folded and banked against pre-existing topography. Breccia (denoted by an "x" pattern on Plate II) consists of fragments of dense vitrophyre, and finely pumiceous black glass in a matrix of dark gray vesicular glass or ash, all containing sparse white plagioclase and acicular clinopyroxene phenocrysts. This unit is probably an autobrecciated vesicular carapace that formed an envelope around crystal-rich rhyodacite flows, based on homolithologic clast composition, texture, and gradational contacts with glassy rhyodacite flows. Basal carapace breccia is strongly welded, and in several locations occurs as stretched and flattened black glass (resembling fiammi) in a matrix of orange, oxidized ash or vesicular glass. Volcanic carapace breccia is texturally gradational into tuffaceous breccia and ash-flow tuff, with increasing amounts of ash in the matrix, suggesting that small, explosive, ash-flow eruptions, perhaps produced by collapse of flow margins, accompanied extrusion of rhyodacite flows.

6.2 Composition of Horsehead Mountain Lavas

Using the analytical methods outlined in Chapter 3 (section 3.3.1), whole rock major- and trace-element compositions were determined for fifteen Horsehead Mountain rocks, including samples from each map unit and vent location (Table 6.1). Trace element compositions by INAA were also performed on five glass separates at the OSU Radiation Center (Table 6.2).

Horsehead Mountain lavas form a compositionally limited, coherent suite that ranges from silicic andesite to rhyodacite with no significant data gaps (Fig. 6.1). By the classification of Irvine and Baragar (1971) the rocks are subalkaline, tholeiitic, K-poor andesites and sodic dacites; the scheme of LeBas (1986) classifies them as trachyandesites and trachydacites.

In comparison to whole-rock compositions, Horsehead Mountain glass is slightly LREE-enriched and HREE-depleted (Fig. 6.2) and has a slightly larger Eu anomaly. Despite their evolved compositions with respect to contemporaneous Steen's basalts, Horsehead Mountain lavas have REE patterns that are nearly identical to Steen's compositions (Fig. 6.2).

6.3 Discussion and future work

Miocene intermediate rocks with calc-alkaline affinity have been documented elsewhere in eastern Oregon, but are scarce and relatively unstudied. Robyn (1979) notes porphyritic dacite at Strawberry Mountain, one of three late Miocene hypersthene andesite centers, also including Sawtooth Crater and Dry Mountain, arranged along a northeast-southwest linear trend in eastern Oregon. Interestingly, Horsehead Mountain and Little Juniper Mountain lie directly on the southwestern projection of the trend. Bailey (1992) studied a compositionally diverse suite at the Powder River volcanic field in northeastern Oregon, including 12-14 Ma calc-alkaline andesite and dacite along with high-silica rhyolite, olivine tholeiite and alkali basalt, all of which post-date

TABLE 6.2: Whole-rock compositions of Horsehead Mountain samples

sample #	JM-91-5	JM-91-6	HH-91-8	HH-91-11	HH-91-14	HH-91-15
map unit	Trd	Trd	Trd	Trd	Trd	Td
XRF analyses (wt. %)						
SiO_2	68.1	68.3	67.2	67.7	67.3	64.6
TiO_2	0.49	0.49	0.60	0.57	0.61	0.80
Al_2O_3	15.02	15.07	15.04	14.94	15.04	15.95
$Fe_2O_3^*$	4.54	4.52	5.19	5.02	5.00	5.96
MnO	0.10	0.10	0.12	0.12	0.11	0.10
MgO	0.69	0.64	0.84	0.77	0.89	1.01
CaO	2.48	2.55	2.72	2.69	2.79	3.52
Na_2O	4.14	3.82	4.08	4.02	3.93	4.51
K_2O	4.22	4.32	3.95	3.99	4.08	3.26
P_2O_5	0.19	0.20	0.23	0.22	0.20	0.29
Total	99.79	99.82	99.71	99.68	99.41	99.68
XRF analyses (ppm)						
V	17	18	24	20	36	34
Ni	7	7	8	6	7	7
Cu	7.8	12.8	12.7	18.5	15.2	17.3
Zn	82	82	92	91	82	97
Ga	18	19	19	18	19	19
Rb	101	98	95	96	99	94
Sr	191	206	198	199	193	243
Ba	1159	1558	1105	1121	1074	1056
Y	41	38	42	43	40	45
Zr	285	277	274	272	273	273
Nb	22.7	22.9	22.2	22.9	22.5	22.7
Pb	15	14	16	17	16	12
INAA analyses (ppm)						
Sc	8.1		9.5	9.0	9.4	11.0
Cr	2		3	3	3	n.d.
Co	4.9		6.1	6.0	6.4	8.1
Cs	3.9		3.9	3.9	4.3	2.7
As	4.6		5.3	4.9	3.3	n.d.
Sb	0.9		0.9	1.0	0.9	0.4
Se	2.2		2.3	2.0	n.d.	1.8
La	30.1		29.0	31.9	28.7	29.0
Ce	63		62	61	60	63
Nd	29		30	30	30	30
Sm	7.41		7.68	7.94	7.41	8.05
Eu	1.60		1.74	1.70	1.60	1.74
Tb	1.11		1.16	1.18	1.18	1.24
Yb	3.9		4.1	4.3	4.2	4.2
Lu	0.60		0.61	0.62	0.58	0.64
Hf	7.3		7.6	7.3	7.5	6.8
Ta	1.5		1.5	1.5	1.5	1.5
Th	8.7		9.2	8.5	9.4	7.8
U	3.4		3.7	3.2	3.8	3.4

Analytical information and precision as in Table 3.6.

TABLE 6.2 (continued)

sample #	HH-91-18	HH-91-20	HH-91-21	HH-91-25	HH-91-32	HH-91-33
map unit	Trd	Trd	Trd	Trd	Ta	Td
XRF analyses (wt. %)						
SiO_2	67.4	66.2	67.5	65.2	64.2	63.6
TiO_2	0.58	0.71	0.56	0.88	0.93	0.97
Al_2O_3	15.02	15.32	15.11	15.68	15.87	15.83
$Fe_2O_3^*$	5.03	5.39	4.80	6.17	6.29	6.51
MnO	0.10	0.12	0.10	0.10	0.11	0.13
MgO	0.86	1.05	0.80	0.75	1.18	1.31
CaO	2.75	3.14	2.66	3.40	3.76	3.92
Na_2O	4.18	3.87	3.83	4.29	4.28	4.15
K_2O	3.85	3.97	4.42	3.29	3.10	3.33
P_2O_5	0.20	0.23	0.20	0.26	0.29	0.29
Total	99.52	99.70	99.88	99.85	99.80	100.29
XRF analyses (ppm)						
V	29	37	26	58	57	65
Ni	7	8	6	8	8	9
Cu	10.4	15.8	11.3	21	21	21.5
Zn	85	87	83	93	98	94
Ga	19	19	19	19	20	20
Rb	98	98	99	92	90	87
Sr	197	213	195	226	241	240
Ba	1157	1081	1083	1010	1045	995
Y	40	42	40	44	264	47
Zr	284	274	277	259	263	254
Nb	22.6	22.5	21.9	22	22.5	21.5
Pb	13	13	16	10	13	13
INAA analyses (ppm)						
Sc	8.7	9.8	8.4	11.4	3.7	11.9
Cr	2	2	4	3	2	n.d.
Co	5.5	7.4	5.6	10.0	0.9	11.3
Cs	4.2	4.1	4.0	2.4	3.4	3.7
As	5.0	3.9	4.3	3.0	4.0	3.9
Sb	1.0	0.9	0.9	0.7	0.8	0.9
Se	2.1	2.1	1.7	1.8	2.4	1.9
La	29.7	27.8	28.3	27.8	27.1	28.0
Ce	62	54	64	61		58
Nd	28	24	31	36		32
Sm	7.62	7.30	7.15	8.18	0.984	7.80
Eu	1.57	1.60	1.52	1.65	0.37	1.73
Tb	1.09	1.13	1.07	1.21	4.94	1.17
Yb	4.2	4.0	3.9	4.7	4.5	4.0
Lu	0.66	0.60	0.56	0.70	0.66	0.60
Hf	7.3	6.9	7.0	6.8	7.6	6.3
Ta	1.5	1.5	1.4	1.5	2.0	1.4
Th	8.6	8.7	8.4	7.7	10.8	7.3
U	3.8	3.4	4.4	3.9	3.4	2.7

TABLE 6.2 (continued)

sample #	HH-91-37	HH-91-38	HH-91-39
map unit	Ta	Trd	Ta
XRF analyses (wt. %)			
SiO_2	62.2	66.1	63.6
TiO_2	1.13	0.57	0.96
Al_2O_3	16.15	15.54	15.64
$Fe_2O_3^*$	7.09	5.72	6.79
MnO	0.12	0.12	0.14
MgO	1.48	0.74	1.19
CaO	4.34	3.26	3.81
Na_2O	4.32	4.01	4.36
K_2O	2.87	3.66	3.06
P_2O_5	0.30	0.24	0.43
Total	99.54	99.54	99.49
XRF analyses (ppm)			
V	86	17	44
Ni	9	6	7
Cu	23.5	15.1	23.1
Zn	101	97	99
Ga	21	20	20
Rb	82	81	81
Sr	250	263	247
Ba	903	1293	945
Y	46	40	44
Zr	241	287	245
Nb	21.7	23.3	22.7
Pb	8	9	10
INAA analyses (ppm)			
Sc	14.3	9.2	12.4
Cr	3	3	5
Co	13.9	5.7	10.5
Cs	3.3	3.1	2.2
As	2.6	4.3	3.4
Sb	0.6	0.8	0.6
Se	1.8	2.1	1.9
La	28.2	29.5	27.8
Ce	51	65	60
Nd	31	34	33
Sm	8.03	7.83	8.32
Eu	1.87	1.92	1.98
Tb	1.34	1.12	1.27
Yb	4.2	4.0	4.1
Lu	0.61	0.54	0.57
Hf	6.8	7.2	6.5
Ta	1.5	1.4	1.4
Th	7.4	7.2	6.9
U	2.9	3.5	3.4

Table 6.3: Trace element compositions of Horsehead Mountain glass

sample #	JM-91-5g	HH-91-11g	HH-91-14g	HH-91-20g	HH-91-38g
map unit	Trd	Trd	Trd	Trd	Trd
INAA analyses (ppm)					
Sc	4.1	6.0	5.0	7.6	8.2
Cr	3	3	2	3	4
Co	1.4	3.3	2.9	4.9	4.4
Cs	5.2	4.9	5.3	4.6	3.6
As	5.3	6.1	5.4	3.8	4.3
Sb	1.2	1.2	1.2	1.1	0.8
Se	2.5	1.6	2.8	2.1	2.1
La	32.9	33.8	31.6	29.0	31.2
Ce	73	78	77	69	75
Nd	32	38	33	32	37
Sm	7.0	7.6	6.8	6.7	7.6
Eu	1.00	1.38	1.13	1.56	1.79
Tb	1.11	1.18	1.12	1.17	1.20
Yb	4.5	4.4	4.5	4.0	4.3
Lu	0.68	0.78	0.66	0.63	0.60
Hf	7.2	6.4	6.8	7.3	7.2
Ta	1.6	1.6	1.6	1.6	1.7
Th	11.6	10.2	10.9	9.1	8.0
U	5.2	4.2	4.6	3.7	3.3

INAA precision values are estimated to be 3 to 5%, except for Ce, Nd and U (10 to 15%).

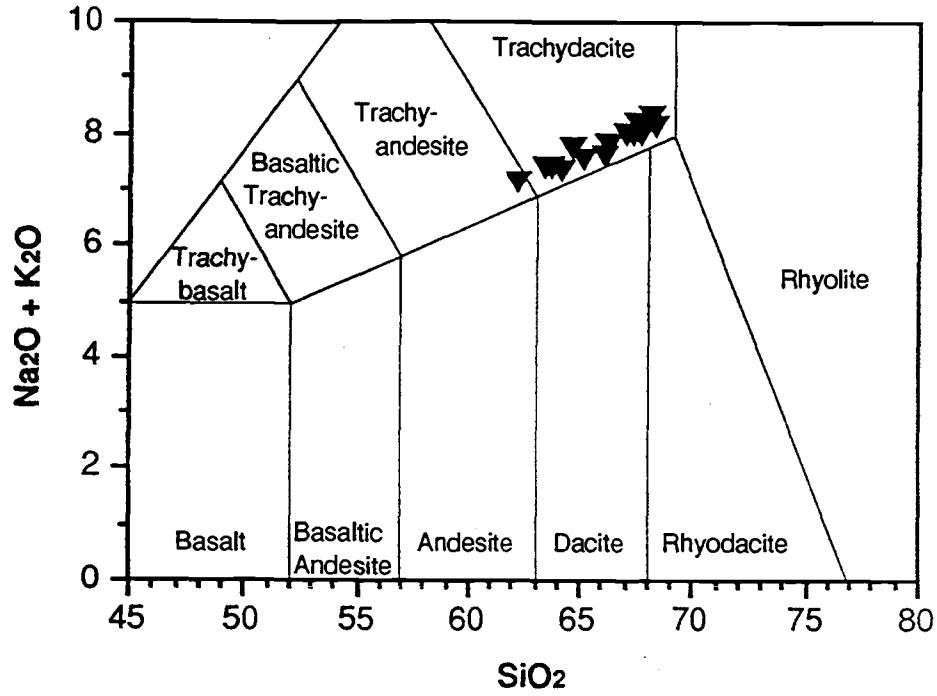

Figure 6.1: $Na_2O + K_2O$ vs. SiO_2 for Horsehead Mountain rocks, with the I.U.G.S. classification scheme of LeBas et al. (1986) shown for reference. Nomenclature is as described in Figure 3.5.

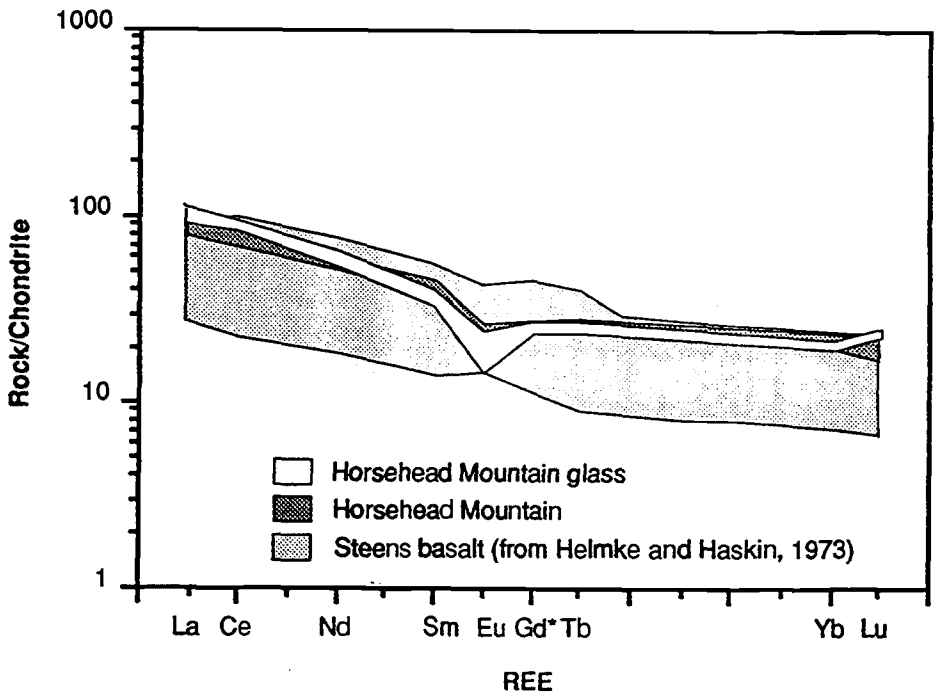

Figure 6.2: Chondrite-normalized rare-earth element diagram for Horsehead Mountain whole-rock compositions and glass seperates. Field of Steen's basalt compositions is shown for reference. Values for non-volatile C1 chondrite are from Anders and Ebihara (1982). Gd* is extrapolated from the heavy rare-earth trend.

the Imnaha and Grande Ronde formations of the Columbia River Basalt Group. He attributes the generation of calc-alkaline dacites to anatexis of a lower crustal granulite, followed by mixing with basalt to form the calc-alkaline andesites. Despite the calc-alkaline nature of the andesites and associated basalts, most workers agree that they are not in any way related to Cascade volcanism or any other arc (Robyn, 1979; Goles, 1986; Goles et al., 1989). By documenting two 15.5 Ma dome complexes (Horsehead Mountain and Little Juniper Mountain), this study shows that older calc-alkaline intermediate lavas are more widespread than previously thought.

A petrogenetic speculation that can be easily offered with respect to Horsehead Mountain magmatism is that direct evolution by crystal fractionation from coeval Steens-type basalt is not possible, because of overlapping rare-earth element patterns (Fig. 6.2). In order to better understand their evolution, future work should include:

1. Comparison of the Horsehead Mountain suite to other Miocene calc-alkaline intermediates in eastern Oregon in order to determine their extent, age range, and compositional variability.

2. Petrographic analysis and interpretation of the diverse mineral textures found in Horsehead Mountain rocks.

3. Chemical analysis of whole rock (if possible) and minerals in the several types of xenoliths in Horsehead Mountain rocks, which constitute a probe of the crust beneath the High Lava Plains in mid-Miocene time.

4. Chemical and isotopic modelling of Horsehead Mountain rocks to constrain their magmatic sources and their connection to Steens basalt volcanism.

BIBLIOGRAPHY

Abbott, R.N., Jr., 1978, Peritectic reactions in the system An-Ab-Or-Qz-H_2O: Canadian Mineralogist, v. 16, p. 245-256.

Anders, E., and Ebihara, M., 1982, Solar-system abundances of the elements: Geochimica et Cosmochimica Acta, v. 46, p. 2363-2380.

Anderson, D.J., and Lindsley, D.H., 1988, Internally consistent solution models for Fe-Mg-Mn-Ti oxides: Fe-Ti oxides: American Mineralogist, v. 73, p. 714-726.

Armstrong, R.L., Ekren, E.B., McKee, E.H., and Noble, D.C., 1969, Space-time relations of Cenozoic silicic volcanism in the Great Basin of the United States: American Journal of Science, v. 267, p. 478-490.

Armstrong, R.L., Leeman, W.P., and Malde, H.E., 1975, K-Ar dating, Quaternary and Neogene volcanic rocks of the Snake River Plain, Idaho: Americal Journal of Science, v. 275, p. 225-251.

Arth, J.G., 1976, Behavior of trace elements during magmatic processes -- a summary of theoretical models and their applications: U.S.G.S Journal of Research, v. 4, p. 41-47.

Atwater, T., 1970, Implications of plate tectonics for the Cenozoic tectonic evolution of western North America: Geological Society of America Bulletin, v. 81, p. 3513-3536.

Bacon, C.R., and Hirschmann, M.M., 1988, Mg/Mn partitioning as a test for equilibrium between coexisting Fe-Ti oxides: American Mineralogist, v. 73, p. 57-61.

Bailey, D.G., 1992, The Powder River volcanic field, northeastern Oregon: Evidence for crustal anatexis and magma mixing in the generation of calc-alkaline magmas associated with crustal extension [abs.]: Geological Society of America, Abstracts with Programs, v. 24, p. 5.

Bailey, D.G., and Conrey, R.M., 1992, Common parent magma for Miocene to Holocene mafic volcanism in the northwestern United States: Geology, v. 20, p. 1131-1134.

Beard, J.S., and Lofgren, G.E., 1991, Dehydration melting and water-saturated melting of basaltic and andesitic greenstones and amphibolites at 1, 3, and 6.9 kb: Journal of Petrology, v. 32, p. 365-401.

Berri, D.A., Cummings, M.L., and Johnson, M.J., 1983, Geology and alteration of a Pliocene silicic volcanic center, Glass Buttes, Oregon [abs.]: Geological Society of America Abstracts with Programs, v. 15, p. 326.

Blundy, J.D., and Wood, B.J., 1991, Crystal-chemical controls on the partitioning of Sr and Ba between plagioclase feldspar, silicate melts, and hydrothermal solutions: Geochimica et Cosmochimica Acta, v. 55, p. 193-209.

Brown, D.E., 1982, Map showing geology and geothermal resources of the southern half of the Burns 15' quadrangle, Oregon: State of Oregon Geological Map Series, GMS-20.

Carlson, R.W., 1984, Tectonic influence on magma composition of Cenozoic basalts from the Columbia Plateau and northwestern Great Basin, U.S.A. *in* Boyd, F.R., Explosive Volcanism: Inception, Evolution, and Hazards: National Research Council, p. 23-33.

Carlson, R.W., and Hart, W.K., 1987, Crustal genesis on the Oregon Plateau: Journal of Geophysical Research, v. 92, p. 6191-6206.

Carmichael, I.S.E., 1964, The petrology of Thingmuli, a Tertiary volcano in eastern Iceland: Journal of Petrology, v. 5, p. 435-460.

Carmichael, I.S.E., 1967, The iron-titanium oxides of salic volcanic rocks and their associated ferromagnesian silicates: Contributions to Mineralogy and Petrology, v. 14, p. 36-64.

Catchings, R.D., and Mooney, W.D., 1988, Crustal structure of east-central Oregon: relation between Newberry Volcano and regional crustal structure: Journal of Geophysical Research, v. 93, p. 10,081-10,094.

Christiansen, R.L., and Lipman, P.W., 1972, Cenozoic volcanism and plate tectonic evolution of the western United States. II. Late Cenozoic: Philosophical Transactions of the Royal Society of London, v. 271, p. 249-284.

Christiansen, R.L., and McKee, E.H., 1978, Late Cenozoic volcanic and tectonic evolution of the Great Basin and Columbia Intermontane regions: Geological Society of America Memoir 152, p. 283-311.

Clayton, R.W., 1989, Kinematics of the northern margin of the Basin and Range, Oregon [abs.]: Geological Society of America Abstracts with Programs, v. 21(5), p. 66

Cox, K.G., Bell, J.D., and Pankhurst, R.J., 1979, The interpretation of igneous rocks: George Allen & Unwin, London, 450 p.

Cummings, M.L., 1984, Glass domes at Round Top Butte, Glass Buttes silicic complex, south-central Oregon [abs.]: Proceedings of the Oregon Academy of Science, v. 20, p. 54.

Cummings, M.L., 1985, Volcanic stratigraphy of the Glass Buttes complex, southcentral Oregon [abs.]: Geological Society of America Abstracts with Programs, v. 17, p. 215.

Cummings, M.L., and Roche, R.L., 1989, Volcanic evolution of a silicic center astride the Brothers Fault Zone, the Glass Buttes complex, Oregon [abs.]: Geological Society of America, Abstracts with Programs, v. 21(5), p. 70.

Davenport, R.E., 1971, Geology of the Rattlesnake and older ignimbrites in the Paulina Basin and adjacent areas, central Oregon: Ph.D. Thesis, Oregon State University, 132 p.

Deer, W.A., Howie, R.A., and Zussman, J., 1966, An introduction to the rock-forming minerals: Longman Scientific and Technical, Essex, 528 p.

DePaolo, D.J., 1981, Trace element and isotopic effects of combined wallrock assimilation and fractional crystallization: Earth and Planetary Science Letters, v. 53, p. 189-202.

Dickinson, W.R., 1979, Mesozoic forearc basin in central Oregon: Geology, v. 7, p. 166-170.

Donath, F.A., 1962, Analysis of Basin-Range structure, southcentral Oregon: Geological Society of America Bulletin, v. 73, p. 1-16.

Dostal, J., Dupuy, C., Carron, J.P., Le Guen de Kerneizon, M., and Maury, R.C., 1983, Partition coefficients of trace elements: application to volcanic rocks of St. Vincent, West Indies: Geochimica et Cosmochimica Acta, v. 47, p. 525-533.

Drake, M.J., and Weill, D.F., 1975, The partitioning of Sr, Ba, Ca, Y, Eu^{2+}, Eu^{3+}, and other REE between plagioclase feldspar and magmatic silicate liquid: an experimental study: Geochimica et Cosmochimica Acta, v. 39, p. 689-712.

Draper, D.S., 1991, Late Cenozoic bimodal magmatism in the northern Basin and Range Province of southeastern Oregon: Journal of Volcanology and Geothermal Research, v. 47, p. 299-328.

Duncan, R.A., 1982, A captured island arc chain in the Coast Range of Oregon and Washington: Journal of Goephysical Research, v. 87, p. 10,827-10,837.

Duncan, R.A., McElwee, K.R., and Leeman, W.P., 1992, Timing and petrogenesis of Paleogene forearc volcanism, Oregon, Washington Coast Range: Geological Society of America Abstracts with programs, v. 24, p. 21.

Eby, G.N., 1990, The A-type granitoids: A review of their occurrence and chemical characteristics and speculations on their petrogenesis: Lithos, v. 26, p. 115-134.

Eby, G.N., 1992, Chemical subdivision of the A-type granitoids: petrogenetic and tectonic implications: Geology, v. 20, p. 641-644.

Frost, T.P., and Mahood, G.A., 1987, Field, chemical, and physical constraints on mafic-felsic magma interaction in the Lamarck Granodiorite, Sierra Nevada, California: Geological Society of America Bulletin, v. 99, p. 272-291.

Gans, P.B., Mahood, G.A., and Schermer, E., 1989, Synextensional magmatism in the Basin and Range province; a case study from the eastern Great Basin: Geological Society of America Special Paper 233, 53 p.

Geist, D., and Richards, M., 1993, Origin of the Columbia Plateau and Snake River Plain: deflection of the Yellowstone plume: Geology, v. 21, p. 789-792.

Geist, D.J., McBirney, A.R., and Baker, B.H, 1989, MacGPP: a program package for creating and using geochemical data files, 33 p.

Ghiorso, M.S., and Sack, R.O., 1991a, Fe-Ti oxide geothermometry: thermodynamic formulation and the estimation of intensive variables in silicic magmas: Contributions to Mineralogy and Petrology, v. 108, p. 485-510.

Ghiorso, M.S., and Sack, R.O., 1991b, Thermochemistry of the oxide minerals: Reviews in Mineralogy, v. 25, p. 221-264.

Goles, G.G., 1986, Miocene basalts of the Blue Mountains Province in Oregon. I: Compositional types and their geologic settings: Journal of Petrology, v. 27, p. 495-520.

Goles, G.G., Brandon, A.D., and Lambert, R.St.J., 1989, Miocene basalts of the Blue Mountains Province in Oregon; Part 2, Sr isotopic ratios and trace element features of little-known Miocene basalts of central and eastern Oregon, in Reidel, S.P., and Hooper, P.R., eds., Volcanism and tectonism in the Columbia River flood-basalt province: Geological Society of America Special Paper 239, p. 357-365.

Green, T. H., and Pearson, N.J., 1983, Effect of pressure on rare earth element partition coefficients in common magmas: Nature, v. 305, p. 414-416.

Green, T. H., and Pearson, N.J., 1985, Rare earth element partitioning between clinopyroxene and silicate liquid at moderate to high pressure: Contributions to Mineralogy and Petrology, v. 91, p. 24-36.

Greene, R.C., 1972, Preliminary geologic map of the Burns and West Myrtle 15-minute quadrangles, Oregon: United States Geological Survey Map MF-320, scale = 1:62,500.

Greene, R.C., 1973, Petrology of the welded tuff of Divine Canyon, southeastern Oregon: Geologcial Society of America Professional Paper 797, 26 p.

Greene, R.C., Walker, G.W., and Corcoran, R.E., 1972, Geologic map of the Burns quadrangle, Oregon: United States Geological Survey Map I-680, scale = 1:250,000.

Guffanti, M., and Weaver, C.S., 1988, Distribution of Late Cenozoic volcanic vents in the Cascade Range: volcanic arc segmentation and regional tectonic considerations: Journal of Geophysical Research, v. 93, p. 6513-6529.

Hart, W.K., 1984, Chemical and isotopic characteristics of silicic volcanism in S.E. Oregon, S.W. Idaho and northern Nevada [abs.]: EOS - Transactions of the American Geophysical Union, v. 65, p. 299.

Hart, W.K., Aronson, J.L., and Mertzman, S.A., 1984, Areal distribution and age of low-K, high-alumina olivine tholeiite magmatism in the northwestern Great Basin: Geological Society of America Bulletin, v. 95, p. 186-195.

Hart, W.K., and Carlson, R.W., 1987, Tectonic controls on magma genesis and evolution in the northwestern United States: Journal of Volcanology and Geothermal Research, v. 32, p. 119-135.

Hart, W.K., and Carlson, R.W., 1988, Characterization of the calk-alkaline to tholeiitic transition in the northern Basin and Range, Nevada: Geological Society of America Abstracts with Programs, v. 20, p. 315.

Hart, W.K., and Mertzman, S.A., 1982, K-Ar ages of basalts from southcentral and southeastern Oregon: Isochron/West, v. 33, p. 23-26.

Helmke, P.A., and Haskin, L.A., 1973, Rare-earth elements, Co, Sc, and Hf in the Steens Mountain basalts: Geochimica et Cosmochimica Acta, v. 37, p. 1513-1529.

Henderson, P., 1982, Inorganic geochemistry: Pergammon Press, Oxford, 353 p.

Hildreth, W., 1981, Gradients in silicic magma chambers: implications for lithospheric magmatism: Journal of Geophysical Research, v. 86, p. 10,153-10,192.

Hill, B.E., 1992, Petrogenesis of compositionally distinct silicic volcanoes in the Three Sisters region of the Oregon Cascade Range: the effects of crustal extension in the development of continental arc silicic magmatism: unpublished Ph.D. dissertation, Oregon State University, 247 p.

Honjo, N., Bonnichsen, B., Leeman, W.P., and Stormer, J.P., Jr., 1992, Mineralogy and geothermometry of high-temperature rhyolites from the central and western Snake River Plain: Bulletin of Volcanology, v. 54, p. 220-237.

Irvine, T.N., and Baragar, R.A., 1971, A guide to the classification of the common volcanic rocks: Canadian Journal of Earth Sciences, v. 8, p. 523-548.

Irving, A.J., 1978, A review of experimental studies of crystal-liquid trace element partitioning: Geochimica et Cosmochimica Acta, v. 42, p. 743-770.

Langer, V.W., 1992, Geology and petrologic evolution of the silicic to intermediate volcanic rocks underneath the Steens Mountain basalt, southeastern Oregon: unpublished Master's thesis, Oregon State University, 109 p.

Langmuir, C.H., Vocke, R.D., Jr., and Hanson, G.N., 1978, A general mixing equation with applications to Icelandic basalts: Earth and Planetary Science Letters, v. 37, p. 380-392.

Laul, J.C., 1979, Neutron activation analysis of geological materials: Atomic Energy Review, v. 17, p. 603-695.

Lawrence, R.D., 1976, Strike-slip faulting terminates the Basin and Range Province in Oregon: Geological Society of America Bulletin, v. 87, p. 846-850.

LeBas, M.J., LeMaitre, R.W., Streckeisen, A., and Zanettin, B., 1986, A chemical classification of volcanic rocks based on the total alkali-silica diagram: Journal of Petrology, v. 27, p. 745-750.

Lindsley, D.H., 1983, Pyroxene geothermometry: American Mineralogist, v. 68, p. 477-493.

Linneman, S.R., and Myers, J.D., 1990, Magmatic inclusions in the Holocene rhyolites of Newberry Volcano, central Oregon: Journal of Geophysical Research, v. 95, p. 17,677-17,691.

Livaccari, R.F., 1979, Late Cenozoic tectonic evolution of the western United States: Geology, v. 7, p. 72-75.

Luedke, R.G., and Smith, R.L., 1982, Map showing distribution, composition, and age of late Cenozoic volcanic centers in Oregon and Washington: U.S.G.S. Map I-1091-D, scale = 1: 1,000,000.

MacLeod, N.S., Walker, G.W., and McKee, E.H., 1975, Geothermal significance of eastward increase in age of upper Cenozoic rhyolitic domes in southeastern Oregon: U.S.G.S. Open File Report 75-348, 21p.

MacLeod, N.S., and Sherrod, D.R., 1988, Geologic evidence for a magma chamber beneath Newberry Volcano, Oregon: Journal of Geophysical Research, v. 93, p. 10,067-10,079.

Malde, H.E., and Powers, H.A., Jr., 1962, Upper Cenozoic stratigraphy of the western Snake River Plain, Idaho: Geological Society of America Bulletin, v. 73, p. 1197-1220.

Mahood, G.A., and Hildreth, W., 1983, Large partition coefficients for trace elements in high-silica rhyolites: Geochimica et Cosmochimica Acta, v. 47, p. 11-30.

Mathis, A.C., 1993, Geology and petrology of a 26-Ma trachybasalt to peralkaline rhyolite suite exposed at Hart Mountain, southern Oregon: unpublished Master's thesis, Oregon State University, 141 p.

McKee, E.H., and Walker, G.W., 1976, Potassium-argon ages of late Cenozoic silicic volcanic rocks, southeast Oregon: Isochron/West, v. 15, p. 37-41.

McKee, E.H., Duffield, W.A., and Stern, R.J., 1983, Late Miocene and early Pliocene basaltic rocks and their implications for crustal structure, northeastern California and south-central Oregon: Geological Society of America Bulletin, v. 92, p. 292-304.

Miller, C.F., and Mittlefehlt, D.W., 1982, Depletion of light rare-earth elements in felsic magmas: Geology, v. 10, p. 129-133.

Nash, W.P., and Crecraft, H.R., 1985, Partition coefficients for trace elements in silicic magmas: Geochimica et Cosmochimica Acta, v. 49, p. 2309-2322.

Nicholls, I.A., and Harris, K.L., 1980, Experimental rare earth element partition coefficients for garnet, clinopyroxene and amphibole coexisting with andesitic and basaltic liquids: Geochimica et Cosmochimica Acta, v. 44, p. 287-308.

Nielsen, R.L., 1985, EQUIL: A program for the modelling of low-pressure differentiation processes in natural mafic magma bodies: Computers & Geosciences, v. 11, p. 531-546.

Nielsen, R.L., 1992, BIGD.FOR: a FORTRAN program to calculate trace-element partition coefficients for natural mafic and intermediate composition magmas: Computers & Geosciences, v. 18, p. 773-788.

Noble, D.C., 1972, Some observations on the Cenozoic volcano-tectonic evolution of the Great Basin, western United States: Earth and Planetary Science Letters, v. 17, p. 142-150.

O'Hara, M.J., 1977, Geochemical evolution during fractional crystallization of a periodically refilled magma chamber: Nature, v. 266, p. 503-507.

Papike, J.J., Cameron, K.L., and Baldwin, K., 1974, Amphiboles and pyroxenes: characterization of other than quadrilateral components and estimates of ferric iron from microprobe data: Geological Society of America Abstracts with Programs, v. 6, p. 1053.

Parker, D.J., 1974, Petrology of selected volcanic rocks of the Harney Basin, Oregon: Ph.D. Thesis, Oregon State University, 119 p.

Patino-Douce, A.E., and Johnston, A.D., 1991, Phase equilibria and melt productivity in the pelitic system: implications for the origin of peraluminous granitoids and aluminous granulites: Contributions to Mineralogy and Petrology, v. 107, p. 290-315.

Pearce, J.A., and Norry, M.J., 1979, Petrogenetic implications of Ti, Zr, Y, and Nb variations in volcanic rocks: Contributions to Mineralogy and Petrology, v. 69, p. 33-47.

Pearce, J.A., Harris, N.B.W., and Tindle, A.G., 1984, Trace element discrimination diagrams for the tectonic interpretation of granitic rocks: Journal of Petrology, v. 25, p. 956-983.

Rapp, R.P., Watson, E.B., and Miller, C.F., 1991, Partial melting of amphibolite/eclogite and the origin of Archean trondhjemites and tonalites: Precambrian Research, v. 51, p. 1-25.

Robyn, T.L., 1979, Miocene volcanism in eastern Oregon: an example of calc-alkaline volcanism unrelated to subduction: Journal of Volcanology and Geothermal Research, v. 5, p. 145-161.

Roche, R.L., 1988, Stratigraphic and geochemical evolution of the Glass Buttes complex, Oregon: Master's Thesis, Portland State University, 99p.

Samson, S.D., and Alexander, E.C., Jr., 1987, Calibration of the interlaboratory ^{40}Ar-^{39}Ar dating standard, MMhb-1: Chemical Geology and Isotope Geosciences, v. 66, p. 27-34.

Sawka, W.N., 1988, REE and trace element variations in accessory minerals and hornblende from the strongly zoned McMurry Meadows pluton, California: Transactions of the Royal Society of Edinburgh: Earth Sciences, v. 79, p. 157-168.

Scholz, C.H., Barazangi, M., and Sbar, M., 1971, Late Cenozoic evolution of the Great Basin, western United States, as an ensialic interarc basin: Geological Society of America Bulletin, v. 82, p. 2979-2990.

Seedorff, E., 1991, Magmatism, extension, and ore deposits of Eocene to Holocene age in the Great Basin - mutual effects and preliminary proposed genetic relationships, in Raines, G.L, Lisle, R.E., Schafer, R.W., and Wilkinson, W.H., eds., Geology and ore deposits of the Great Basin: Geological Society of Nevada and United States Geological Survey Symposium, Proceedings, p. 133-178.

Snyder, W.S., Dickinson, W.R., and Silberman, M.L., 1976, Tectonic implications of space-time patterns of Cenozoic magmatism in the western United States: Earth and Planetary Science Letters, v. 32, p. 91-106.

Stewart, J.H., and Carlson, J.E., 1976, Cenozoic rocks of Nevada: four maps and brief description of distribution, lithology, age, and centers of volcanism: Nevada Bureau of Mines Geological Map 52, scale 1:1,000,000.

Stormer, J.C., 1983, The effects of recalculation on estimates of temperature and oxygen fugacity from analyses of multicomponent iron-titanium oxides: American Mineralogist, v. 68, p. 586-594.

Streck, M.J., 1991, Local and regional facies and facies variations within the Rattlesnake Tuff, a wide-spread ash-flow tuff sheet in eastern Oregon [abs.]: EOS-Transactions of the American Geophysical Union, v. 74, p. 568-569.

Streck, M.J., 1992, Element gradients in the high-silica rhyolites and dacites from the Rattlesnake Tuff, southeastern Oregon [abs.]: Geological Society of America Abstracts with Programs, v. 24, p. 83.

Streck, M.J., and Grunder, A.L., 1991, The Rattlesnake ash-flow tuff, eastern Oregon: zoning and a large compositional gap [abs]: Geological Society of America, Abstracts with Programs, v. 23, no. 2, p. 101.

Taylor, J.R., 1982, An introduction to error analysis: University Science Books, Mill Valley, California.

Vielzeuf, D., and Holloway, J.R., 1988, Experimental determination of the fluid-absent melting relations in the pelitic system: Contributions to Mineralogy and Petrology, v. 98, p. 257-276.

Walker, G.W., 1974, Some implications of late Cenozoic volcanism to geothermal potential in the High Lava Plains of south-central Oregon: The Ore Bin, v. 36, p. 109-119.

Walker, G.W., 1979, Revisions to the Cenozoic stratigraphy of Harney Basin, southeastern Oregon: United States Geological Survey, Bulletin 1475, 35p.

Walker, G.W., 1981, Uranium, thorium and other metal associations in silicic volcanic complexes of the northern Basin and Range, a preliminary report: United States Geological Survey Open-File Report 81-1290, 45 p.

Weaver, J.S., and Langmuir, C.H., 1990, Calculation of phase equilibrium in mineral-melt systems: Computers and Geosciences, v. 16, p. 1-19.

Wernicke, B.P., Christiansen, R.L., England, P.C., and Sonder, L.J., 1987, Tectonomagmatic evolution of Cenozoic extension in the North American Cordillera, in Coward, M.P., Dewey, J.F., and Hancock, P.L. (eds.), Continental Extensional Tectonics: Geological Society Special Publication 28, p. 203-221.

Whalen, J.B., Currie, K.L., and Chappell, B.W., 1987, A-type granites: geochemical characteristics, discrimination and petrogenesis: Contributions to Mineralogy and Petrology, v. 95, p. 407-419.

Wilson, R.T., Rehrig, W.A., and Christiansen, E.H., 1983, Silicic volcanism and continental extension: implications for the nature of the crust in the western United States: Geological Society of America Abstracts with Programs, v. , p. 288.

Wolf, M.B., and Wyllie, P.J., 1992, Dehydration-melting of solid amphibolite at 10 kbar: textural development, liquid interconnectivity and applications to the segregation of magmas: Mineralogy and Petrology, v. 44, p. 151-179.

Zoback, M.L., and Thompson, G.A., 1978, Basin and Range rifting in northern Nevada: Clues from a mid-Miocene rift and its subsequent offsets: Geology, v. 6, p. 111-116.

APPENDICES

APPENDIX 1: Petrographic description of map units at Juniper Ridge and Horsehead Mountain

Younger Rocks

High-alumina olivine tholeiite (Tob_1, Tobg, Tob_h): Includes plateau-forming basalt flows (Tob_1, Tobg) with minor basal hydroclastic deposits (Tob_h) at eastern Juniper Ridge. Basalt flows contain several percent phenocrysts of olivine and plagioclase in a diktytaxitic, subophitic, vesicular matrix of plagioclase > pyroxene > olivine > opaque oxides. **Olivine** phenocrysts are blocky and subhedral, ranging in size up to 2 mm in length. Olivine crystals that exceed the average groundmass size usually make up 1 to 7 percent of the rock, but are indistinguishable petrographically from groundmass olivine, except that groundmass olivine is usually anhedral and equant. Both phenocryst and groundmass olivine crystals are partially replaced by iddingsite from their margins inward. **Plagioclase** crystals rarely exceed the average groundmass size, except in Tob_1, which contains about 10 percent large, euhedral, bytownite (An_{75} by Carlsbad-albite) phenocrysts ranging from 5 to 10 mm in length. The **groundmass** of the plateau-forming basalts is composed of 40 to 50 percent plagioclase, which forms an interlocking matrix of euhedral, tabular grains 0.1 to 2 mm in length, 20 to 30 percent anhedral, subophitic to ophitic clinopyroxene up to 2 mm across, 5 to 20 percent anhedral, equant, intergranular olivine ranging from 0.1 to 1 mm in diameter, and 5 to 10 percent opaque oxides that are either equant and anhedral, or acicular and subhedral, and range in size from 0.05 to 0.2 mm. These rocks contain 5 to 15 percent vesicles into which plagioclase laths commonly protrude (diktytaxitic texture). Hydroclastic deposits (Tob_h) found at the base of plateau basalts in eastern Juniper Ridge are composed of angular shards of brown basaltic glass ranging from 0.25 to 2 mm in diameter, in a matrix of finely comminuted basaltic glass. Shards and matrix both contain sparse phenocrysts of euhedral olivine and plagioclase phenocrysts, which often exhibit skeletal (quench?) morphology. Silicic glass shards, pumice, and mineral grains from unit Tr_4 are also present; they are rare in proximal hyaloclastite deposits (Sample JR-92-58) but increase in abundance to over 50 percent of total grains at distal outcrops (Sample JR-92-55).

Mafic vents (Tmv): Cinder cones, often associated with small lava flows, are composed of olivine basalt that is finer-grained, but otherwise identical petrographically to the plateau-forming basalt. Samples collected from mafic vents contain plagioclase > olivine > oxide phenocrysts in a diktytaxitic, pilotaxitic, vesicular groundmass of plagioclase, clinopyroxene, olivine and opaque oxide minerals. **Plagioclase** (5 to 10 percent) phenocrysts are euhedral to subhedral and range from 0.5 to 2 mm in length. Anorthite content of the plagioclase is 65 to 70 percent (labradorite; Carlsbad-albite method). Plagioclase phenocrysts are often poikilitic, enclosing grains of olivine and pyroxene. **Olivine** (trace to 5 percent) ranges from 0.1 to 1 mm in diameter and is anhedral, equant, and commonly rimmed by iddingsite. **Opaque oxides** (0.5 to 5 percent) are equant, anhedral, and range from 0.1 to 0.2 mm in diameter. Rare **alkali feldspar** crystals up to 0.5 mm in length have eroded margins and sieved interiors. The **groundmass** is composed of about 45 percent euhedral, tabular plagioclase, 25 to 35 percent clinopyroxene, about 10 percent olivine and 5 to 20 percent oxide minerals. Groundmass plagioclase ranges up to 0.1 mm in length and is pilotaxitic; anhedral, equant pyroxene olivine and oxide grains range from 0.01 to 0.05 mm in diameter. The groundmass contains 5 to 10 percent smooth-walled vesicles.

Western Juniper Ridge

Squaw Butte basaltic andesite (Toa_1): Dark grey, sparsely phyric andesite with less than 10 percent phenocrysts of plagioclase and olivine in an aphanitic groundmass. **Plagioclase** phenocrysts (3 to 5 percent) are blocky, euhedral and range in length from 0.1 to about 1.5 mm. Trace amounts of plagioclase with anomalous blue extinction range up to 3 mm in length and are subhedral. **Olivine** (2 to 3 percent) is mostly euhedral, often exhibiting diamond-shaped outlines in thin section, and ranges from 0.1 to 1 mm in diameter. Up to 1 percent **opaque oxides** are euhedral and range from 0.05 to 0.2 mm in diameter. Trace amounts of colorless to light brown, slightly pleochroic, uniaxial (-), very low birefringence, moderately high relief, prismatic, hexagonal **apatite** are also present. Pleochroism in apatite ranges from light tan (slow direction) to brown (fast direction) and is greatest perpendicular to the c-axis. Apatite crystals are euhedral, bipyramidal prisms, ranging from 0.1 to 0.3 mm in length and display distinct basal parting. The **groundmass** is pilotaxitic and consists of 40 to 60 percent acicular plagioclase ranging from 0.01 to 0.1 mm in length, 25 to 30 percent mottled, microlitic brown glass, 15 to 20 percent anhedral clinopyroxene ranging from 0.01 to 0.05 mm in diameter, 10 to 15 percent anhedral olivine ranging from 0.01 to 0.05 mm in diameter, and 5 to 10 percent opaque oxide minerals ranging from 0.01 to 0.02 mm in diameter.

Phyric high-silica rhyolite (Tr_2): Grey to greenish grey, pumiceous to perlitic rhyolite glass with 3 to 5 percent phenocrysts of sanidine > quartz > clinopyroxene ± plagioclase ± fayalite ± orthopyroxene ± opaque oxides ± zircon. **Sanidine** (0.5 to 3 percent) ranges from 0.1 to 1.5 mm in length and is usually subhedral, although some crystals are euhedral or anhedral. Tabular sanidine phenocrysts are often bent or broken. Rare sanidine phenocrysts have seived plagioclase cores. **Quartz** crystals (ranging up to 1 percent) average about 0.5 mm, but range from 0.1 to 1 mm in diameter and occur as equant, rounded, anhedral grains, commonly displaying concentric fractures. A small percentage of quartz grains have embayed margins. Quartz also occurs rarely as vermicular intergrowths with feldspar. **Clinopyroxe**ne (trace to almost 0.5 percent) is green, biaxial (+) and non-pleochroic, and occurs either as euhedral, acicular grains up to 2 mm in length. In devitrified or altered samples, clinopyroxene is partially or wholly replaced by secondary oxides. **Fayalite and orthopyroxene** occur as slightly elongate, prismatic, subhedral grains ranging from 0.01 to 0.5 mm in diameter. When present, **plagioclase** occurs in trace amounts and is usually euhedral or slightly subhedral, with grain sizes ranging up to 1 mm in length. Plagioclase also occurs as embayed cores within subhedral alkali feldspar crystals. Trace **oxide minerals** may be dispersed throughout the groundmass or occur within glomerocrysts with feldspar. Oxides are equant and sometimes euhedral, but more commonly display rounded or embayed grain margins, and range in size from 0.05 to 0.1 mm in diameter. Equant, subhedral **zircon** crystals up to 0.02 mm in diameter occur as trace phases in several samples, where they are included in feldspar or pyroxene crystals. Several samples contain **olivine xenocrysts** in which anhedral, intergranular olivine occurs in glomerocrysts with euhedral plagioclase. The **groundmass** for phyric rhyolite flows ranges from completely glassy to completely devitrified, with increasing percentage of spherulites and/or vesicle-filling SiO_2 minerals. Flow banding in devitrified samples is defined by layers of microcrystalline quartz and feldspar alternating with spherulitic layers. Up to 15 volume percent vesicles are present; dense glass between vesicles often exhibits perlitic fractures.

Andesite and dacite (Tad_1): Dark grey to black, porphyritic andesite and dacite, characterized by large plagioclase phenocrysts, along with glomerocrysts of plagioclase and olivine and xenocrysts of alkali feldspar, quartz, and clinopyroxene. **Plagioclase** phenocrysts occur both as large, vitreous, subhedral, tabular megacrysts (2 to 5 percent) up to 2 cm long, and in radiate glomerocrysts (2 to 3 percent) with olivine. Plagioclase megacrysts are sometimes skeletal, containing inclusions of groundmass material. About 1 to 2 percent **olivine** ranges above the average groundmass in size (up to 1 mm) and is subhedral and blocky, occurring interstitially between radiate plagioclase in glomerocrysts or as isolated grains in the groundmass. **Alkali feldspar** (2 percent) occurs as anhedral, frittered, or broken grains from 0.5 to 2 mm in size, and commonly is in reaction with the groundmass, displaying brown, finely dendritic margins. Most samples of Tad_1 contain trace to 1 percent **quartz**, which ranges from 0.5 to 1 mm in diameter, and is equant, anhedral, and occasionally embayed. Reaction rims of clinopyroxene occur around quartz xenocrysts in some samples. Light green, anhedral, embayed **clinopyroxene** xenocrysts ranging from 0.2 to 0.5 mm in length occur in trace amounts in some samples. In most rocks mapped as Tad_1, the **groundmass** consists of 20 to 70 percent mottled or partially devitrified brownish glass, 20 to 50 percent euhedral plagioclase laths ranging from 0.01 to 0.2 mm in length, 5 to 20 percent subhedral, prismatic pyroxene ranging from 0.01 to 0.1 mm in diameter, and 5 to 10 percent anhedral, equant, iddingsitized olivine, which ranges from 0.1 to 0.2 mm in diameter. Up to 5 percent equant, euhedral opaque oxide minerals ranging from 0.01 to 0.1 mm in diameter may be dispersed throughout the groundmass. Alignment of plagioclase laths along flow lines around phenocrysts is common. The groundmass usually contains slightly coarser- or finer-grained domains with the same general mineralogy that may represent cognate xenoliths or may be due to imperfect mixing between magmas. In contrast to trachytoid groundmass texture, plagioclase laths in the coarser-grained domains are not aligned. One sample mapped as Tad_1 (JR-91-19) contains 10 to 15 percent basalt inclusions with irregular, finely cuspate margins in a groundmass of high-silica rhyolite, petrologically identical to map unit Tr_2, but also containing several percent large, vitreous plagioclase megacrysts that are typical of the rest of Tad_1.

Low-silica (microlitic and crystal-poor) rhyolite (Tr_3): To the west of Ramer Peak fault, Tr_3 occurs as aphyric glass; to the east, zoned flows consist of variably devitrified rhyolite with up to 5 percent phenocrysts of plagioclase > clinopyroxene > orthopyroxene > opaque oxides. **Plagioclase** (2 to 5 percent) ranges from 0.1 to 2 mm in length and occurs as subhedral to anhedral, tabular crystals, often with pronounced concentric zoning. Plagioclase is occasionally glomerocrystic with pyroxene. Plagioclase crystals are rarely seived, with cores containing regularly spaced, geometrical inclusions of brown glass. Moderately pleochroic, biaxial (-) **clinopyroxene** grains (trace to 1 percent) range in size from 0.1 to 0.75 mm in length and are either equant (subhedral) or prismatic (euhedral). Pleochroism ranges from green (fast direction) to brown (slow direction). **Oxide minerals** (trace to 0.5 percent) occur as euhedral, equant grains 0.1 to 0.2 mm in diameter or replace clinopyroxene in oxidized samples. When fresh, the **groundmass** consists of vesicular, partially spherulitic and/or perlitic glass; devitrified samples have mottled, banded groundmasses. In flow-banded samples, elongate phenocrysts are aligned parallel to flowbanding; one sample (JR-91-28) has a glassy groundmass that contains about 20 percent acicular microlites that show local flow alignment.

Eastern Juniper Ridge

Glomerophyric olivine andesite (Toa_2): Black, glomerophyric andesite with phenocrysts of plagioclase > clinopyroxene > olivine > opaque oxides in a pilotaxitic groundmass. **Plagioclase** (3 to 4 percent) includes euhedral, normally zoned crystals (2 to 3 percent) ranging up to 1 mm long, and coarsely skeletal, anhedral crystals (1 to 2 percent) that occur mostly in glomerocrysts and range up to 2 mm long. Rare euhedral plagioclase contains a thin zone of inclusions near the outer margin of the grain. **Clinopyroxene** crystals (1 to 2 percent) are euhedral, blocky, and range from 0.25 to 0.75 mm in length. **Olivine** (about 1 percent) is euhedral, averages about 0.5 mm in diameter and occurs in glomerocrysts with plagioclase. Trace opaque oxides are euhedral to slightly embayed and average about 0.1 mm in diameter. The **groundmass** is pilotaxitic and consists of about 50 percent acicular plagioclase crystals up to 0.1 mm long, about 30 percent brown, intersertal glass, 15 percent anhedral, intergranular clinopyroxene ranging up to 0.01 mm in diameter, and 5 percent equant, anhedral oxide minerals ranging up to 0.03 mm in diameter.

Aphanitic olivine andesite (Toa_3): Dark grey, almost aphyric, aphanitic andesite with less than 1 percent phenocrysts of plagioclase > pyroxene > olivine > opaque oxides. **Plagioclase** (about 0.5 to 1 percent) is mostly euhedral and ranges from 0.5 to 1 mm in length. A small percentage of larger plagioclase grains are anhedral and have resorbed, frittered margins. **Clinopyroxene** crystals (less than 1 percent) are anhedral and range between 0.2 and 0.5 mm in diameter. Trace **olivine** and **opaque** minerals are equant, euhedral and range from 0.1 to 0.3 mm in diameter. The **groundmass** is slightly pilotaxitic and consists of 60 percent acicular plagioclase from 0.01 to 1 mm in length, 20 percent devitrified glass and 20 percent anhedral clinopyroxene, olivine and opaque minerals ranging from 0.01 to 0.5 mm in diameter.

Andesite and dacite (Tad_2): Grey to black, devitrified or glassy andesite and dacite with phenocrysts of alkali feldspar > plagioclase > clinopyroxene ± olivine >> opaque oxides. **Alkali feldspar** ranges from 0.5 to 2 percent and includes relatively large (1 to 2 mm) cross-hatched microcline (?) and smaller (0.5 to 1 mm) untwinned sanidine (?). Both varieties of alkali feldspar are euhedral to subhedral and are occasionally broken; untwinned alkali feldspar may exhibit brown, finely skeletal reaction rims in more mafic samples. **Plagioclase** (usually less than 1 percent in dacite; up to 2 percent in andesite) ranges from 0.5 to 2 mm in length and is euhedral. About one percent subhedral **olivine** occurs as phenocrysts in the most mafic andesite. Light green, euhedral, prismatic, non-pleochroic, biaxial (-) **clinopyroxene**, ranging from 0.1 to 0.5 mm in length occurs in trace amounts. Trace amounts of equant, euhedral **oxide minerals** ranging from 0.1 to 0.2 mm in diameter are also present. Phenocrysts are enclosed in a vitrophyric, hyalopilitic or devitrified **groundmass** that when fresh consists of light brown glass with very fine-grained, hairlike microlites ranging up to 0.01 mm in length. The groundmass in andesites contains about 50 percent mottled, brownish glass, 25 to 30 percent euhedral plagioclase ranging from 0.01 to 0.2 mm in length, 10 to 15 percent anhedral, equant clinopyroxene ranging in diameter from 0.01 to 0.05, and 5 percent iddingsitized olivine with similar shape and grain size to groundmass pyroxene.

Aphanitic olivine basalt (Tob_2): Dark grey, aphanitic, almost aphyric basalt containing trace plagioclase phenocrysts in an ophitic, intersertal, intergranular, diktytaxitic groundmass. Trace **plagioclase** with anhedral, resorbed margins ranges above the average groundmass size (up to 0.5 mm). The **groundmass** consists of an interlocking matrix of euhedral plagioclase (40 percent) ranging from 0.01 to 0.2 mm in length, 25 percent intersertal brown glass, about 20 percent anhedral, ophitic clinopyroxene ranging up to 2 mm in diameter, 10 percent intergranular anhedral olivine ranging from 0.05 to 0.1 mm in diameter, and 5 percent euhedral opaque oxides ranging from 0.01 to 0.1 mm in diameter. The groundmass contains 5 to 10 percent small, diktytaxitic vesicles.

Phyric rhyolite (Tr_4): Grey, crystal-rich vitrophyre with up to 20 percent crystals of alkali feldspar > pyroxene > plagioclase > oxides >> zircon in a groundmass of microlitic rhyolite glass. **Alkali feldspar** (5 to 10 percent) occurs in two forms: 3 to 7 percent is euhedral, unzoned, and ranges from 0.01 to 0.5 mm in length; 2 to 3 percent is subhedral, sieved, ranges up to 1 mm in length and occurs in radiate glomerocrysts with pyroxene and plagioclase. **Plagioclase** (2 to 3 percent) is relatively euhedral and ranges from 0.01 to 2 mm in length. **Orthopyroxene** (4 to 5 percent) includes a light green to tan pleochroic, biaxial (-) variety as well as trace amounts of darker green, non-pleochroic, biaxial (+) pyroxene. Pleochroic pyroxene is prismatic, euhedral and ranges from 0.05 to 0.5 mm in length; non-pleochroic pyroxene is stubbier, ranging from 0.1 to 0.5 mm in length and is occurs in glomerocrysts. About 1 percent equant, subhedral **oxide minerals** ranging between 0.02 and 0.2 mm in diameter occurs in the glassy groundmass, along with trace amounts of **zircon**. The **groundmass** contains bands of brown and clear glass. Acicular microlites in the clear glass protrude into the brown glass where the two glass types are in contact, but are otherwise absent in the brown glass. Brown glass also occurs in inclusions in sieved feldspar grains.

Southern Juniper Ridge

Andesite and dacite (Tad_3): Black dacitic vitrophyre with phenocrysts of plagioclase > alkali feldspar > clinopyroxene > opaque minerals and trace rhyolite inclusions in a groundmass of banded, microlitic glass. **Plagioclase** (about 1 percent) ranges from 1 to 2 mm in length and is mostly euhedral, with a small population of subhedral, skeletal grains. **Alkali feldspar** (0.5 percent) grains exhibit concentric zoning, are euhdral and range from 0.5 to 1 mm in length. Trace light green, non-pleochroic **clinopyroxene** is anhedral when it occurs in glomerocrysts with feldspar, but euhedral when isolated in the groundmass, and ranges up to 0.5 mm in length. Trace amounts of euhedral **opaque oxides** are present, as well as angular inclusions of microlitic brown glass. Acicular microlites in the **groundmass** are aligned parallel to color bands in the black to grey glass. Phenocrysts in the groundmass are similarly aligned.

Horsehead Mountain

Crystal-rich and crystal-poor rhyodacite and dacite (Trd and Td): Black, glassy, seriate, crystal-rich dacite and rhyodacite consisting of 10 to 30 percent (Trd) or 5 to 10 percent (Td) crystals of plagioclase, clinopyroxene, orthopyroxene, potassium feldspar and oxide minerals in a groundmass of black to colorless, flow-layered, sometimes microlitic glass. **Plagioclase** is the most abundant phase (10 to 20 percent) and exhibits a diversity of textural types, the most characteristic of which is large, seived crystals up to 4 mm in length, with rounded grain margins and oscillatory zoning, often occurring in glomerocrysts with pyroxene. Brown glass inclusions in the seived feldspars are large and irregularly shaped, but appear to be crystallographically oriented. Other plagioclase crystals are euhedral, elongate, concentrically zoned and range from 0.1 to 1 mm in length. Rocks included in map units Trd and Td can contain from 6 to 8 percent phenocrysts of clinopyroxene or orthopyroxene, or more commonly both. **Clinopyroxene** crystals are biaxial (+), pleochroic from light green to tan, and range from 0.5 to 1 mm long. **Orthopyroxene** grains are light green, biaxial (-), non-pleochroic, and occur as anhedral to subhedral prisms ranging from 0.1 to 2 mm in length. In devitrified samples, both pyroxene types are replaced by magnetite. **Alkali feldspar** phenocrysts (1 to 5 percent) are subhedral, range from 1 to 3 mm in diameter and commonly exhibit finely vermicular, feathery margins that consist of thin subparallel intergrowths that are perpendicular to grain margins. Other alkali feldspar grains exhibit finely seived interiors with thin euhedral rims. **Oxide** minerals (2 to 6 percent) are rounded to embayed, equant, and range from 0.1 to 0.4 mm in diameter. Rare euhedral **amphibole** (biaxial (+), pleochroic from green to dark brown) is found in several samples and may be xenocrystic. Fine-grained, **cognate inclusions** are found mainly in Trd and are composed of randomly oriented, interlocking aggregates of lath-shaped plagioclase and acicular oxide minerals with interstitial brown glass. Rare **xenoliths** include fine-grained, layered quartzite, coarse-grained gabbro and medium-grained, biotite- and zircon-bearing granitoid. The **groundmass** consists of up to 70 percent brown glass, microlitic colorless glass, or intricate interfingerings of both, and 30 percent square to slightly rectangular, seriate plagioclase tablets ranging from 0.01 to 0.4 mm in length. Microlitic colorless glass contains very small (0.001 to 0.05 mm) acicular plagioclase (?) crystals that parallel banding and protrude slightly into brown glass where the two glass types are in contact. Flow layering in the groundmass is defined by alingment of microcrystals, and by interlayering of brown and clear glass.

Aphanitic andesite (Ta): Dark grey, aphanitic, vesicular andesite and dacite with less than 5 percent phenocrysts of plagioclase, pyroxene and oxides in a pilotaxitic groundmass. **Plagioclase** (1 to 3 percent) ranges up to 1.5 mm in length and consists of several textural groups, including (1) euhedral to subhedral, blocky laths with complex oscillatory zonation, occurring in glomerocrysts with clinopyroxene or as isolated grains, (2) euhderal, elongate, unzoned laths, (3) larger, seived and/or poikilitic grains, (4) euhderal grains with finely seived margins, and (5) grains with seived cores and euhedral rims. Euhedral to subhedral **orthopyroxene** (0 to 1 percent) ranges from 0.2 to 0.7 mm in length, has near-parallel extinction, and is pleochroic in green (fast direction) and tan (slow direction). **Clinopyroxene** (0 to 0.5 percent) ranges up to 0.5 mm in length, is subhedral and includes both biaxial (+) and biaxial (-) varieties. Euhedral **oxide minerals** (less than 1 percent) are equant and range from 0.01 to 0.25 mm in diameter. The **groundmass** is either glassy or felty and trachytoid. Glassy groundmass types are mottled and microlitic; crystalline groundmass types are composed of 60 to 70 percent euhedral plagioclase up to 0.05 mm in length, about 20 to 30 percent devitrified glass, and about 10 percent oxide minerals up to 0.02 mm in diameter. Some groundmass plagioclase has swallowtail structure. Vesicles range up to almost 50 percent in some andesites, and are commonly elongate or gash-like.

APPENDIX 2: Juniper Ridge sample locations

Younger Basalts

Map unit	sample #	type	latitude	longitude
Tob_1	JR-92-59*	HS,TS	43.493	119.580
Tobg	JR-91-14*	HS,TS	43.524	119.703
	JR-92-53*	HS,TS	43.485	119.538
	JR-92-60	HS,TS	43.483	119.583
Tob_h	JR-92-55	HS,TS	43.485	119.546
	JR-92-58	HS,TS	43.494	119.565
Tmv	JR-91-23	HS	43.487	119.676
	JR-91-29	HS,TS	43.492	119.680
	JR-92-68	HS,TS	43.450	119.667

Western Juniper Ridge

Map unit	sample #	type	latitude	longitude
Toa_1	SB-91-1	HS	43.478	119.724
	JR-91-12*	HS,TS	43.464	119.708
	JR-91-21*	HS,TS	43.480	119.722
	JR-92-66	HS,TS	43.443	119.696
Tr_1	JR-91-4 *	HS	43.506	119.756
	JR-91-17	HS	43.480	119.717
	JR-91-20*	HS	43.480	119.718
	JR-91-22	HS	43.475	119.711
	JR-91-24	HS	43.501	119.739
	JR-91-25*#	HS	43.484	119.755
	JR-92-70	HS	43.496	119.736
Tr_2	HP-91-13*#	HS,TS	43.512	119.710
	JR-91-2 *	HS,TS	43.509	119.740
	JR-91-10	HS,TS	43.507	119.722
	JR-91-13*	HS,TS	43.480	119.751
	JR-91-15	HS,TS	43.504	119.732
	JR-91-18*	HS,TS	43.466	119.700
	JR-91-26	HS,TS	43.508	119.698
	JR-92-61	HS,TS	43.514	119.751
	JR-92-69	HS,TS	43.495	119.716

(*) geochemical sample; (#) dated sample; (HS) hand sample; (TS) thin section

Western Juniper Ridge (continued)

Map unit	sample #	type	latitude	longitude
Tad_1	JR-91-6	HS,TS	43.493	119.762
	JR-91-11*	HS,TS	43.494	119.765
	JR-91-19*	HS,TS	43.451	119.675
	JR-91-27*	HS,TS	43.507	119.690
	JR-92-67	HS,TS	43.470	119.706
	JR-92-71*	HS,TS	43.484	119.755
Tr_3	JR-91-3	HS,TS	43.521	119.762
	JR-91-5*	HS	43.498	119.760
	JR-91-8	HS	43.516	119.765
	JR-91-9	HS	43.517	117.767
	JR-91-28	HS,TS	43.507	119.688
	JR-91-30	HS,TS	43.516	119.697
	JR-91-31	HS,TS	43.533	119.673
	JR-91-32	HS	43.534	119.681
	JR-91-33	HS,TS	43.518	119.703
	JR-91-34*	HS,TS	43.523	119.684
	JR-91-35*	HS	43.531	119.669
	JR-91-36	HS	43.510	119.675
	JR-91-37	HS	43.508	119.661
	JR-91-38	HS,TS	43.523	119.670
	JR-91-39	HS	43.523	119.667
	JR-91-40	HS	43.526	119.657
	JR-91-41	HS	43.515	119.666
	JR-92-62*	HS	43.517	119.755
	JR-92-72*	HS	43.483	119.785

Eastern Juniper Ridge

Map unit	sample #	type	latitude	longitude
Toa_2	JR-91-46*	HS,TS	43.532	119.660
Toa_3	JR-91-42*	HS,TS	43.525	119.607
Tad_2	JR-91-43	HS,TS	43.529	119.621
	JR-91-44*	HS,TS	43.532	119.631
	JR-92-49	HS,TS	43.502	119.574
	JR-92-50*	HS,TS	43.506	119.566
Tob_2	JR-92-47*	HS,TS	43.512	119.588

(*) geochemical sample; (#) dated sample; (HS) hand sample; (TS) thin section

Eastern Juniper Ridge (continued)

Map unit	sample #	type	latitude	longitude
Tr_4	JR-92-48*	HS,TS	43.510	119.577
	JR-92-51*	HS,TS	43.498	119.553
	JR-92-52	HS,TS	43.480	119.553
	JR-92-54*	HS,TS	43.483	119.548
Tr_5	JR-91-45	HS	43.531	119.620
	JR-92-56*#	HS	43.477	199.533
	JR-92-57	HS	43.483	119.536

Southern Juniper Ridge

Map unit	sample #	type	latitude	longitude
Tad_3	JR-92-63*	HS,TS	43.439	119.683
	JR-92-64	HS	43.437	119.683
Tr_6	JR-92-65*	HS	43.438	119.685

(*) geochemical sample; (#) dated sample; (HS) hand sample; (TS) thin section

APPENDIX 3: Complete Microprobe Data for Juniper Ridge Minerals.

Sample	mineral	Na2O	MgO	Al2O3	SiO2	K2O	CaO	FeO	SrO	BaO	Ab	Or	An
JR-91-13	FELDSPAR	7.914	0.01	23.56	62.332	0.801	4.893	0.227	0	0.211	71.011	4.727	24.261
JR-91-13	FELDSPAR	7.56	0	24.043	61.876	0.712	5.508	0.158	0	0.093	68.281	4.23	27.489
JR-91-13	FELDSPAR	7.861	0	23.774	62.291	0.765	5.009	0.24	0	0.155	70.611	4.523	24.866
JR-91-13	FELDSPAR	7.837	0.018	23.643	62.56	0.785	4.87	0.208	0	0.178	70.958	4.676	24.366
JR-91-13	FELDSPAR	7.743	0.01	23.853	62.082	0.694	5.358	0.2	0	0.189	69.377	4.092	26.531
JR-91-13	FELDSPAR	7.914	0.013	23.593	61.604	0.713	5.097	0.222	0	0.185	70.665	4.186	25.149
JR-91-13	FELDSPAR	7.807	0.007	23.7	62.011	0.775	5.062	0.229	0	0.137	70.243	4.589	25.168
JR-91-13	FELDSPAR	7.351	0.011	24.319	61.813	0.692	5.548	0.229	0	0.128	67.614	4.187	28.199
JR-91-13	FELDSPAR	7.47	0.002	23.851	61.099	0.704	5.462	0.206	0	0.13	68.21	4.229	27.561
JR-91-13	FELDSPAR	7.589	0	23.838	62.112	0.722	5.228	0.17	0	0.206	69.287	4.337	26.376
JR-91-34	FELDSPAR	6.702	0	19.3	65.579	6.191	0.333	0.209	0	0.72	61.151	37.169	1.68
JR-91-34	FELDSPAR	6.114	0	19.636	65.103	6.628	0.253	0.193	0	1.111	57.601	41.082	1.317
JR-91-34	FELDSPAR	6.223	0.006	19.949	64.948	6.154	0.389	0.166	0	1.536	59.34	38.608	2.052
JR-91-34	FELDSPAR	6.778	0	19.431	65.791	6.003	0.289	0.211	0	0.652	62.256	36.279	1.465
JR-91-34	FELDSPAR	6.887	0	20.272	64.847	5.073	0.695	0.186	0	1.229	64.92	31.46	3.62
JR-91-34	FELDSPAR	5.943	0	19.288	65.455	7.238	0.198	0.12	0	0.859	54.953	44.037	1.011
JR-91-18	FELDSPAR	6.766	0	19.535	66.351	6.219	0.36	0.145	0	0.244	61.192	37.007	1.8
JR-91-18	FELDSPAR	6.115	0	19.468	66.163	7.091	0.232	0.118	0	0.383	56.055	42.768	1.177
JR-91-18	FELDSPAR	6.322	0	19.577	66.026	6.935	0.312	0.161	0	0.504	57.175	41.266	1.559
JR-91-18	FELDSPAR	5.942	0	19.482	66.603	7.408	0.189	0.163	0	0.211	54.41	44.634	0.956
JR-91-18	FELDSPAR	5.974	0.011	19.442	66.413	7.297	0.237	0.113	0	0.544	54.778	44.021	1.201
JR-91-18	FELDSPAR	5.62	0	19.284	66.179	7.981	0.169	0.138	0	0.454	51.257	47.894	0.85
JR-91-18	FELDSPAR	5.871	0.022	19.55	66.15	7.418	0.259	0.123	0	0.627	53.889	44.797	1.315
JR-92-48	FELDSPAR	6.682	0.019	25.886	58.911	0.633	7.496	0.265	0	0.105	59.446	3.704	36.85
JR-92-48	FELDSPAR	4.348	0.047	29.43	52.906	0.153	12.247	0.432	0	0.052	38.766	0.896	60.338
JR-92-48	FELDSPAR	6.946	0.021	25.175	59.876	0.712	6.781	0.32	0	0.105	62.229	4.199	33.571
JR-92-48	FELDSPAR	6.7	0	25.558	59.138	0.658	7.409	0.204	0	0.122	59.675	3.856	36.469
JR-92-48	FELDSPAR	7.146	0.004	24.572	60.87	0.857	5.898	0.266	0	0.154	65.15	5.138	29.713
JR-92-48	FELDSPAR	6.223	0.019	26.545	57.865	0.551	8.322	0.272	0	0.067	55.641	3.239	41.12
JR-92-48	FELDSPAR	7.294	0.01	24.296	61.319	0.946	5.643	0.241	0	0.171	66.101	5.641	28.258
JR-92-48	FELDSPAR	3.791	0.049	30.681	51.247	0.183	13.406	0.636	0	0	33.487	1.065	65.448
JR-92-48	FELDSPAR	4.252	0.015	29.877	52.885	0.239	12.32	0.512	0	0.021	37.906	1.4	60.694
JR-92-48	FELDSPAR	4.474	0.061	29.339	53.347	0.279	11.982	0.45	0	0.089	39.67	1.625	58.704
JR-92-48	FELDSPAR	3.946	0.055	30.082	52.321	0.234	12.732	0.486	0	0.058	35.438	1.383	63.179
JR-91-42	FELDSPAR+	3.224	0.076	31.487	49.886	0.112	14.52	0.276	0	0.03	28.48	0.65	70.87
JR-91-42	FELDSPAR+	3.037	0.13	31.057	49.618	0.117	14.757	0.472	0	0.031	26.953	0.684	72.363
JR-91-42	FELDSPAR+	5.868	0.066	26.809	56.571	0.372	9.208	0.466	0	0.065	52.389	2.185	45.427
JR-91-42	FELDSPAR+	2.998	0.139	31.384	50.144	0.144	14.765	0.474	0	0.002	26.646	0.842	72.512
JR-91-42	FELDSPAR+	2.508	0.102	32.258	48.21	0.089	15.773	0.609	0	0.041	22.232	0.519	77.249

APPENDIX 3: Complete Microprobe Data for Juniper Ridge Minerals (continued).

Sample	mineral	Na2O	MgO	Al2O3	SiO2	K2O	CaO	FeO	SrO	BaO	Ab	Or	An
JR-91-42	FELDSPAR-	5.068	0.081	28.092	54.713	0.3	10.921	0.551	0	0	44.847	1.746	53.407
JR-91-42	FELDSPAR-	4.576	0.128	29.074	53.327	0.279	12.014	0.528	0	0.036	40.144	1.613	58.243
JR-91-42	FELDSPAR-	4.382	0.096	28.848	52.934	0.27	11.96	0.616	0	0.016	39.237	1.588	59.175
JR-91-42	FELDSPAR-	3.697	0.165	30.389	51.706	0.166	13.34	0.542	0	0.016	33.074	0.977	65.949
JR-91-11	FELDSPAR+	3.221	0.158	31.81	50.385	0.06	14.56	0.476	0	0	28.488	0.347	71.165
JR-91-11	FELDSPAR+	3.012	0.151	31.756	50.233	0.06	14.659	0.374	0	0	27.009	0.352	72.638
JR-91-11	FELDSPAR+	2.73	0.14	31.926	49.485	0.05	15.206	0.445	0	0.001	24.448	0.297	75.256
JR-91-11	FELDSPAR+	3.235	0.126	31.101	50.293	0.048	14.117	0.449	0	0.014	29.231	0.284	70.486
JR-91-11	FELDSPAR+	3.11	0.113	31.289	50.007	0.054	14.357	0.447	0	0	28.071	0.319	71.61
JR-91-11	FELDSPAR-	3.637	0.228	30.453	51.41	0.054	13.512	0.684	0	0	32.651	0.318	67.032
JR-91-11	FELDSPAR-	3.466	0.159	30.893	51.352	0.076	13.856	0.638	0	0.005	31.02	0.449	68.531
JR-91-11	FELDSPAR-	2.914	0.143	31.673	50.276	0.104	14.775	0.538	0	0.04	26.144	0.614	73.242
JR-91-11	FELDSPAR-	3.15	0.139	31.057	50.724	0.069	14.338	0.668	0	0.031	28.33	0.408	71.262
JR-91-11	FELDSPAR-	3.263	0.169	30.956	50.687	0.061	14.096	0.568	0	0.046	29.412	0.364	70.223
JR-91-21	FELDSPAR+	5.502	0.058	27.331	56.228	0.432	9.372	0.332	0	0.044	50.177	2.593	47.23
JR-91-21	FELDSPAR+	5.969	0.028	26.398	57.376	0.464	8.563	0.335	0	0.071	54.234	2.773	42.993
JR-91-21	FELDSPAR+	6.183	0.035	26.297	58.125	0.486	8.358	0.342	0	0.15	55.599	2.873	41.528
JR-91-21	FELDSPAR-	5.912	0.057	26.774	57.701	0.562	8.494	0.365	0	0.093	53.865	3.37	42.766
JR-91-21	FELDSPAR-	6.182	0.029	26.449	57.864	0.616	8.363	0.419	0	0.112	55.153	3.616	41.232
JR-91-21	FELDSPAR-	5.971	0.046	26.678	57.593	0.499	8.665	0.316	0	0.029	53.854	2.961	43.185
JR-91-21	FELDSPAR-	5.366	0.049	27.682	56.201	0.381	9.96	0.405	0	0.047	48.251	2.254	49.494
JR-92-59	FELDSPAR+	3.152	0.211	31.281	49.961	0.07	14.435	0.513	0	0	28.204	0.413	71.383
JR-92-59	FELDSPAR+	3.32	0.169	31.271	50.639	0.081	14.204	0.346	0	0.043	29.582	0.476	69.942
JR-92-59	FELDSPAR+	3.473	0.171	30.336	50.284	0.077	13.547	0.476	0	0	31.546	0.459	67.995
JR-92-59	FELDSPAR+	3.165	0.179	31.235	50.351	0.074	14.66	0.501	0	0.006	27.975	0.43	71.594
JR-92-59	FELDSPAR+	2.871	0.148	31.674	49.412	0.065	14.79	0.43	0	0.03	25.896	0.384	73.72
JR-92-59	FELDSPAR+	3.189	0.153	30.74	50.729	0.094	14.217	0.414	0	0.016	28.708	0.556	70.735
JR-92-59	FELDSPAR+	3.136	0.167	31.023	50.055	0.106	14.096	0.443	0	0	28.52	0.635	70.846
JR-92-59	FELDSPAR+	3.246	0.145	31.163	50.843	0.063	14.129	0.438	0	0.013	29.255	0.375	70.37
JR-92-59	FELDSPAR-	5.793	0.08	26.94	56.386	0.349	9.218	0.729	0	0.039	52.111	2.067	45.822
JR-92-59	FELDSPAR-	3.404	0.175	30.388	51.033	0.091	13.723	0.579	0	0	30.814	0.541	68.646
JR-92-59	FELDSPAR-	3.094	0.134	31.053	50.33	0.089	14.275	0.511	0	0.03	28.022	0.53	71.447
JR-92-59	FELDSPAR-	3.463	0.212	30.449	50.75	0.102	13.653	0.513	0	0.009	31.27	0.608	68.122
JR-92-53	FELDSPAR-	3.013	0.126	31.333	50.025	0.097	14.55	0.423	0	0.02	27.104	0.575	72.32
JR-92-53	FELDSPAR-	3.586	0.121	30.546	51.512	0.115	13.445	0.507	0	0.034	32.332	0.682	66.986
JR-92-53	FELDSPAR-	5.166	0.084	27.893	55.21	0.224	10.46	0.646	0	0.009	46.564	1.331	52.105
JR-92-53	FELDSPAR-	3.295	0.102	31.238	50.917	0.091	14.025	0.534	0	0.02	29.672	0.541	69.787
JR-92-53	FELDSPAR-	3.135	0.129	31.3	50.608	0.11	14.371	0.382	0	0	28.116	0.652	71.232

APPENDIX 3: Complete Microprobe Data for Juniper Ridge Minerals (continued).

Sample	mineral	Na2O	MgO	Al2O3	SiO2	K2O	CaO	TiO2	Cr2O3	MnO	FeO	Fe2O3	Wo	En	Fs
JR-91-18	PYROXENE	0.473	0.939	0.281	48.673	0	19.225	0.176	0	1.104	28.746	1.535	43.851	2.979	53.17
JR-91-18	PYROXENE	0.53	0.828	0.283	48.077	0.001	18.933	0.177	0.016	1.07	28.372	1.728	43.953	2.673	53.375
JR-91-18	PYROXENE	0.348	1.856	0.398	48.721	0.022	19.191	0.11	0.003	1.18	27.589	1.102	43.38	5.835	50.785
JR-91-18	PYROXENE	0.444	0.863	0.267	48.227	0.01	18.981	0.208	0	1.085	28.814	1.039	43.604	2.758	53.638
JR-91-18	PYROXENE	0.421	0.881	0.326	47.493	0.001	19.154	0.231	0.008	1.04	27.881	1.158	44.582	2.852	52.565
JR-91-18	PYROXENE	0.378	1.012	0.33	48.579	0	19.009	0.168	0	1.174	29.14	0.961	43.115	3.192	53.693
JR-91-18	PYROXENE	0.025	7.053	0.159	47.748	0.007	1.215	0.087	0	2.575	40.301	0.774	2.729	22.04	75.231
JR-91-34	PYROXENE	0.02	11.24	0.336	49.76	0	1.577	0.153	0.003	1.72	35.226	0	3.424	33.941	62.636
JR-91-34	PYROXENE	0.013	11.872	0.303	50.158	0.011	1.432	0.088	0	1.695	34.661	0	3.09	35.639	61.272
JR-91-34	PYROXENE	0.307	9.508	0.812	51.53	0	19.471	0.211	0	0.858	17.624	0.36	41.311	28.063	30.626
JR-91-34	PYROXENE	0.022	11.795	0.318	49.005	0.01	1.423	0.15	0	1.682	34.05	0.507	3.11	35.876	61.014
JR-91-34	PYROXENE	0.036	11.605	0.292	49.188	0.016	1.468	0.105	0.003	1.666	34.444	1.058	3.204	35.238	61.557
JR-91-34	PYROXENE	0.013	11.555	0.284	49.288	0.004	1.471	0.132	0.019	1.746	34.733	0.522	3.195	34.918	61.887
JR-91-34	PYROXENE	0.029	11.875	0.302	49.642	0.005	1.455	0.162	0	1.631	34.676	0.42	3.141	35.657	61.202
JR-91-34	PYROXENE	0.015	12.515	0.315	49.806	0	1.419	0.13	0	1.661	33.801	0.02	3.05	37.421	59.53
JR-91-34	PYROXENE	0.021	12.124	0.325	50.028	0.004	1.479	0.101	0	1.561	34.716	0.153	3.17	36.133	60.697
JR-91-34	PYROXENE	0.321	9.043	0.628	51.101	0.001	18.787	0.138	0.01	0.982	18.557	0.562	40.291	26.981	32.728
JR-91-34	PYROXENE	0.003	11.422	0.359	49.446	0.01	1.541	0.116	0.016	1.67	35.161	0.158	3.336	34.396	62.268
JR-91-34	PYROXENE	0.019	11.826	0.32	49.889	0.001	1.444	0.125	0	1.666	35.063	0.113	3.099	35.319	61.582
JR-91-34	PYROXENE	0.014	11.838	0.278	50.077	0.004	1.45	0.122	0	1.666	34.984	0	3.115	35.385	61.5
JR-91-13	PYROXENE	0.443	1.049	0.518	48.062	0.006	19.375	0.215	0	1.161	27.722	1.239	44.653	3.364	51.983
JR-91-13	PYROXENE	0.426	0.702	0.429	48.122	0.008	17.713	0.222	0	1.303	30.474	0.69	40.713	2.246	57.041
JR-91-13	PYROXENE	0.458	0.602	0.424	47.69	0.004	18.357	0.227	0.004	1.235	29.252	1.277	42.688	1.947	55.366
JR-91-13	PYROXENE	0.376	1.379	0.313	48.243	0	19.533	0.107	0	1.138	27.404	0.916	44.657	4.386	50.957
JR-92-48	PYROXENE	0.031	20.059	0.426	51.845	0.002	1.271	0.186	0	1.035	23.587	1.27	2.627	57.649	39.725
JR-92-48	PYROXENE	0.024	18.923	0.484	51.153	0.003	1.248	0.19	0	1.06	24.82	1.307	2.612	55.092	42.296
JR-92-48	PYROXENE	0.035	19.287	0.368	52.548	0.003	1.289	0.175	0.009	1.012	25.767	0.04	2.628	54.721	42.651
JR-92-48	PYROXENE	0.025	18.589	0.715	51.828	0.003	1.445	0.191	0.007	1.079	25.943	0.22	2.985	53.422	43.593
JR-92-48	PYROXENE	0.012	18.729	0.249	52.548	0.007	1.154	0.117	0.012	1.151	26.526	0	2.364	53.365	44.27
JR-92-48	PYROXENE	0	18.344	0.266	51.666	0	1.19	0.157	0	1.149	26.536	0.439	2.463	52.803	44.734
JR-92-48	PYROXENE	0.011	20.325	0.402	52.926	0.007	1.178	0.128	0.037	1.034	24.288	0	2.393	57.437	40.17
JR-92-48	PYROXENE	0.025	20.932	0.394	53.217	0.01	1.146	0.136	0.008	1.081	23.012	0	2.335	59.327	38.337
JR-92-48	PYROXENE	0.004	26.543	0.596	54.607	0.012	1.126	0.068	0.056	0.718	15.827	0.861	2.209	72.441	25.35
JR-92-48	PYROXENE	0.015	25.732	1.694	53.393	0	0.995	0.12	0.136	0.651	16.084	1.288	1.996	71.793	26.211
JR-91-42	PYROXENE	0.196	17.331	1.918	52.347	0.001	18.266	0.53	0.192	0.241	7.625	1.166	37.648	49.693	12.659
JR-91-42	PYROXENE	0.251	16.783	1.712	52.052	0	19.286	0.489	0.171	0.297	6.594	1.61	40.166	48.624	11.209
JR-91-42	PYROXENE	0.303	15.488	2.074	51.844	0.004	20.101	0.776	0	0.367	7.543	1.512	42.03	45.053	12.918
JR-91-42	PYROXENE	0.383	14.382	3.284	50.395	0	19.213	1.055	0.02	0.43	8.749	2.274	41.417	43.13	15.453
JR-91-42	PYROXENE	0.261	15.379	2.122	51.096	0	19.79	0.769	0	0.385	7.425	1.955	41.852	45.247	12.901

APPENDIX 3: Complete Microprobe Data for Juniper Ridge Minerals (continued).

Sample	mineral	Na2O	MgO	Al2O3	SiO2	K2O	CaO	TiO2	Cr2O3	MnO	FeO	Fe2O3	Wo	En	Fs
JR-92-59	PYROXENE	0.362	12.921	3.309	49.91	0	20.237	1.806	0.052	0.294	10.37	1.185	43.484	38.625	17.891
JR-92-59	PYROXENE	0.32	13.483	2.312	50.873	0.017	20.5	1.205	0.05	0.246	9.838	0.534	43.495	39.799	16.706
JR-92-59	PYROXENE	0.44	10.988	2.94	48.712	0.022	18.766	2.382	0	0.405	14.247	0.931	41.251	33.602	25.147
JR-92-59	PYROXENE	0.374	12.747	3.366	49.413	0.008	20.453	2.014	0.036	0.233	9.982	1.544	44.308	38.416	17.277
JR-92-53	PYROXENE	0.322	14.448	3.147	50.76	0.011	20.464	1.721	0.194	0.249	8.499	1.355	43.178	42.409	14.413
JR-92-53	PYROXENE	0.304	14.567	3.562	50.205	0	20.879	2.027	0.163	0.165	7.564	1.022	44.255	42.955	12.791
JR-92-53	PYROXENE	0.381	13.683	2.31	50.787	0.006	19.685	1.86	0.043	0.292	10.713	0.871	41.605	40.233	18.162
JR-92-53	PYROXENE	0.408	13.984	3.36	49.584	0.016	18.96	2.484	0.172	0.315	10.051	1.596	40.766	41.83	17.404
JR-92-53	PYROXENE	0.395	13.713	2.031	50.79	0.001	18.812	1.601	0.001	0.346	11.445	0.94	39.945	40.507	19.548
Sample	mineral	MgO	Al2O3	SiO2	CaO	MnO	NiO	FeO	Mo	Fo	Fa	Li	Th		
JR-91-13	OLIVINE	0.675	0	28.948	0.169	2.976	0	65.942	0.31	1.719	94.281	0	4.31		
JR-91-13	OLIVINE	0.684	0	29.278	0.173	2.9	0	66.503	0.315	1.731	94.414	0	4.17		
JR-91-13	OLIVINE	0.674	0	29.078	0.175	2.741	0	66.171	0.321	1.718	94.632	0	3.97		
JR-91-42	OLIVINE	40.22	0.039	37.628	0.172	0.358	0.041	21.349	0.237	76.935	22.913	0.042	0.389		
JR-91-42	OLIVINE	42.662	0.051	38.162	0.165	0.308	0.214	18.074	0.224	80.709	19.185	0.219	0.331		
JR-91-11	OLIVINE	40.455	0.09	37.756	0.289	0.293	0.14	19.978	0.402	78.366	21.713	0.146	0.323		
JR-91-11	OLIVINE	40.526	0.066	37.941	0.266	0.292	0.095	20.85	0.366	77.637	22.411	0.098	0.318		
JR-91-11	OLIVINE	39.119	0.071	37.912	0.248	0.303	0.095	21.984	0.346	76.036	23.975	0.1	0.334		
JR-91-11	OLIVINE	41.605	0.109	38.668	0.268	0.292	0.121	18.84	0.369	79.781	20.27	0.125	0.319		
JR-91-21	OLIVINE	13.931	0.024	31.925	0.256	1.968	0	51.833	0.418	31.698	66.176	0	2.544		
JR-91-21	OLIVINE	14.84	0.02	32.12	0.273	1.873	0	50.409	0.446	33.734	64.292	0	2.42		
JR-91-21	OLIVINE	15.763	0.056	32.198	0.16	1.616	0	49.797	0.258	35.417	62.778	0	2.063		
JR-91-21	OLIVINE	16.503	0.47	32.358	0.231	1.635	0	48.363	0.373	37.167	61.114	0	2.093		
JR-92-59	OLIVINE	25.817	0.014	34.68	0.404	0.648	0.044	37.626	0.618	54.923	44.911	0.05	0.783		
JR-92-59	OLIVINE	27.316	0.047	35.072	0.383	0.544	0.099	35.854	0.58	57.548	42.381	0.113	0.651		
JR-92-59	OLIVINE	31.239	0.053	35.995	0.376	0.532	0.041	30.692	0.558	64.422	35.512	0.045	0.624		
JR-92-59	OLIVINE	43.573	0.056	38.69	0.253	0.25	0.175	15.693	0.348	83.253	16.823	0.18	0.271		
JR-92-53	OLIVINE	31.529	0.042	36.121	0.32	0.465	0.069	30.759	0.472	64.581	35.35	0.076	0.541		
JR-92-53	OLIVINE	43.569	0.072	38.588	0.191	0.235	0.184	16.788	0.259	82.23	17.777	0.187	0.252		
JR-92-53	OLIVINE	44.217	0.056	38.92	0.235	0.213	0.253	16.141	0.317	83.075	17.015	0.256	0.227		
JR-92-53	OLIVINE	39.971	0.082	37.768	0.275	0.28	0.138	20.811	0.383	77.45	22.625	0.145	0.308		
JR-92-53	OLIVINE	40.36	0.078	37.662	0.275	0.281	0.201	20.335	0.382	78.018	22.055	0.209	0.309		
JR-91-18	ILMENITE	0.068	0	0	49.051	0.254	0.042	1.253	42.737	0	0.328	5.285			
JR-91-18	ILMENITE	0.076	0	0.029	48.351	0.271	0	1.247	42.081	0.063	0.492	5.964			
JR-91-18	ILMENITE	0.068	0	0.031	47.858	0.261	0.01	1.361	41.54	0.091	0.252	7.2			
JR-91-18	ILMENITE	0.092	0	0.059	48.305	0.213	0.04	1.236	42.041	0.06	0.343	5.792			
JR-91-18	ILMENITE	0.088	0	0.044	48.518	0.284	0.011	1.33	42.13	0	0.353	5.776			
JR-91-18	ILMENITE	0.071	0	0.04	48.972	0.213	0.016	1.325	42.576	0.014	0.346	5.133			
JR-91-42	ILMENITE	1.862	0	0.077	48.728	0.436	0	0.57	39.922	0.091	0.094	6.424			

APPENDIX 3: Complete Microprobe Data for Juniper Ridge Minerals (continued).

sample	mineral	MgO	Al2O3	SiO2	TiO2	V2O5	Cr2O3	MnO	FeO	ZrO2	Nb2O5	Fe2O3
JR-91-42	ILMENITE	1.6	0	0.079	47.728	0.491	0.04	0.534	39.545	0.215	0.009	8.533
JR-91-42	ILMENITE	1.457	0	0.092	48.07	0.563	0	0.48	40.143	0.425	0.17	7.049
JR-92-48	ILMENITE	2.122	0	0.01	45.696	0.465	0.021	0.849	36.459	0.004	0.049	13.65
JR-92-48	ILMENITE	1.814	0	0.026	45.827	0.368	0	0.804	37.161	0.109	0.098	13.231
JR-92-48	ILMENITE	1.994	0	0.014	45.889	0.353	0.005	0.807	36.896	0.06	0.122	13.471
sample	mineral	MgO	Al2O3	SiO2	TiO2	V2O5	Cr2O3	MnO	FeO	ZrO2	Fe2O3	
JR-91-13	MAGNETITE	0.033	0.386	0.107	15.463	0.081	0	0.77	44.441	0	38.227	
JR-91-13	MAGNETITE	0.031	0.387	0.093	15.513	0.062	0	0.813	44.48	0.095	38.204	
JR-91-13	MAGNETITE	0.055	0.402	0.1	15.464	0.083	0.004	0.727	44.544	0.036	38.411	
JR-91-18	MAGNETITE	0.045	0.389	0.067	17.336	0.214	0	0.882	45.959	0	34.411	
JR-91-18	MAGNETITE	0.02	0.416	0.098	17.388	0.062	0.031	0.783	46.284	0	34.524	
JR-91-18	MAGNETITE	0.04	0.428	0.071	17.186	0.097	0.011	0.942	45.944	0	35.015	
JR-91-18	MAGNETITE	0.052	0.448	0.129	17.478	0.117	0.047	0.803	46.25	0	34.196	
JR-91-18	MAGNETITE	0.03	0.447	0.109	16.974	0.087	0.01	0.786	45.925	0	35.401	
JR-91-18	MAGNETITE	0.047	0.418	0.082	17.123	0.138	0	0.815	45.915	0	34.976	
JR-91-34	MAGNETITE	0.519	1.108	0.07	16.363	0.235	0	0.789	44.726	0.047	36.105	
JR-91-34	MAGNETITE	0.522	1.12	0.087	16.276	0.234	0	0.769	44.646	0	36.217	
JR-91-34	MAGNETITE	0.502	1.113	0.11	16.587	0.265	0.034	0.86	44.896	0.051	35.633	
JR-91-34	MAGNETITE	0.504	1.18	0.149	15.86	0.253	0	0.76	44.142	0	36.577	
JR-91-34	MAGNETITE	0.501	1.135	0.065	15.313	0.182	0.026	0.728	43.799	0.073	37.958	
JR-91-34	MAGNETITE	0.501	1.104	0.157	16.232	0.182	0	0.757	44.615	0.066	36.239	
JR-91-21	MAGNETITE	0.283	0.67	0.057	20.837	0.104	0	0.857	49.112	0	27.868	
JR-91-21	MAGNETITE	0.445	0.77	0.067	21.358	0.115	0	1.043	49.101	0.025	26.663	
JR-91-21	MAGNETITE	0.346	0.81	0.116	19.339	0.11	0	0.947	47.591	0.098	30.709	
JR-91-42	MAGNETITE	2.201	2.708	0.058	17.944	0.893	0.232	0.443	44.065	0.055	31.446	
JR-91-42	MAGNETITE	0.94	0.967	0.071	17.404	1.01	5.246	0.411	45.134	0.025	28.371	
JR-91-42	MAGNETITE	1.881	2.061	0.052	17.145	1.029	0.173	0.428	43.745	0.015	33.704	
JR-92-48	MAGNETITE	0.994	1.607	0.075	7.167	0.692	0.052	0.564	35.516	0.066	52.93	
JR-92-48	MAGNETITE	0.998	1.473	0.051	8.761	0.654	0.056	0.564	37.021	0	50.125	
JR-92-48	MAGNETITE	0.96	1.497	0.07	9.091	0.633	0.054	0.535	37.617	0	49.877	

Appendix 4: Parent compositions for major and trace element model

Element	Stage 1 F = 0 to 10% (JR-92-53)	Stage 2 F = 10 to 40%	Stage 3 F = 40 to 70%	Stage 4 F = 70 to 85%
(wt. %)				
SiO2	47.6	49.0	52.7	60.9
TiO2	1.56	1.66	1.53	0.94
Al2O3	16.37	16.92	16.65	16.00
FeO	11.81	11.40	9.96	6.87
MnO	0.19	0.19	0.19	0.24
MgO	9.13	6.67	5.35	3.19
CaO	9.8	10.2	8.4	5.2
Na2O	2.88	3.13	3.69	4.28
K2O	0.32	0.45	0.91	2.03
P2O5	0.32	0.36	0.54	0.31
(ppm)				
Sr	277.30	301.51	359.30	269.66
Rb	2.70	6.34	18.63	47.16
Ba	270.30	332.64	553.63	1034.30
Sc	32.00	34.80	25.31	17.34
Cr	279.00	281.01	82.74	15.99
Co	52.20	49.79	31.26	14.74
Ni	174.90	109.45	66.87	11.85
V	243.40	257.80	210.12	108.81
Zn	97.00	101.21	90.67	81.92
Nb	5.30	6.16	9.30	14.72
Zr	107.30	124.50	177.25	286.52
Y	28.10	31.90	33.16	36.34
La	7.99	9.53	15.33	24.94
Ce	18.82	22.22	34.28	49.96
Nd	14.49	16.63	22.88	27.91
Sm	4.03	4.58	5.43	6.07
Eu	1.56	1.66	1.86	1.74
Tb	0.81	0.92	1.42	2.91
Yb	2.60	2.96	3.31	3.91
Lu	0.38	0.43	0.49	0.59
Hf	2.76	3.22	3.80	6.38
Ta	0.23	0.28	0.46	0.81
Th	0.35	0.70	1.90	4.10

Appendix 5: Mineral/melt partition coefficients for trace element model (mafic and intermediate rocks)

Stage 1:					Stage 2:						Stage 3:							Stage 4:						
T = 1240; F = 0 to 10 %; r = 0.22					T = 1220; F = 10 to 40 %; r = 0.15						T = 1120; F = 40 to 70 %; r = 0.10							T = 1020; F = 70 to 85 %; r = 0						
phase	plag	ol	mgt	total	plag	ol	cpx	mgt	ilm	total	plag	ol	cpx	apat	mgt	ilm	total	plag	opx	cpx	apat	mgt	ilm	total
%	37.7	59	3.3	100	53	10	28.7	7.4	0.9	100	59.1	10.5	20.4	1.6	5.4	3	100	66	17	10.5	1.3	3	2.2	100
Sr	0.74	0.001	0		0.99	0.001	0.1	0	0		2.1	0.001	0.3	1.3	0	0		4	0.02	2.3	2.1	0	0	
Rb	0.09	0.001	0		0.09	0.0005	0.01	0	0		0.1	0.0006	0.01	0	0	0		0.2	0.02	0.02	0	0	0	
Ba	0.3	0.005	0		0.35	0.005	0.04	0	0		0.4	0.006	0.05	0	0	0		1	0	0.1	0	0	0	
Sc	0.05	0.22	1.3		0.05	0.23	4.8	1.4	1.4		0.06	0.25	6	0.04	1.5	1.6		0.09	1.3	8	0.07	2.5	2.5	
Cr	0	0.12	20		0	0.14	1.8	25	20		0	0.24	11	0	25	15		0	14	130	0	30	15	
Co	0	1.1	15		0	1.1	1.6	17	1.4		0	1.2	1.8	0	25	1.6		0	2.5	2.8	0	30	2.5	
Ni	0	7	4		0	10	2	4	3		0	14	6	0.5	6	5		0	10	15	0.8	6	5	
V	0.04	0.04	10		0.04	0.04	0.35	15	6		0.05	0.04	0.4	0	25	10		0.07	0.41	0.6	0	35	15	
Zn	0	0.63	5		0	0.63	0.37	13	0		0	0.72	0.37	0	17	0		0	0	0.7	0	30	0	
Nb	0.01	0.01	1.4		0.01	0.01	0.06	0.38	15		0.01	0.01	0.01	0	0.4	12		0.02	0.002	0.006	0	1	10	
Zr	0.01	0.01	1.3		0.01	0.01	0.8	0.35	5		0.01	0.01	0.15	0.3	0.4	10		0.02	0.03	0.06	0.5	0.9	15	
Y	0.03	0.003	0.004		0.03	0.003	3	0.004	0.004		0.03	0.004	2.5	20	0.004	0.005		0.05	0.1	1.5	10	0.004	0.005	
La	0.1	0.0001	0.003		0.11	0.0001	0.25	0.003	0.007		0.1	0.0001	1	7.5	0.003	0.007		0.15	0.01	1.3	8	0.003	0.007	
Ce	0.07	0.0001	0.003		0.07	0.0001	0.5	0.003	0.008		0.06	0.0001	1.5	11	0.003	0.008		0.08	0.01	1.5	11	0.003	0.008	
Nd	0.07	0.0002	0.002		0.07	0.0002	1	0.002	0.009		0.06	0.0002	2	17	0.002	0.008		0.08	0.03	2	17	0.002	0.008	
Sm	0.04	0.001	0.003		0.04	0.001	2	0.003	0.01		0.04	0.002	2	24	0.003	0.01		0.04	0.03	1.2	24	0.003	0.01	
Eu	1.1	0.002	0.001		1.2	0.002	0.1	0.001	0.001		1.3	0.002	0.5	10	0.001	0.001		3	0.02	0.6	10	0.001	0.001	
Yb	0.03	0.04	0.02		0.03	0.04	2.5	0.02	0.02		0.02	0.05	3	8	0.02	0.02		0.03	0.1	1.5	8	0.02	0.02	
Lu	0.02	0.07	0.02		0.02	0.07	2.5	0.02	0.03		0.02	0.1	3	7	0.02	0.03		0.03	0.1	1.5	7	0.02	0.03	
Hf	0	0.0001	1.6		0.0001	0.0001	2.3	0.4	6.4		0.0001	0.0001	0.5	0.4	0.5	7		0.0002	0.06	0.2	0.6	1.1	10	
Ta	0.02	0.0001	1.6		0.02	0.0001	0.23	0.5	5		0.03	0.0001	0.05	0	0.5	8		0.04	0.01	0.03	0	1.2	10	
Th	0.005	0.001	0.1		0.005	0.001	0.04	0.5	1		0.006	0.001	0.05	6	1.5	2.5		0.01	0.01	0.1	8	1.5	3	

T in degrees C; F = percent crystallization; r = rate of assimilation with respect to rate of crystallization (DePaolo, 1981).

Appendix 5 (cont.): Mineral/melt partition coefficients for trace element model (Squaw Butte and rhyolitic rocks)

Squaw Butte zone refining model						Western Juniper Ridge rhyolites									Eastern Juniper Ridge rhyolites						
phase	plag	ol	cpx	mgt	total	phase	san	plag	cpx	qtz	mgt	allan	zirc	total	san	plag	cpx	qtz	mgt	zirc	total
%	25	60	10	5	100	%	38	13	10	37.615	1.3	0.025	0.06	100	40	27.5	2	28.977	1.5	0.023	100
Sr	4	0.001	0.3	0		Sr	5.1	6.8	0.67	0					5.1	6.8	0.67	0			
Rb	0.05	0.0006	0.01	0		Rb	2.4	0.09		0					2.4	0.09		0			
Ba	0.4	0.006	0.05	0		Ba	5.4	0.63	0	0					2.1	0.63	0	0			
						Sc	0.04	0.06	30	0	8.9	0.46			0.04	0.06	30	0	5		
Sc	0.06	0.25	6	1.5																	
Cr	0	0.24	11	25		Nb		0.06	1.5	0	10					0.06	0.8	0	10		
Co	0	1.2	1.8	25		Zr	0.02	0.04	0.6	0	0.8		1190		0.02	0.04	0.6	0	0.8	1190	
Ni	0	14	6	6		Y	0	0.04	2.7	0	2				0	0.04	2.7	0	2		
V	0.05	0.04	0.4	25																	
Zn	0	0.72	0.37	17		La	0.1	0.32	0.76	0	26	1331	3.3		0.1	0.32	0.76	0	26	3.3	
						Ce	0.06	0.21	1.2	0	22.9	1279	2.4		0.06	0.21	1.2	0	22.9	2.4	
Nb	0.01	0.01	0.01	0.4		Nd	0.04	0.14	2.3	0	18.6	874			0.04	0.14	2.3	0	18.6		
Zr	0.01	0.01	0.15	0.4		Sm	0.04	0.11	3.6	0	12.49	438	3.7		0.04	0.11	3.6	0	12.49	3.7	
Y	0.03	0.004	1.8	0.004		Eu	4.6	3.8	3.2	0	2.8	107	3.4		4.6	3.8	3.2	0	2.8	3.4	
						Tb	0.06	0.09	4.6	0	7.5	204	26.3		0.06	0.09	4.6	0	7.5	26.3	
La	0.1	0.0001	0.25	0.003		Yb	0.04	0.06	3.5	0		22	225		0.04	0.06	3.5	0		225	
Ce	0.06	0.0001	0.75	0.003		Lu	0.03	0.06	3.3	0		22	300		0.03	0.06	3.3	0		300	
Nd	0.06	0.0002	1	0.002																	
Sm	0.04	0.002	1.5	0.003		Hf	0.02	0.06	0.37	0	0	2	1190		0.02	0.06	0.37	0	0	1190	
Eu	1.3	0.0021	0.5	0.001		Ta	0.02	0.02	0.09	0	5	3.2	4.8		0.02	0.02	0.09	0	5	4.8	
Tb						Th	0.03	0.03	0.09	0	20	400	14.8		0.03	0.03	0.09	0	20	14.8	
Yb	0.02	0.05	1.8	0.02																	
Lu	0.02	0.1	1.8	0.02																	
Hf	0.0001	0.0001	0.5	0.5																	
Ta	0.03	0.0001	0.05	0.5																	
Th	0.006	0.001	0.05	1.5																	